2007

Investigation of a Rectenna element for infrared and millimeter wave application

Henrry La Rosa
University of South Florida

Scholar Commons Citation

La Rosa, Henrry, "Investigation of a Rectenna element for infrared and millimeter wave application" (2007). *Graduate Theses and Dissertations.*
http://scholarcommons.usf.edu/etd/2251

Investigation of the Rectenna Concept for Millimeter Wave Applications

by

Henrry La Rosa

A thesis submitted in partial fulfillment
of the requirements for the degree of
Master of Science in Electrical Engineering
Department of Electrical Engineering
College of Engineering
University of South Florida

Co-Major Professor: Elias Stefanakos, Ph.D.
Co-Major Professor: Kenneth A. Buckle, Ph.D.
Thomas M. Weller, Ph.D.
Shekhar Bhansali, Ph.D.

Date of Approval:
November 5, 2007

Keywords: Microstrip Slot Antenna, Schottky Diode, Detector, Coplanar Waveguide (CPW), Wideband, *W* band, Membrane

Dedication

To my fiancé Stephanie Pedersen, my parents Felix N. La Rosa and Concepsion A. La Rosa, and my sister Arlettys La Rosa

Acknowledgements

I would like to express my gratitude to the individuals who have contributed to this thesis work. I gratefully acknowledge my advisor Elias Stefanakos, Ph.D., P.E. and my co-advisor Kenneth A. Buckle, Ph.D., P.E. for their excellent guidance, unconditional support, and for providing me with the opportunity to work in such interesting projects such as the one mentioned in this thesis. I also would like to thank Thomas M. Weller, Ph.D. for his excellent technical support and guidance. In addition, I would like to express my gratitude to Shekhar Bhansali, Ph.D., Mr. Bernard Batson, and the Bridge to the Doctorate program for their financial support and supervision. I would also like to recognize Modelithics Inc. and the WAMI program for providing me the necessary equipment needed for the success of this project.

My gratitude also goes to all my colleagues in ENB 412 and ENB 245 who made the success of this project possible. Especially I would like to express my gratitude to Subramanian Krishnan for the development and fabrication of the MIM diode as well as the fabrication of the 94GHz slot antenna. I would also like to especially thank Suzette Presas for her unconditional friendship, support, and reviewing this thesis work. In addition, I would like to thank Alberto Rodriguez and Sergio Melais for their technical support and guidance through out the project. My gratitude also goes to Saravana P. Natarajan for assisting with the 94GHz system fabrication process. Finally, I want to thank Bojana Zevanovic for reviewing this thesis work.

Table of Contents

List of Tables iv

List of Figures v

Abstract xii

Chapter 1 - Introduction 1

- 1.1 Overview 1
- 1.2 Motivation 4
- 1.3 Thesis Organization 4
- 1.4 Contributions 5

Chapter 2 - 2.5GHz Slot Antenna Design 7

- 2.1 Introduction 7
  - 2.1.1 Background Theory 7
  - 2.1.2 Input Impedance 9
  - 2.1.3 Radiation Pattern 11
- 2.2 Motivation for Using a CPW-fed Slot Antenna 14
- 2.3 CPW-fed Narrow Slot Antenna 15
- 2.4 Antenna Efficiency and Gain Definitions 24
- 2.5 CPW-fed Wide Slot Antenna with Tuning Stubs 26
- 2.6 Antenna Simulations with Reflector in Place 30
- 2.7 Result and Comparison 34

2.7.1 2.5GHz Narrow Slot Antenna 34

2.7.2 Radiation Pattern Measurements 36

2.7.3 2.5GHz Wide Slot Antenna with U-shaped Tuning Stubs Results 41

2.8 Chapter Summary and Conclusions 46

Chapter 3 - 2.5GHz Detector Circuit Design – Integration of Rectenna Element 47

3.1 Introduction 47

3.1.1 Background Theory 48

3.2 Detector Circuit Design 51

3.3 Rectenna Element Integration 61

3.3.1 Via-less CPW-to-Microstrip Transition 61

3.4 Results and Comparison 66

3.4.1 2.5GHz Detector Circuit 66

3.4.2 Via-less CPW-to-Microstrip Transition Results 71

3.4.3 Antenna/CPW-to-Microstrip Integration Results 73

3.4.4 2.5GHz Rectenna Element Integration 75

3.5 Chapter Summary and Conclusions 78

Chapter 4 - 94GHz Antenna Design 79

4.1 Introduction 79

4.1.1 Millimeter Wave Band Characteristics 79

4.1.2 Advantages and Disadvantages 79

4.1.3 Applications 82

4.2 94GHz CPW-fed Slot Antenna Design 84

4.2.1 Surface Wave in Silicon 85

4.2.2 Substrate Thickness Characterization Using Momentum 86

4.2.3 TRL Standards and Substrate Thickness Issues 90

4.3 Results and Comparisons 92

4.4 Chapter Summary and Conclusions 99

Chapter 5 – Summary and Recommendations 101

5.1 Conclusions 101

5.2 Future Work and Recommendations 104

References 106

Appendices 109

Appendix A: 2.5GHz Rectenna Elements Measurements' Setup 110

Appendix B: Low Frequency Calibration Standards and Results 117

Appendix C: *W* band Calibration Standard Results 125

List of Tables

Table 2.1 Comparison Between the Slot and Patch Antenna Characteristics. 14

Table 2.2 Comparison Between the Center-fed and Offset-fed Simulated Antenna Parameters. 24

Table 2.3 Comparison Between the Simulated Antenna Parameters with no Reflector, Finite Reflector, and Infinite Reflector Placed at dr = ¼λ. 33

Table 3.1 Step Impedance Filter Dimensions. 53

Table 3.2 Measured Input Power and Output Voltage as a Function of Attenuation Setting. 69

Table 4.1 Radar System Performance in Millimeter Wave, Microwave, and Optical Frequencies. 82

Table 4.2 Millimeter Wave Applications in the Four Major Areas of Wireless Communication [24]. 83

Table 4.3 Slot Antenna Efficiency, Directivity, and Gain as a Function of Substrate Thickness. 88

Table A.1 Recorded Data for the Rectenna Elements Connected by a M-M Barrel. 115

Table A.2 Recorded Data for the Fully Integrated Rectenna Element. 116

List of Figures

Figure 1.1 Nahas Model for Microwave-to-DC Energy Conversion [3]. 2

Figure 2.1 (a) Center-fed Slot Antenna Short Circuited Through the Substrate. 8

Figure 2.2 Voltage and Current Distribution Around the Slot. 9

Figure 2.3 Different Feeding Methods Used to Decrease the Slot Antenna Input Impedance. 10

Figure 2.4 (a) ½λ Slot Antenna on an Infinite Ground Plane, (b) Complementary ½λ Printed Dipole Antenna. 11

Figure 2.5 (a) Radiated Fields of a Slot Antenna on an Infinite Ground Plane, (b) and Radiated Fields of the Complementary Dipole Antenna. 12

Figure 2.6 Slot Antenna Fed by a Microstrip Line with (a) Vertical Polarization, and (b) Horizontal Polarization. 13

Figure 2.7 CPW-fed Slot Antenna Feeding Mechanisms: (a) Center-fed Slot Antenna, (b) Offset-fed Slot Antenna with Bond Wire for Stability, (c) Capacitively Coupled, and (d) Inductively Coupled Slot Antenna. 16

Figure 2.8 (a) Current Density Distribution of the Center-fed Slot Antenna, and (b) Radiated Electric Field. 17

Figure 2.9 Center-fed Slot Antenna Results. 18

Figure 2.10 Effect of the Offset Point d_S on the Series Resistance of the Slot Antenna. 19

Figure 2.11 Normalized Impedance of the Slot Referenced at the Edge of the Antenna. 20

Figure 2.12 ADS Schematic Utilized to Find the Impedance of the Slot Antenna. 20

Figure 2.13 Normalized Impedance of the Slot Referenced at the Slot. 21

Figure 2.14 Phase of the Slot Antenna at ds = 0, 5, 8, 10, and 12mm. 22

Figure 2.15 Linearly Polarized Radiation Pattern Obtain in Momentum. 23

Figure 2.16 CPW-fed Wide Slot Antenna with U-shaped Tuning Stub Layout. 27

Figure 2.17 (a) Current Density Distribution of the Center-fed Wide Slot Antenna with U-shaped Tuning Stub, and (b) 3D Radiated Electric Field. 28

Figure 2.18 (a) Wide Slot Antenna Return Loss, and (b) Wide Slot Antenna Phase. 29

Figure 2.19 Simulated VSWR of the CPW-fed Wide Slot Antenna with U-shaped Tuning Stubs. 30

Figure 2.20 Microstrip-fed Slot Antenna with a Plane Reflector for Unidirectional Radiation. 30

Figure 2.21 Reflector Spacing Effect on the Wide Slot Antenna RL. 31

Figure 2.22 Simulated Radiation Pattern as a Function of Reflector Spacing. 32

Figure 2.23 3D Radiated Field. 33

Figure 2.24 Photograph of the Narrow Slot Antenna Fabricated on a FR-4 Board. 34

Figure 2.25 Narrow Slot Antenna Measured vs. Simulated Data. 35

Figure 2.26 Measure vs. Simulated RL of the Tuned Narrow Slot Antenna. 36

Figure 2.27 Measured vs. Simulated Phase of the Narrow Slot Antenna. 36

Figure 2.28 Radiation Pattern of a Vertical Slot and Coordinate System. 37

Figure 2.29 (a) Photograph of the Narrow Slot Antenna E-plane Measurement Setup. 38

Figure 2.30 (a) Photograph of the Narrow Slot Antenna H-plane Measurement Setup. 39

Figure 2.31 Measured vs. Simulated Cross-polarized E-plane. 40

Figure 2.32 Measured vs. Simulated Cross-polarized H-plane. 40

Figure 2.33 Measured vs. Simulated Return Loss of the 2.5GHz Wide Slot Antenna with U-shaped Tuning Stubs. 41

Figure 2.34 Measured vs. Simulated Wide Slot Antenna Impedance. 42

Figure 2.35 Measured vs. Simulated VSWR. 43

Figure 2.36 (a) Photograph of the Wide Slot Antenna E-plane Measurement Setup. 44

Figure 2.37 (a) Photograph of the Wide Slot Antenna H-plane Measurement Setup. 45

Figure 3.1 Typical Forward Current vs. Forward Voltage in Logarithmic Scale Representation. 49

Figure 3.2 Conventional RF Detector Circuit Schematic. 50

Figure 3.3 Step Impedance Low Pass Filter Momentum Layout. 53

Figure 3.4 Step Impedance Low Pass Filter Response. 54

Figure 3.5 ¼λ Shorted Stub IL and RL. 55

Figure 3.6 Harmonics Generated by the Rectification Process at the Input of the Detector. 55

Figure 3.7 Harmonics Generated by the Rectification Process at the Output of the Detector with ¼λ Stub in Place. 56

Figure 3.8 Detector Input Port Interface. 57

Figure 3.9 Simulated Output Voltage vs. Input Power. 59

Figure 3.10 Simulated Detector Sensitivity. 59

Figure 3.11 (a) Optimized Detector Circuit Layout. 60

Figure 3.12 Via-less CPW-to-Microstrip Transition Sections. 62

Figure 3.13 CPW-to-Microstrip Transition Simulated Data. 63

Figure 3.14 2.5GHz Wide Slot Antenna and CPW-to-Microstrip Transition Integration. 64

Figure 3.15 Radiation Pattern Comparison Between the Simulated Wide Slot Antenna with and without the Transition in Place. 66

Figure 3.16 Photograph of the Fabricated 2.5GHz Detector Circuit with SOLT and TRL Calibration Reference Plane. 67

Figure 3.17 2.5GHz Detector Circuit Simulated vs. Measured RL Using Different Calibration Techniques. 68

Figure 3.18 Simulated vs. Measured Detector Performance. 70

Figure 3.19 Visual of the 2.5GHz Via-less CPW-to-Microstrip Transition. 71

Figure 3.20 Simulated vs. Measured CPW-to-Microstrip Transition. 72

Figure 3.21 (a) Visual of the Fabricated Slot Antenna/Transition. 73

Figure 3.22 Simulated vs. Measured Radiation Pattern for the Integrated Antenna. 75

Figure 3.23 Photograph of the Fully Integrated Rectenna Element. 76

Figure 3.24 Comparison Between the Measured Rectenna Element in a Single FR-4 Board vs. the Rectenna Element Connected by M-M Barrel. 76

Figure 4.1 Millimeter Wave Atmospheric Absorption for Horizontal Propagation [25]. 80

Figure 4.2 Atmospheric Attenuation Due to Precipitation Rate [25]. 81

Figure 4.3 3D Radiation Pattern for the 94GHz Slot Antenna as a Function of Substrate Thickness. 87

Figure 4.4 94GHz Slot Antenna (a) Layout, (b) Simulated RL, and (c) Simulated Phase. 89

Figure 4.5 94GHz vs. 2.5GHz Simulated 2D Radiation Pattern. 90

Figure 4.6 94GHz Elements on a 10µm Silicon Membrane. 91

Figure 4.7 Visual of the Fabricated Devices. 93

Figure 4.8 Close up Visual of: (a) the 94GHz Slot Antenna and (b) 20µm Silicon Membrane. 93

Figure 4.9 Measured vs. Simulated Antenna RL; Obtained with the CS-5 Calibration Kit. 94

Figure 4.10 RL of the Different Slot Antennas Measured with the CS-5 Calibration Kit. 95

Figure 4.11 IL of the Different Slot Antennas Measured with the CS-5 Calibration Kit. 95

Figure 4.12 RL of the Different Slot Antennas Measured with the On-wafer Calibration Kit. 96

Figure 4.13 (a) Top View of the Fabricated Substrate and (b) View of the Back Etched Membranes. 96

Figure 4.14 Close up of the Fabricated Slot Antenna on top of ~5μm Silicon Membrane. 97

Figure 4.15 RL of the Different Slot Antennas Measured with the CS-5 Calibration Kit. 98

Figure 4.16 RL of the Different Slot Antennas Measured with the On-wafer Calibration. 98

Figure 4.17 Phase of the Different Slot Antennas Measured with the On-wafer Calibration Standards. 99

Figure A.1 Block Diagram for One-Port S-parameter Measurements. 110

Figure A.2 Block Diagram of a Full Two-Port S-parameter Measurements. 111

Figure A.3 Typical Block Diagram for Antenna Range Measurements. 112

Figure A.4 Square-law Detector Block Diagram Measurement Setup. 112

Figure A.5 Block Diagram for the Integrated Rectenna Element Power Measurements. 114

Figure B.1 IL of the SOLT Thru Standard. 117

Figure B.2 Phase Response of the SOLT Thru Standard. 118

Figure B.3 RL of the SOLT Load Standard. 118

Figure B.4 RL of the SOLT Open Standard. 119

Figure B.5 RL of the SOLT Short Standard. 119

Figure B.6 (a) Drawing of a Given TRL Standard Kit and Reference Plane. 120

Figure B.7 IL of the TRL Thru Standard. 122

Figure B.8 RL of the TRL Thru Standard. 122

Figure B.9 Phase of the TRL Thru Standard. 123

Figure B.10 Phase of the TRL Delay Standard. 123

Figure B.11 RL of the TRL Delay Standard. 124

Figure B.12 RL of the TRL Open Standard. 124

Figure C.1 Visual of the *W* band Measurement Setup. 125

Figure C.2 IL of the CS-5 Thru Standard (After Reference Plane Shift to Probe Tips). 126

Figure C.3 RL of the CS-5 Thru Standard (After Reference Plane Shift to Probe Tips). 126

Figure C.4 Phase of the TRL Thru Standard (After Reference Plane Shift to Probe Tips). 127

Figure C.5 RL of the CS-5 550μm Delay Standard (After Reference Plane Shift to Probe Tips). 127

Figure C.6 Phase of the CS-5 550μm Delay Standard (After Reference Plane Shift to Probe Tips). 128

Figure C.7 RL of the CS-5 Open Standard (After Reference Plane Shift to Probe Tips). 128

Figure C.8 Phase of the CS-5 Open Standard (After Reference Plane Shift to Probe Tips). 129

Figure C.9 Drawing of the On-wafer Calibration Standards. 130

Figure C.10 IL of the On-wafer Thru Standard. 130

Figure C.11 Phase of the On-wafer Thru Standard. 131

Figure C.12 RL of the On-wafer Thru Standard. 131

Figure C.13 RL of the On-wafer Delay Standard. 132

Figure C.14 IL of the On-wafer Delay Standard. 132

Figure C.15 Phase of the On-wafer Delay Standard. 133

Figure C.16 RL of the On-wafer Open Standard. 133

Figure C.17 Phase of the On-wafer Open Standard. 134

Investigation of the Rectenna Concept for Millimeter Wave Applications

Henrry La Rosa

ABSTRACT

This thesis presents the rectifying antenna potential for infrared and millimeter wave energy conversion. Infrared imaging is one of the emerging technologies that have attracted considerable attention in the next generation of military, medical, and commercial applications. Moreover, with the ever-increasing congestion of the electromagnetic spectrum at RF and microwave frequencies and the establishment of firm civilian and military requirements best met by millimeter wave systems, the interest in the technology has grown and is now firmly established. During this work a 2.5GHz slot antenna, a 2.5GHz Schottky diode detector, a CPW-to-Microstrip transition, a fully integrated Rectenna element, and a 94GHz slot antenna were designed, fabricated, and tested. Results on the performance of the devices show a great deal of correlation between the simulated and measured data.

To perform an initial study, the CPW-fed narrow slot antenna is designed at 2.5GHz and implemented on an FR-4 board. This investigation serves as the basis for the development of the Rectenna element at millimeter wave frequencies. In order to increase the bandwidth of the slot antenna, a 2.5GHz CPW-fed wide slot antenna with U-shaped tuning stub is realized, which provides a 60% increase in bandwidth while keeping the same radiation characteristics. In addition, a set of simulations is performed to show how a reflector plate affects the radiating properties of the slot antenna. A 2.5GHz square-law detector is also designed, fabricated, and tested in order to rectify the RF signal delivered by the antenna. The fabricated detector presents a well matched condition at the design frequency with a dynamic range found to be from –17dBm to –50dBm. The low frequency Rectenna element prototype is then integrated within a single FR-4 board. This is accomplished by implementing a compact via-less CPW-to-Microstrip transition.

Finally, a 94GHz CPW-fed wide slot antenna is realized on a 10μm high resistivity silicon membrane. This antenna shows a great deal of similarity to the 2.5GHz slot antenna. This low profile antenna presents at least a 10dB return loss over the entire *W* band frequency window. Simulated antenna efficiencies of up to 99% were achieved assuming a perfect conductor.

Chapter 1

Introduction

1.1 Overview

The purpose of this thesis work is to aid in the development of an un-cooled antenna coupled Metal-Insulator-Metal (MIM) diode detector also known as a Rectenna for the purpose of infrared and millimeter wave energy conversion. To date, infrared imaging has being accomplished by quantum and thermal detectors. Quantum detectors provide extremely high sensitivity and fast response; however they require cryogenic cooling mechanisms, which increase the detector's complexity and cost. Thermal detectors, on the other hand, use micro-bolometers, which are simply structured devices with room temperature operation. The downside of micro-bolometer is that it suffers from low sensitivity and slower response than quantum detectors. The proposed Rectenna concept presented here upholds all the advantages of the micro-bolometer described above, while providing a much faster response and higher sensitivity.

R. Baily first proposed the Rectenna concept in 1972 for solar energy conversion [1], [2]. Baily suggested that by using an antenna array in conjunction with a high-speed rectifier, solar radiation could be captured and efficiently converted into DC power providing efficiencies greater than 85%. Due to fabrication restrictions and to the limited understanding of material properties at light frequency, focus was placed in the development of an un-cooled detector for infrared and millimeter wave applications using the same concept proposed by Baily.

Nahas [3] developed the first Rectenna element model consisting of a dipole antenna, a step impedance filter, an extremely fast rectifier, and an output DC filter. This Rectenna element model is presented in Figure 1.1.

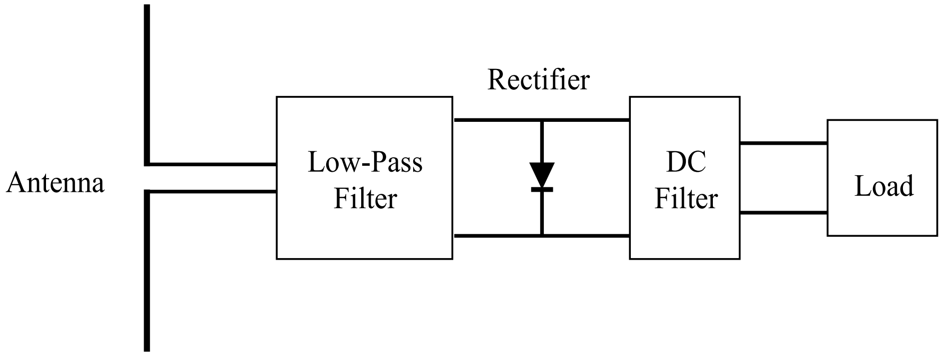

Figure 1.1: Nahas Model for Microwave-to-DC Energy Conversion [3].

In Figure 1.1 it can be observed that the antenna acts as a transducer between free space and the detector circuit by intercepting an incident electromagnetic wave within a frequency range and efficiently delivering an RF signal to the detector circuit. The step impedance filter prevents the higher order harmonics generated by the detector from re-radiating through the antenna, thus increasing the amount of power that is delivered to the load. Nonlinear devices such as Schottky-barrier diodes are responsible for the rectification process, and the output DC filter provides a DC path to the load by separating the high frequency components from the DC signal.

A 2.5GHz prototype of the Rectenna element was initially characterized in order to get familiar with the system and find possible solutions at millimeter and infrared frequencies. During the course of this thesis work three planar antennas, a Schottky diode detector, a CPW-to-Microstrip transition, a fully integrated Rectenna element, and a 94GHz slot antenna were implemented. These elements presented good agreement with the expected results. This was accomplished by dividing the project into four different sections. First a 2.5GHz CPW-fed narrow slot antenna was optimized so that it provided extremely high efficiencies. A slot antenna design was chosen due to its similarities to the conventional ½λ dipole with the slot antenna's electric field being orthogonal to the dipole's electric field. In addition, integrating tuning stubs within the aperture can easily increase the bandwidth of the antenna while maintaining the same radiation characteristics. Furthermore, slot antennas could be used to achieve both unidirectional and bidirectional radiation. Unidirectional radiation is achieved by placing a reflector plate parallel to the slot antenna on the opposite side of the substrate.

In order to complete the Rectenna element, a square-law detector circuit using a commercially available Schottky diode was designed, fabricated, and tested. A square-law detector essentially serves as a power-measuring device with multiple applications in RF circuitry. These detectors are commonly used in radiometers, power-scavenging systems, RFID tags, and in numerous other mobile applications. The 2.5GHz detector circuit was designed using the HSMS-2850 Schottky diode to rectify the RF signal delivered by the antenna. In order to implement the Rectenna element within a single board, a via-less CPW-to-Microstrip transition was employed. Transitions are commonly used to match the propagation modes of different transmission lines or waveguides in order to minimize reflections and power loss at a given interface.

After getting acquainted with the problems at lower frequencies, a 94GHz wide slot antenna with tuning stubs was characterized. The antenna was fabricated on a 10μm high resistivity silicon membrane that serves to prevent surface waves from propagating through the substrate, thus increasing the overall efficiency of the antenna. It will be shown that even though the jump in frequency is extensive, the performance of the antenna is comparable to that of the 2.5GHz antenna.

1.2 Motivation

The Rectenna concept has great potential not only for millimeter wave applications and infrared energy conversion, but also for efficiently collecting solar radiation and converting it into DC power. Theoretically, by utilizing the Rectenna concept conversion efficiencies approaching 100% have been predicted [4], which surpass the current state of the art solar cells efficiencies. In literature [5], efficiencies of up to 85% have been reported at lower frequencies. The successful development of a Rectenna element at millimeter wave frequencies can also reduce the overall cost of millimeter wave sensory systems. This device can also provide multiple applications for military and commercial industries such as: concealed weapon imaging, automatic braking, radiometry, and missile guidance systems.

1.3 Thesis Organization

This thesis work is divided into five chapters. The first chapter consists of the introduction, composed of the motivation behind the project, thesis organization, and major contributions. Chapter 2 presents the design of two 2.5GHz CPW-fed slot antennas. An in-depth analysis of slot antennas is provided along with a brief theoretical description of slot antennas. The effects of a reflector plate on the impedance and radiation characteristics of the antenna are also analyzed through a set of Agilent's Momentum simulations. The optimization of a conventional CPW-fed ½λ slot antenna that achieves efficiencies of up to 99% is also presented. In order to increase the bandwidth of the antenna, a CPW-fed wide slot antenna with U-shaped tuning stubs is implemented.

Chapter 3 shows the design of a conventional Schottky diode detector circuit with distributed elements as the matching network and filtering mechanism. A sensitivity analysis of the detector circuit is also performed in order to demonstrate how the matching network affects the overall performance of the square-law detector. In addition, a CPW-to-Microstrip transition is employed in order to integrate the antenna and the detector circuit within a single FR-4 board. The separate Rectenna elements connected by a Male-to-Male (M-M) connector are also analyzed and compared to the fully integrated Rectenna element by measuring its square-law characteristics and sensing properties. Finally, an in-depth comparison between the simulated and measured data is presented.

Chapter 4 of this thesis discusses the design, fabrication, and characterization of a 94GHz slot antenna. This antenna was designed on top of a 10μm high resistivity silicon membrane and presented simulated efficiencies of up to 99%. A brief description of surface waves within the silicon substrate along with a parametric study performed in Momentum to study the effects of the substrate thickness on the antenna radiation properties is provided.

1.4 Contributions

Many contributions were made during the course of this thesis work. For instance, a 2.5GHz Rectenna element was successfully integrated within a single FR-4 board and tested for its sensing properties. In the process, a compact via-less CPW-to-Microstrip transition was implemented presenting extremely low loss at the design frequency of

2.5GHz. In addition, a 94GHz wide slot antenna was fabricated on a 10μm high resistivity silicon membrane and measured to validate its performance over the entire *W* band frequency window. To the best of the author's knowledge this is the first time this specific antenna has been implement on a 10μm high resistivity silicon membrane.

Chapter 2

2.5GHz Slot Antenna Design

2.1 Introduction

Aperture antennas have been studied for the past fifty years becoming a separate research area of their own [6]. Throughout the years many configurations have been realized such as: square, rectangular, circular, and elliptical apertures just to mention a few. Aperture antennas are also very practical for space applications, since they can be flush-mounted on the metallic surface of a spacecraft or aircraft. In addition, strip and slot combinations offer an additional degree of freedom in the design of microstrip antennas. This thesis work mainly concentrates on slot antennas and their characteristics.

Throughout this chapter, a slot antenna is characterized, which is the first component of the Rectenna element. A brief theoretical description of slot antennas and the terms used to describe them are presented. In addition, the antenna properties are shown by presenting two low frequency prototype antenna designs operating at 2.5GHz. Also, some of the advantages of using a CPW-fed slot antenna over patch and microstrip-fed slot antennas are mentioned in Section 2.3. Finally, the optimized antenna prototypes are fabricated and tested showing a great deal of correlation to the simulated data.

2.1.1 Background Theory

A slot antenna consists of a slot cut in a metal surface with an orthogonal feeding mechanism in most cases. The slot dimensions are usually smaller than a wavelength and much smaller than the ground plane in which they reside. Figure 2.1 illustrates a conventional center-fed slot antenna presented by Garg et al. [7]. The slot antenna can be efficiently excited by physically shorting the microstrip line through the substrate into the far edge of the slot as illustrated in Figure 2.1a. The most commonly used feeding topology is presented in Figure 2.1b. In this case, an open-circuited stub is terminated approximately at a ¼λ from the edge of the slot, which presents an electrical short circuit at the edge of the antenna. Other feeding techniques have been utilized [6-12] such as the one mentioned subsequently in this chapter.

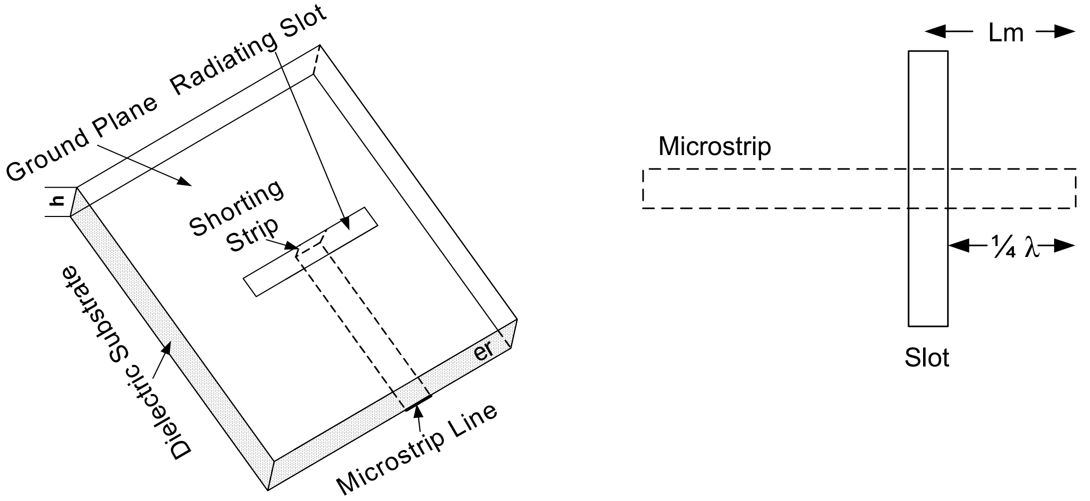

(a) (b)

Figure 2.1: (a) Center-fed Slot Antenna Short Circuited Through the Substrate. (b) Microstrip Slot Antenna Terminated with an Open-circuited Stub.

The microstrip conductor excites the slot by coupling a voltage potential across the aperture forming a distributed electric field. Within the aperture, the voltage maximum and current minimum occur at the center of the slot, while the voltage minimum and current maximum take place at the two edges of the slot. The fringing fields, which are caused by current crowding at the edges of the slot, increase the electrical length of the antenna [6]. Thus, the physical length *L* of the slot antenna is denoted by the equation 2.1

$$L = \frac{\lambda_S}{2} - \Delta l \tag{2.1}$$

where λ_S is the wavelength in the slot and Δl is the electrical length caused by the currents flowing around the edges of the slot [6]. The current and voltage distribution of the slot antenna is presented in Figure 2.2, which is key to understanding some of the impedance matching techniques discussed in the subsequent sections.

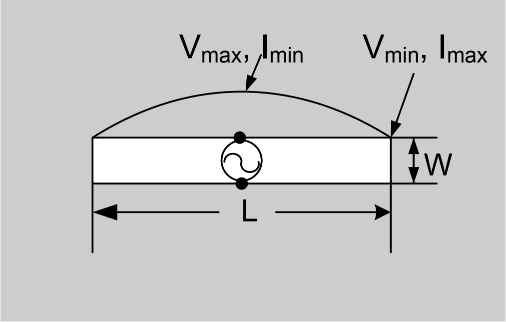

Figure 2.2: Voltage and Current Distribution Around the Slot.

2.1.2 Input Impedance

According to Bahl and Bhartia [6], the input impedance of the antenna consists of a series combination of the radiation resistance *R* and the reactive component *X*. At resonance the reactive component of the impedance is taken to be zero; leaving a purely real component. Literature has reported that the impedance of the resonant center-fed slot antenna is approximately 550Ω, which is far from being matched to the feeding mechanism. It should be mentioned that this high impedances depend on the substrate characteristics. Due to the voltage and current relationship presented in Figure 2.2, the impedance of the antenna decreases towards the edges of the slot, and in most cases, different feeding techniques can be used to match the antenna's input impedance to the characteristic impedance of the line, which usually increases the bandwidth of the antenna [6]. Figure 2.3 presents some of the feeding techniques used in [8], [9] to reduce the antenna's resistance.

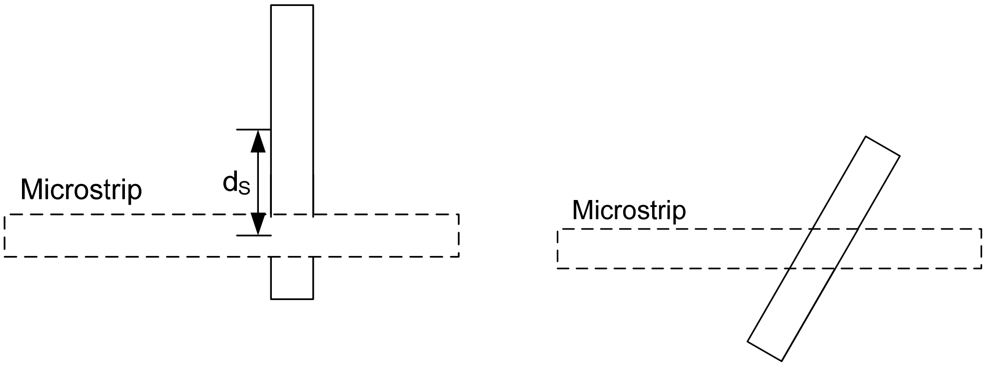

(a) (b)

Figure 2.3: Different Feeding Methods Used to Decrease the Slot Antenna Input Impedance. (a) Offset Microstrip-fed and (b) Center-fed but Inclined Microstrip-fed.

As suggested by Yoshimura [8], the radiation resistance of the slot antenna can be reduced by feeding it at a point away from the center of the slot, which is also known as the offset-fed slot antenna illustrated in Figure 2.3a. For most slot antennas, the impedance mainly depends on the width of the slot, the location of the feed point, the size and width of the tuning stubs, and the dielectric material used. The other feeding technique is depicted in Figure 2.3b, which consists of inclining the slot about its axis. Yoshimura [8] also stated that the resonant length of the center-fed slot antenna is greater than the resonant length of the offset-fed slot. As a rule of thumb, the resonant length of the offset-fed slot antenna usually lies between .4λ and .5λ [6].

The other technique used to reduce the impedance of the antenna consists of stub tuning the slot antenna as suggested by Pozar [10]. This technique is similar to that of Figure 2.1b except that the length of the stub is no longer terminated at a ¼ λ from the edge of the slot. The microstrip tuning stubs change the resonant frequency of the antenna so that the input resistance matches with the feed line impedance at the new resonant frequency [7]. The stub can be tuned to cancel out the reactive part of the impedance and reduce the radiation resistance of the antenna as well. In addition, Yoshimura [8] declared that the distortion created at the feeding mechanism has minimum or no effect on the far field radiation pattern of the antenna.

2.1.3 Radiation Pattern

The easiest way to demonstrate the radiation characteristics of the slot antenna is to consider it as a dual value problem to the dipole antenna case. As illustrated in Figure 2.4, both antennas are excited at their center which is represented by a voltage source.

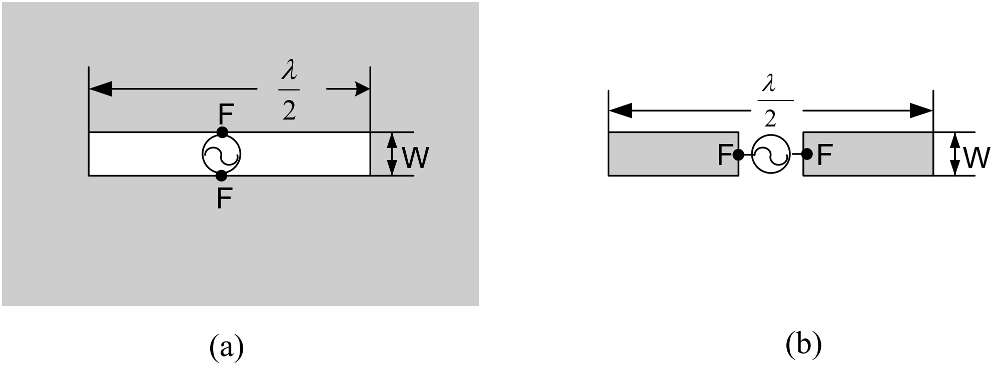

Figure 2.4: (a) ½λ Slot Antenna on an Infinite Ground Plane, (b) Complementary ½λ Printed Dipole Antenna.

Booker [11] stated that the radiation pattern of the slot is the same as the complementary half wavelength printed dipole represented in Figure 2.4b, with their fields being orthogonal to each other. The two cases can be treated as a boundary-value problem by finding the appropriate solution to Maxwell's equations while satisfying the proper boundary conditions. Where, E and H are the electric and magnetic fields of the aperture respectively.

$$\nabla^2 E = \mu\varepsilon E \tag{2.2}$$

$$\nabla^2 H = \mu\varepsilon H \tag{2.3}$$

Either of the above wave equations can be solved to satisfy the following boundary conditions. For the dipole depicted in Figure 2.4b, the tangential components of the magnetic field are zero outside the perimeter of the dipole, and the normal components of the magnetic field are zero within the perimeter of the dipole. For the slot in Figure 2.4a, the tangential components of the electric field are zero outside the perimeter of the slot and the normal components of the electric field are zero within the perimeter of the slot. From the above boundary conditions it is observed that both problems are similar, differing only by the fact that the electric and magnetic fields are interchanged. This is illustrated in Figure 2.5. It should be noted that if the slot antenna in Figure 2.5a is rotated by 90° about the y-axis the electric and magnetic fields vectors are aligned in the same direction.

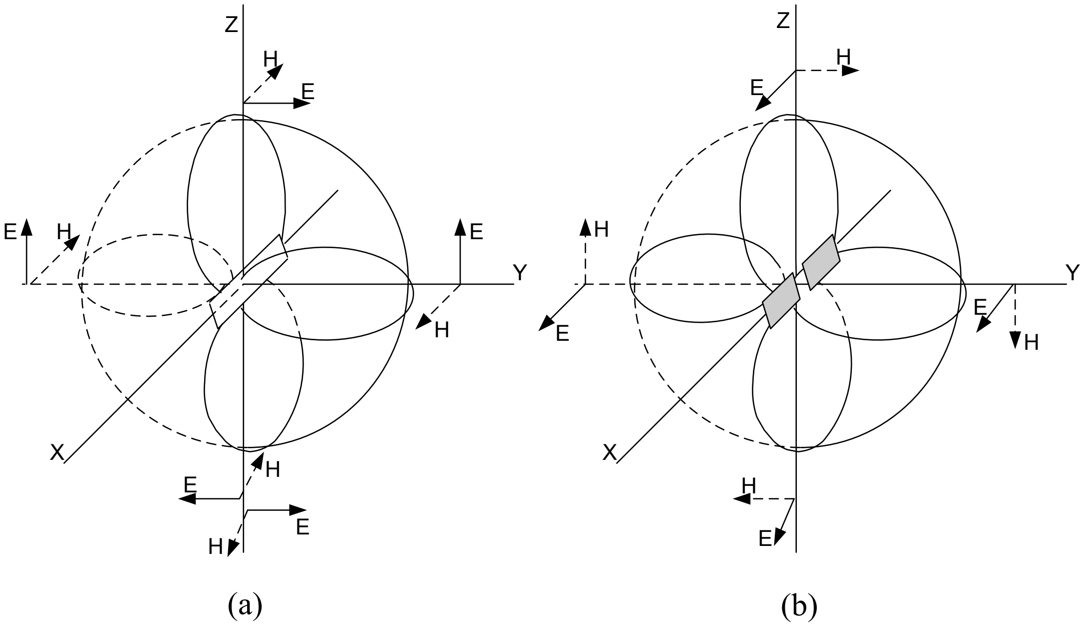

(a) (b)

Figure 2.5: (a) Radiated Fields of a Slot Antenna on an Infinite Ground Plane, (b) and Radiated Fields of the Complementary Dipole Antenna.

The electric field for the slot antenna has the same doughnut shape of a ½λ dipole antenna. Also, since the electric and magnetic fields of both antennas are interchangeable, the slot antenna's electric and magnetic fields can be expressed as a function of the magnetic and electric fields of the dipole antenna. This is given by 2.4 and 2.5,

$$E_S = k_1 H_d \tag{2.4}$$

$$H_S = k_2 E_d \tag{2.5}$$

where E_S and H_S are the electric and magnetic fields in the slot; and E_d and H_d are the electric and magnetic fields in the dipole respectively [6]. For a full derivation of the slot antenna's electric and magnetic fields refer to [6], [7], and [8].

Slot antennas can present both linear and circular polarization. For the narrow slot antenna depicted in Figure 2.6, the radiation normal to the ground plane of the horizontal slot in Figure 2.6a is vertically polarized while the radiation normal to the ground plane of the vertical slot presented in Figure 2.6b is horizontally polarized.

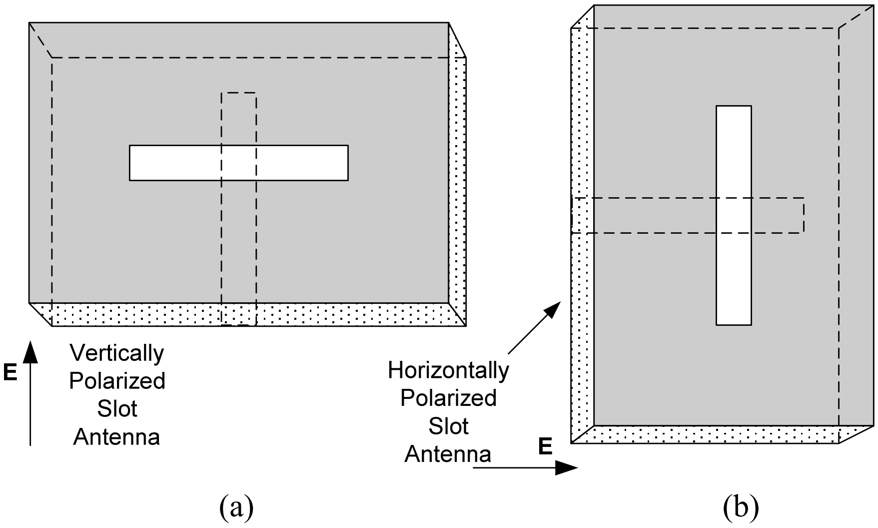

Figure 2.6: Slot Antenna Fed by a Microstrip Line with (a) Vertical Polarization, and (b) Horizontal Polarization.

2.2 Motivation for Using a CPW-fed Slot Antenna

CPW-fed slot antennas have many advantages over other microstrip radiators. For instance, slot antennas have the advantage of providing bidirectional and unidirectional radiation. Unidirectional radiation is achieved by placing a reflector plate parallel to the substrate. In Section 2.5 of this chapter a set of simulations were performed in Agilent's electromagnetic simulator "Momentum" to demonstrate the reflector spacing effect on the impedance and radiation characteristics of the antenna. Table 2.1 summarizes some of the characteristics and advantages of slot antennas over patch antennas [7].

Table 2.1: Comparison Between the Slot and Patch Antenna Characteristics.

Characteristics	Patch	Slot
Analysis and design	Easy	Easy
Fabrication	Very easy	Very Easy
Tolerance in fabrication	Critical	Not very critical
Profile	Thin	Thin
Shape flexibility	Any shape	Limited
Radiation fields	Unidirectional	Unidirectional and bidirectional
Polarization	Linear and circular	Linear and circular
Bandwidth	Narrow	Wide
Dual frequency operation	Possible	Possible
Spurious radiation	Moderate	Low
Isolation between radiating elements	Fair	Good
Frequency scanning	Easily possible	Possible
Cross-polarization level	Low	Very low
End-fire antenna	Not possible	Possible

The CPW-fed slot antenna was chosen for this project because it provides many advantages over the conventional microstrip-fed slot antenna. For instance, the CPW-fed slot antenna does not require alignment since the entire structure is fabricated on one side of the substrate. This feeding technique reduces the fabrication error tolerance found in microstrip and coax fed slot antennas. In addition, CPW lines can be easily integrated with monolithic components within the same surface reducing the overall cost of the device.

2.3 CPW-fed Narrow Slot Antenna

In this section an experimental analysis on an offset CPW-fed narrow slot antenna is presented. Some of the feeding topologies published in the literature [7], [12] are depicted in Figure 2.7. In the center-fed CPW slot antenna illustrated in Figure 2.7a the two electric field components of the CPW aperture excite the slot antenna across its width. As mentioned by [7], the CPW apertures' radiated fields almost add out of phase in the far field providing extremely low cross-polarization. The same feeding technique used to reduce the radiation resistance of the antenna also applies to the CPW-fed slot antenna as shown in Figure 2.7b. The problem with this feeding mechanism is that it requires wire bonding in order to stabilize the ground plane and suppress higher order modes that can provide cross-polarization. The other feeding mechanisms are depicted in Figure 2.7c and Figure 2.7d. The inductively coupled feeding method is found to be extremely useful for series-fed array configurations [7].

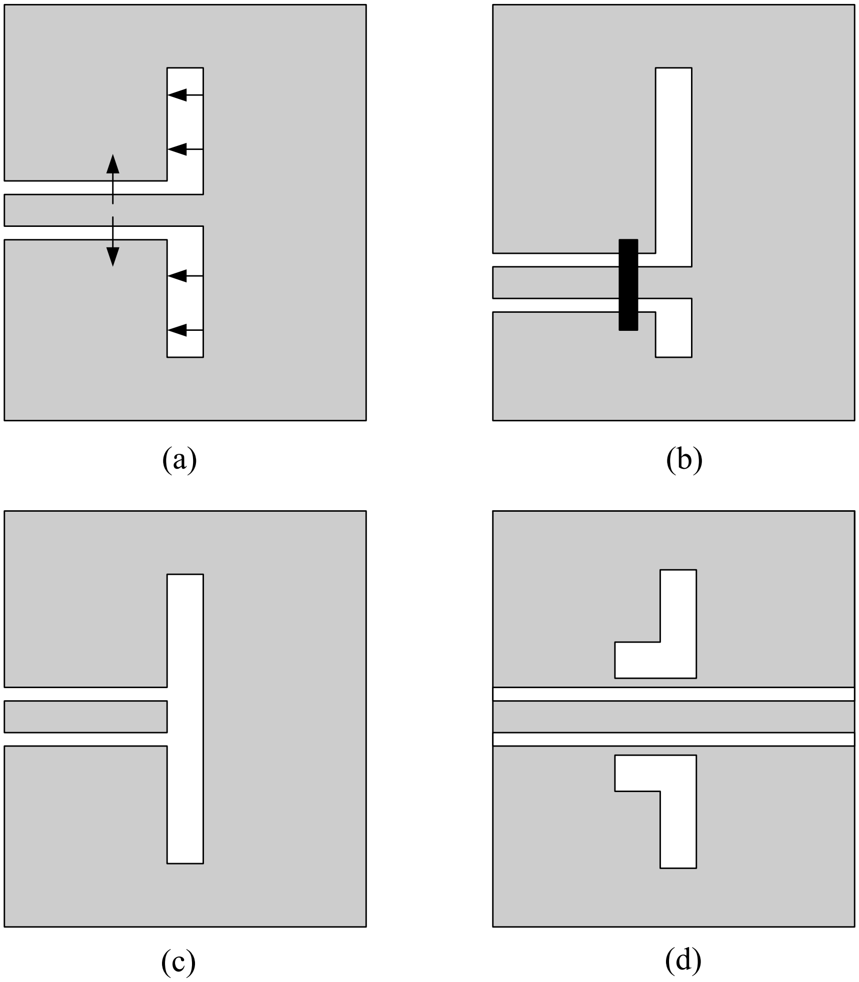

Figure 2.7: CPW-fed Slot Antenna Feeding Mechanisms: (a) Center-fed Slot Antenna, (b) Offset-fed Slot Antenna with Bond Wire for Stability, (c) Capacitively Coupled, and (d) Inductively Coupled Slot Antenna.

The slot antenna design mentioned in this section was characterized using Momentum. First, a 2.5GHz center-CPW-fed slot antenna was simulated to analyze its characteristics and to become familiar with the current distribution around the antenna. As illustrated in Figure 2.8, the electric current density is more intense at the edges of the slot, which agrees well with literature. In addition, the radiation pattern possesses the same doughnut shape as that of the dipole antenna and presents a high degree of symmetry about its axis.

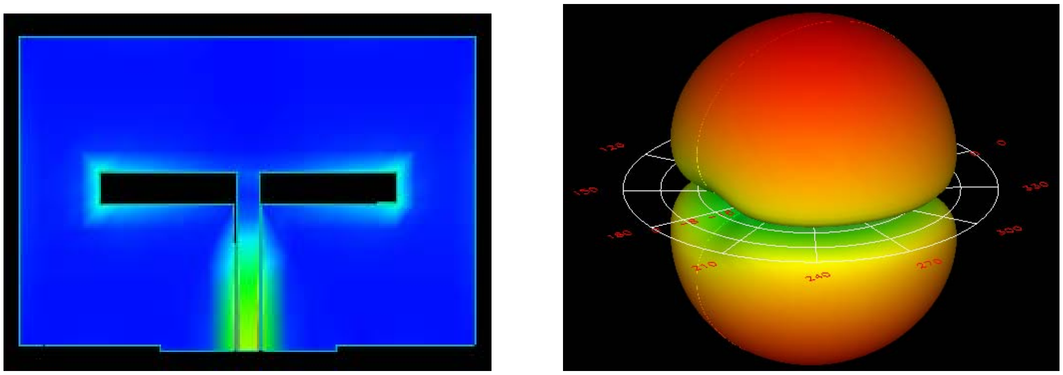

(a) (b)

Figure 2.8: (a) Current Density Distribution of the Center-fed Slot Antenna, and (b) Radiated Electric Field.

The resonant length of the antenna is found to be approximately 40mm with a complementary width of 4mm. An FR-4 board ($\varepsilon_r = 4.3$) was chosen for this design. Figure 2.9 illustrates the simulated results of the center-fed slot antenna. The resonance occurs at approximately 2.5GHz, but its impedance is far from being matched to the characteristic impedance of the CPW line. As mentioned before, the radiation resistance of the slot antenna can be matched to a 50 Ω transmission line by feeding it at a certain distance d_S away from the center of the slot. This feeding technique is illustrated in Figure 2.3a. A parametric study was performed on Momentum to find the optimum offset point. The distance of the offset point was varied from d_S=0mm to d_S=12mm, and the impedance of the antenna was monitored. The simulated results are depicted in Figure 2.10.

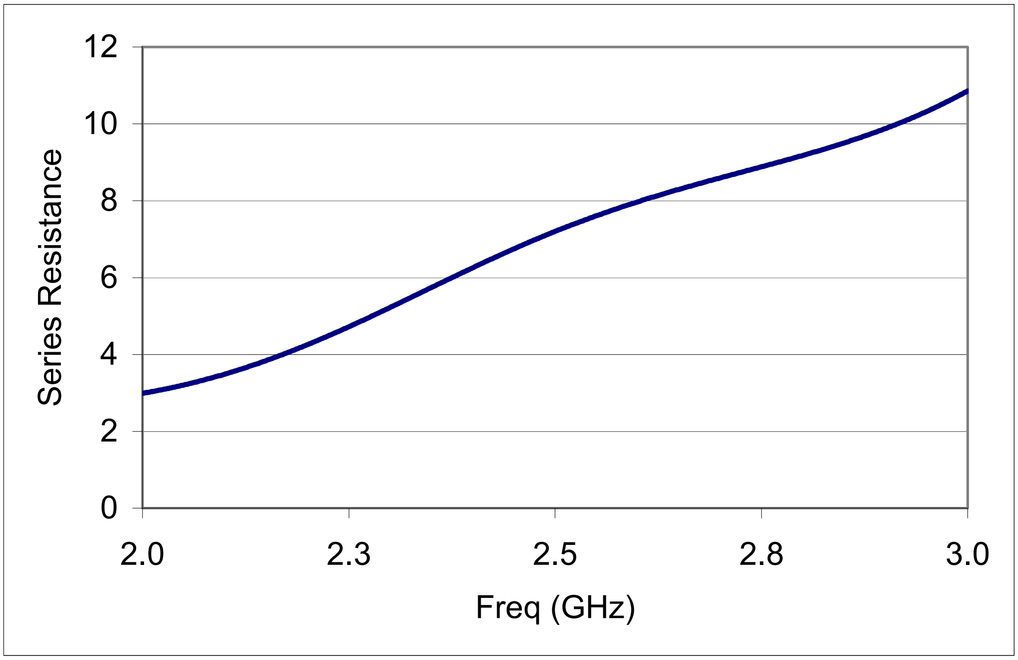

(a)

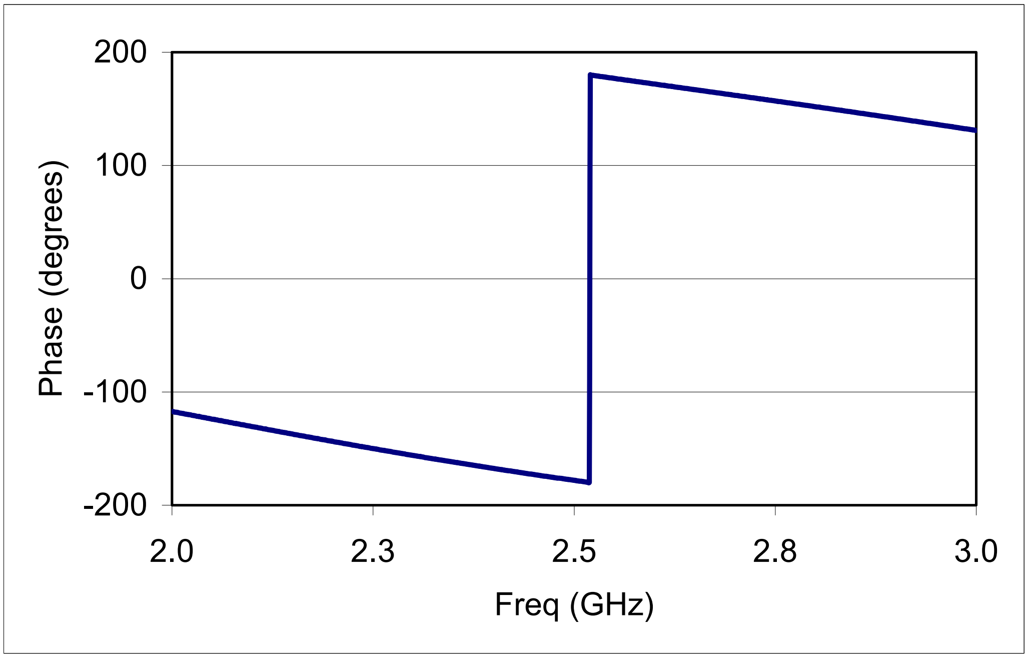

(b)

Figure 2.9: Center-fed Slot Antenna Results. (a) Series Resistance and (b) Phase.

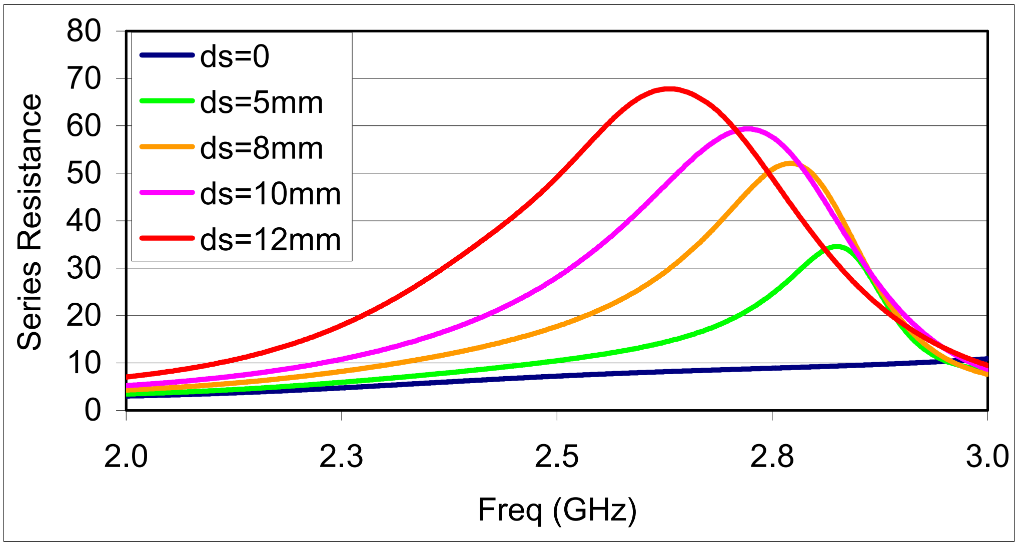

Figure 2.10: Effect of the Offset Point d_S on the Series Resistance of the Slot Antenna.

It is observed that as the feeding point approaches the edge of the slot antenna the aperture impedance increases. The plotted impedance illustrated in Figure 2.10 contradicts the impedances reported in literature [7]. This is due to the fact that the simulated impedance is referenced at the edge of the antenna, which is approximately a ¼λ away from the slot. Figure 2.11 presents the normalized impedance of the antenna in a Smith Chart. From this plot it is evident that the impedance at the center of the slot is extremely low and increases as the feeding point moves towards the edge of the antenna.

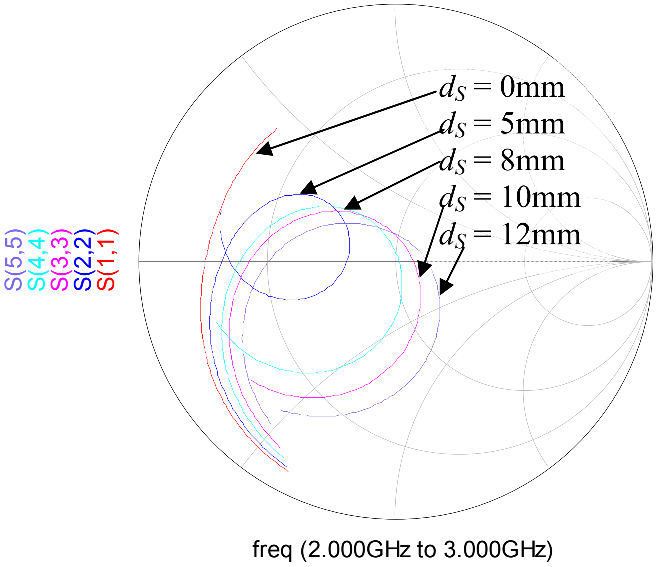

Figure 2.11: Normalized Impedance of the Slot Referenced at the Edge of the Antenna.

In order to find the actual impedance of the slot, the simulated S-parameters were extracted from the Momentum simulation and imported into Agilent's Advanced Design System (*ADS*). Then, a ¼λ CPW line was added to obtain the actual impedance of the aperture. The complete schematic utilized to shift the reference plane to the edge of the slot and the simulated results are depicted in Figure 2.12 and Figure 2.13.

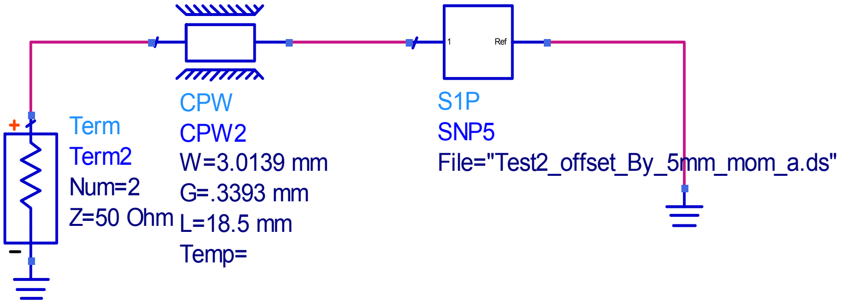

Figure 2.12: ADS Schematic Utilized to Find the Impedance of the Slot Antenna.

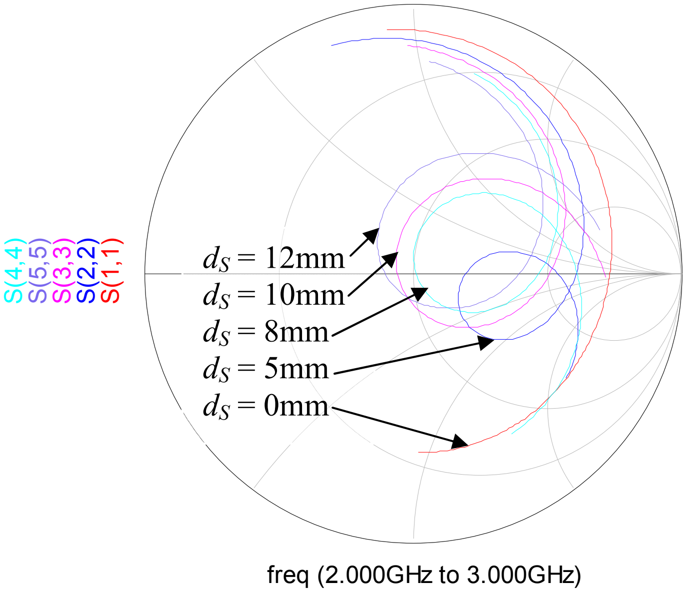

Figure 2.13: Normalized Impedance of the Slot Referenced at the Slot.

As illustrated in Figure 2.13, the S-parameters are rotated on the Smith Chart by ¼λ placing the reference plane at the edge of the slot. The results show that the slot impedance is very high when it is center-fed and drops as it approaches the edge of the aperture, which agrees well with literature. The actual series resistance of the center-fed slot antenna was found to be approximately 420**Ω**, and the optimal feeding point was found to be at d_S = 8mm. As mentioned before, the resonant length of the offset slot antenna is smaller than the center-fed slot antenna. Figure 2.14 illustrates this behavior.

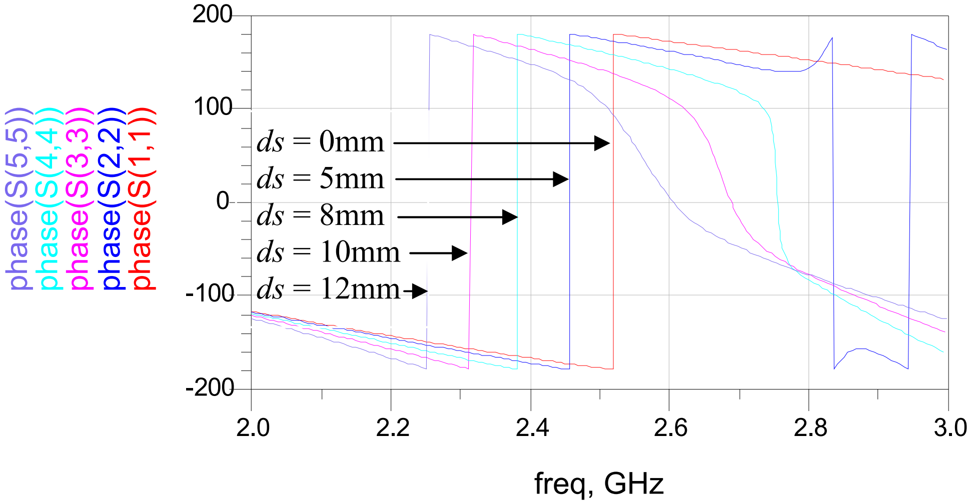

Figure 2.14: Phase of the Slot Antenna at d_S = 0, 5, 8, 10, and 12mm.

The downside of the offset-CPW-fed narrow slot antenna is that it requires wire bonding in order to balance the CPW's ground plane. The failure to balance the ground planes can create other operating modes causing non-desired cross-polarization. Figure 2.15 presents a comparison between the center and the offset-fed slot antenna's simulated radiation pattern. It is observed that the simulated radiation pattern of the center-CPW-fed slot antenna possesses extremely low cross-polarization, while the offset-CPW-fed slot antenna provides a cross-polarization that is 10dB below the co-polarized pattern. It should be mentioned that the offset-CPW-fed slot antenna was simulated without a wire bond.

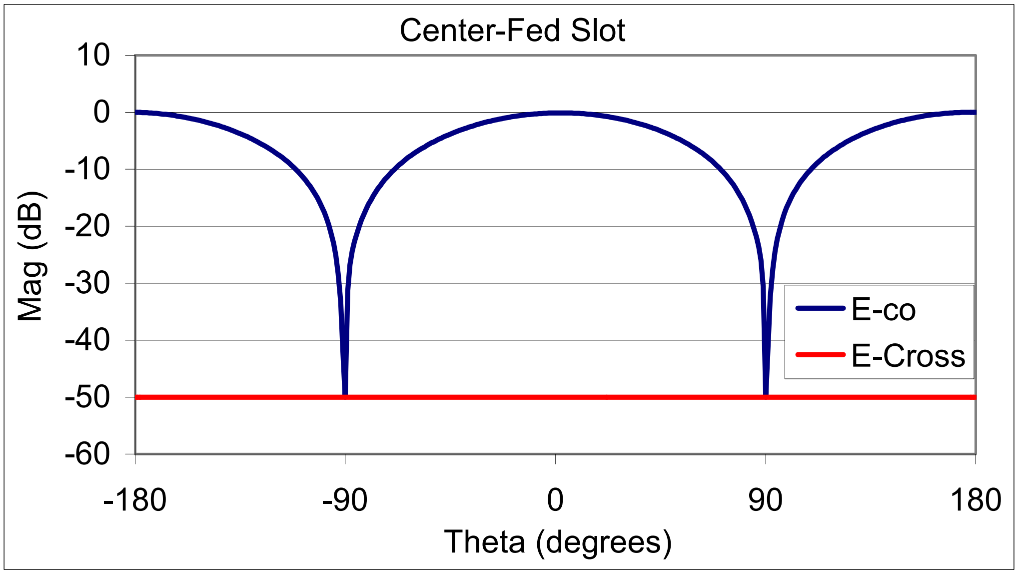

(a)

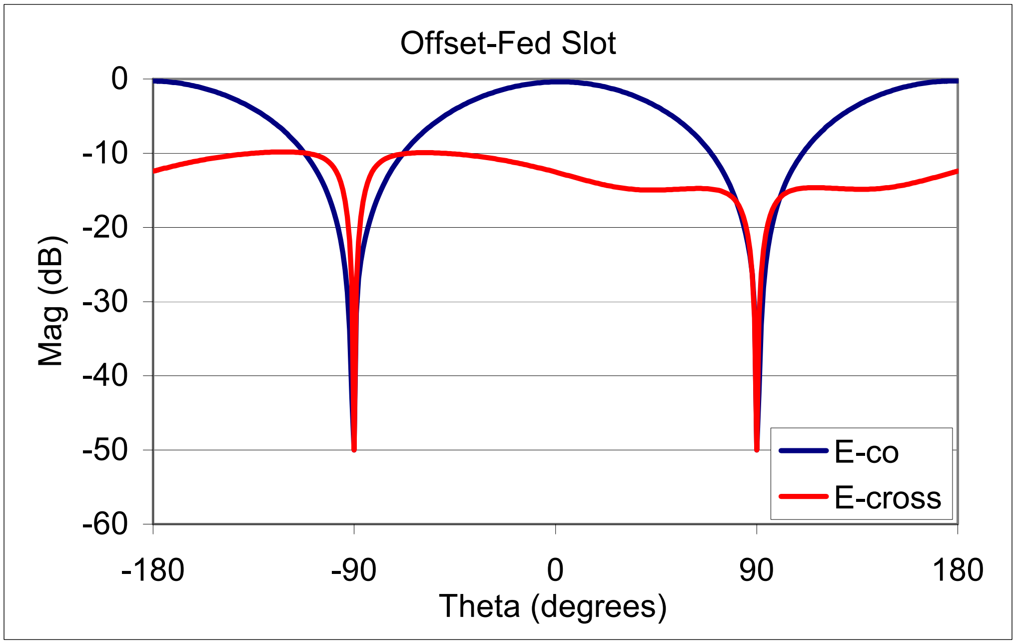

(b)

Figure 2.15: Linearly Polarized Radiation Pattern Obtain in Momentum. (a) Center-fed Slot Antenna, (b) Offset-fed Slot Antenna.

Table 2.2 also presents a comparison of the center and offset-fed slot simulated antenna parameters.

Table 2.2: Comparison Between the Center-fed and Offset-fed Simulated Antenna Parameters.

Simulated Antenna Parameter	Center-fed	Offset-fed
Power Radiated (mW)	1.2	2.5
Directivity (dB)	4.73	4.68
Gain (dB)	4.71	4.65
Efficiency	99%	99%

2.4 Antenna Efficiency and Gain Definitions

According to Balanis [13], the overall efficiency η_0 of the antenna is provided by equation 2.6.

$$\eta_0 = \eta_r \eta_c \eta_d \tag{2.6}$$

where:

η_r is the reflection (mismatch) efficiency = $\left(1 - |\Gamma|^2\right)$

η_c is the conduction efficiency

η_d is the dielectric efficiency

and Γ is the voltage reflection coefficient at the input terminals of the antenna given by equation 2.7.

$$\mathrm{T} = \frac{Z_{IN} - Z_0}{Z_{IN} + Z_0} \tag{2.7}$$

where Z_{IN} is the input impedance of the antenna, and Z_0 is the characteristic impedance of the line. Since the dielectric and conduction efficiencies are somewhat cumbersome to calculate and cannot be obtained separately from measurements, they are usually combined to give the antenna radiation efficiency $\eta_{cd} = \eta_c \eta_{d.}$. This equation can be used to relate the gain and the directivity of the antenna.

Balanis [13] stated that according to the IEEE standards, “gain does not include losses arising from impedance mismatches (reflection losses) and polarization mismatches (losses)." The gain of an antenna is defined as "the radiation intensity radiated in a certain direction compared to an isotropic radiator." An isotropic radiator is defined as "a hypothetical lossless antenna having equal radiation in all directions." In practice, relative gain is used, and is defined as "the ratio of the power gain in a given direction to the power gain of a reference antenna in its referenced direction" [13]. If the direction is not specified, the power gain is measured in the direction of maximum radiation. Equations 2.8 and 2.10 illustrate how the gain and directivity of the antenna are related by the efficiency of the antenna. The gain of the antenna $G(\theta,\Phi)$ can be expressed as

$$G(\theta,\phi)=\eta_{cd}\left[4\pi\frac{U(\theta,\phi)}{P_{rad}}\right] \tag{2.8}$$

where

$$P_{rad}=\eta_{cd}Pin \tag{2.9}$$

and the directivity is given by equation 2.10.

$$D(\theta,\phi)=4\pi\frac{U(\theta,\phi)}{P_{rad}} \tag{2.10}$$

Now if the equation 2.10 is substituted into equation 2.8, it is observed that the gain and the directivity are related by the efficiency of the antenna expressed in equation 2.11.

$$G(\theta,\phi)=\eta_{cd}D(\theta,\phi) \tag{2.11}$$

In addition, the maximum gain of the antenna is directly related to the maximum directivity by finding the maximum radiation intensity of the antenna.

$$G_0=G(\theta,\phi)\big|_{MAX}=\eta_{cd}D(\theta,\phi)\big|_{MAX}=\eta_{cd}D_0 \tag{2.12}$$

To calculate the overall gain of the antenna, which is defined as the absolute gain of the antenna G_{0abs} [13], the transmission line mismatch and polarization losses have to be included in the analysis. If the antenna is perfectly matched to the feeding mechanism, the absolute gain is equal to the relative gain of the antenna. From the above expressions and the simulated antenna parameters, efficiencies of up to 99% were achieved under the assumption that copper is a perfect conductor.

2.5 CPW-fed Wide Slot Antenna with Tuning Stubs

For some applications wide operational bandwidths are desired. The proposed antenna presented in this section provides many advantages over the narrow slot antenna presented in the previous section. These include wider bandwidth, low cross-polarization, and added tuning capabilities. In addition, wide slot antennas are less sensitive to fabrication errors and alignment issues found in narrow slot antennas [6]. The antenna presented in this section is composed of a CPW-fed wide slot utilizing a U-shaped tuning stub to achieve broadband operation.

The bandwidth of an antenna can be calculated in one of two ways. Let f_U and f_L be the upper and lower frequency of operation, respectively, in which the impedance or other performance characteristics of the antenna do not change dramatically. The impedance bandwidth is usually measured at a VSWR ≤ 2 or a RL $\leq$ 10dB which is equivalent. In most cases the antenna’s bandwidth is represented as a percentage expressed by equation 2.13

$$BW = \frac{f_U - f_L}{f_C} x100 \tag{2.13}$$

where f_C is defined as the center frequency of operation or as the design frequency, in this case 2.5GHz. According to [14], an antenna is said to be broadband if its impedance does not change significantly over about an octave $(f_U / f_L = 2)$ or more.

Wide slot antennas inherently present wider bandwidths than narrow slot antennas, and the addition of tuning stubs creates multiple resonances which increases the overall bandwidth of the antenna. Throughout the literature [15], [16], [17] many stub tuning techniques have been realized providing impedance bandwidths of about 35% to 60%. Chair [18] reported a CPW-fed wide slot antenna with U-shaped tuning stubs in conjunction with a back reflector for ultra-wideband operation that presented impedance bandwidths of up to 120% measured at a RL $\leq$ 10dB.

Even though this project does not require ultra-wideband operation, the same tuning topology presented in [18] was realized. Figure 2.16 illustrates the proposed antenna and slot dimension relative to a wavelength.

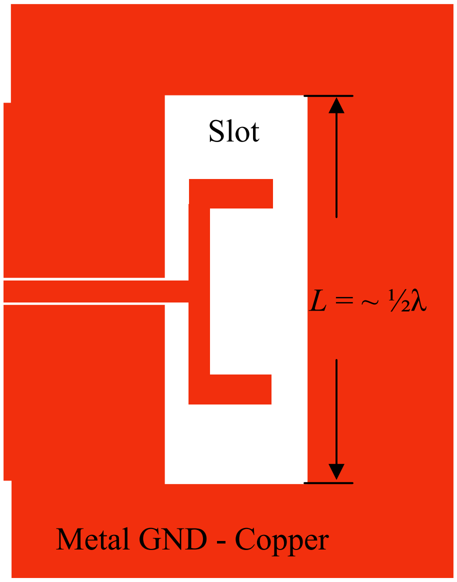

Figure 2.16: CPW-fed Wide Slot Antenna with U-shaped Tuning Stub Layout.

The antenna depicted in Figure 2.16 presents the same current and voltage distribution as the narrow slot antenna. In addition, this antenna provides the same doughnut shaped radiation characteristics found in the narrow slot antenna and the ½λ dipole depicted in Figure 2.17b.

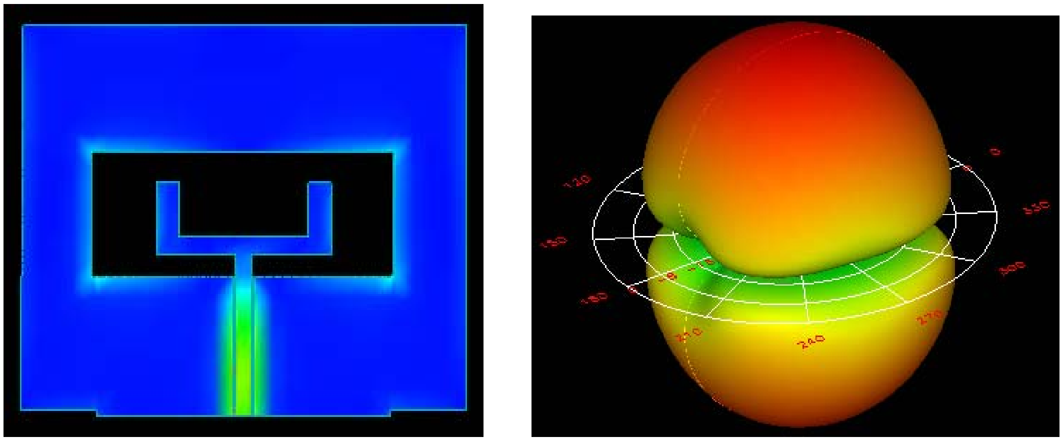

(a) (b)

Figure 2.17: (a) Current Density Distribution of the Center-fed Wide Slot Antenna with U-shaped Tuning Stub, and (b) 3D Radiated Electric Field.

As mentioned before this antenna has many advantages over the narrow slot antenna. For instance, a matched condition is achieved without the need of an offset feed point providing extremely low cross-polarization. The antenna's resistance is mainly controlled by the width of the slot, the length and width of the tuning stub, the location of the stubs, and the dielectric material. The simulated RL and phase of the antenna are presented in Figure 2.18, and it is important to mention that the reference plane in the simulations was placed at the edge of the antenna. The antenna is well matched over a large frequency range. It should also be noted that the antenna presents multiple resonances. These resonances are mainly due to the length of the slot, the position of the stubs, and the length of the stubs increasing the overall bandwidth of the antenna.

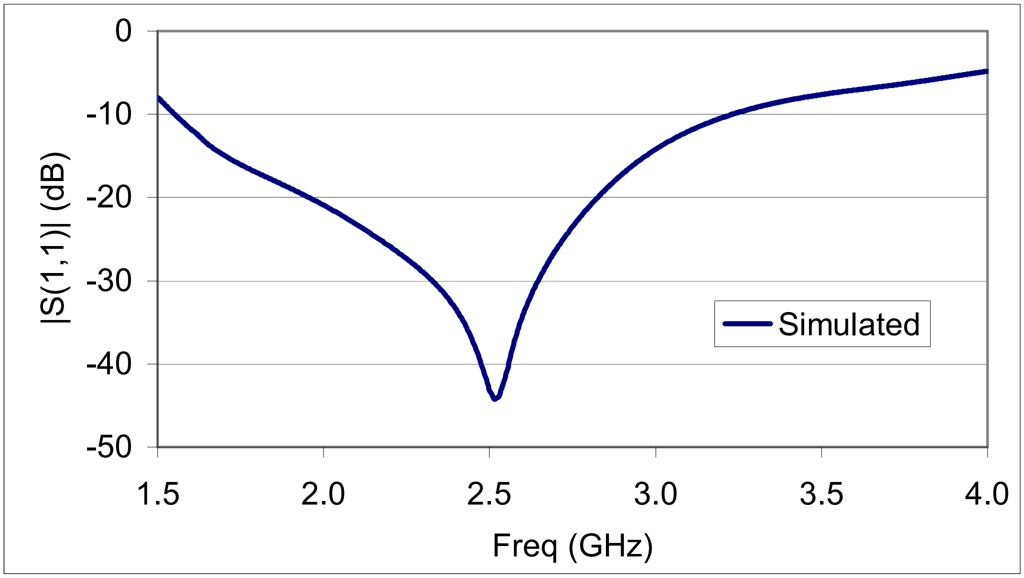

(a)

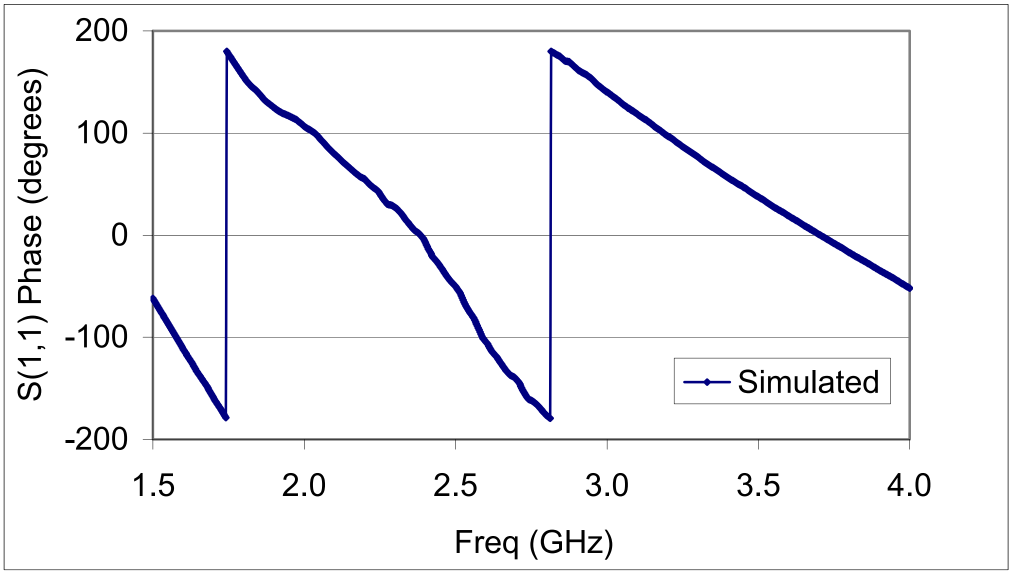

(b)

Figure 2.18: (a) Wide Slot Antenna Return Loss, and (b) Wide Slot Antenna Phase.

Even though the focus of the antenna design was for it to be well matched at the design frequency rather than an ultra-wideband operation, broadband operation was achieved with bandwidths of up to 70% referenced to a VSWR ≤ 2, which is depicted in Figure 2.19.

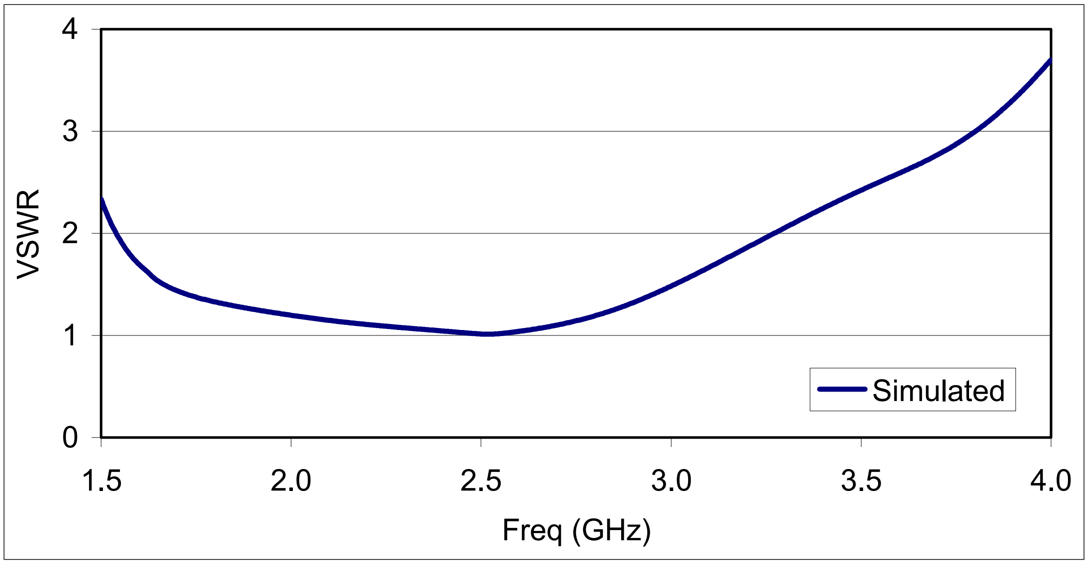

Figure 2.19: Simulated VSWR of the CPW-fed Wide Slot Antenna with U-shaped Tuning Stubs.

2.6 Antenna Simulations with Reflector in Place

As mentioned before, unidirectional radiation can be achieved by placing a reflector plate parallel to the substrate as illustrated in Figure 2.20.

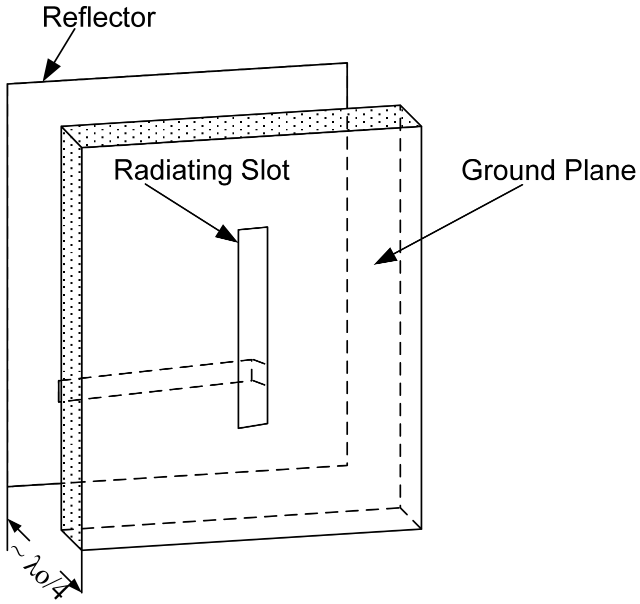

Figure 2.20: Microstrip-fed Slot Antenna with a Plane Reflector for Unidirectional Radiation.

In this section the effect of the reflector plate spacing on the impedance and radiation characteristics of the antenna is presented. According to [6] and [7], the RL of the antenna can change dramatically when the antenna to reflector plate spacing approaches ½λ, and hardly changes as the reflector plate spacing approaches ¾λ - 1λ. A parametric study to demonstrate this behavior was performed in Momentum. The reflector spacing d_r was varied from 1/8λ to 1λ while monitoring the RL and the radiation pattern of the antenna. Figure 2.21 presents the simulated results of this study.

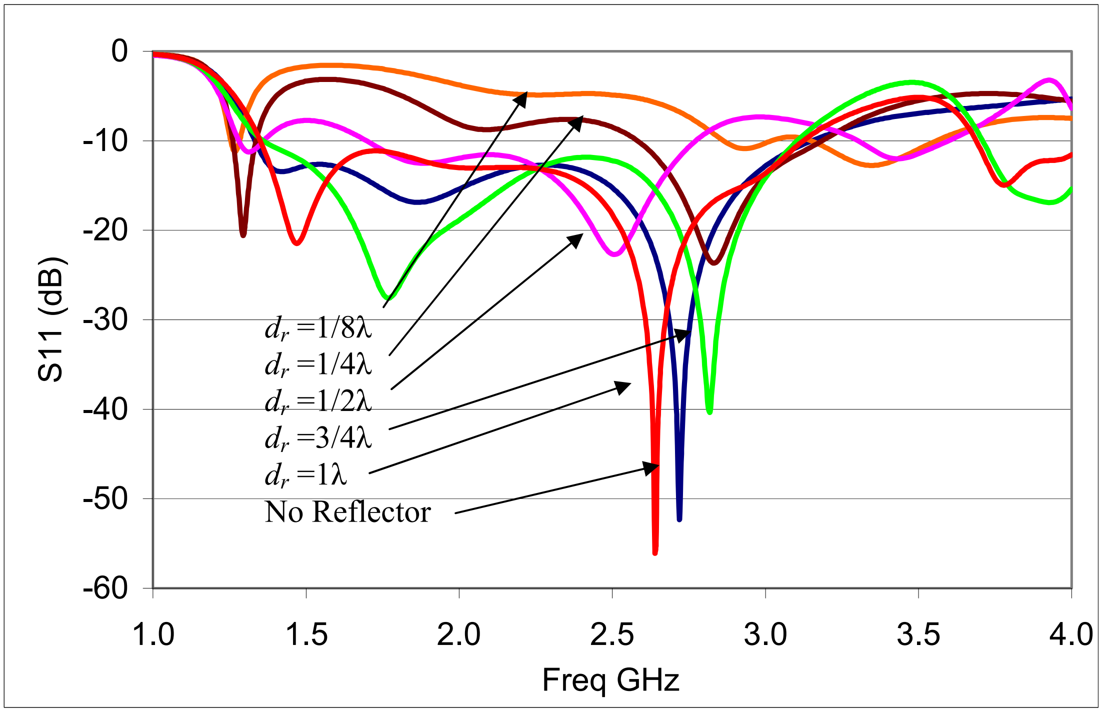

Figure 2.21: Reflector Spacing Effect on the Wide Slot Antenna RL.

The results presented in Figure 2.21 show that the optimum reflector plate spacing needed to maintain the same return loss as that of the slot antenna without a reflector plate lies between ¾λ and 1λ. On the other hand, the radiation pattern of the antenna achieves the optimal front-to-back ratio of 10dB and minimum side lobes at a reflector spacing of approximately ¼λ as illustrated in Figure 2.22.

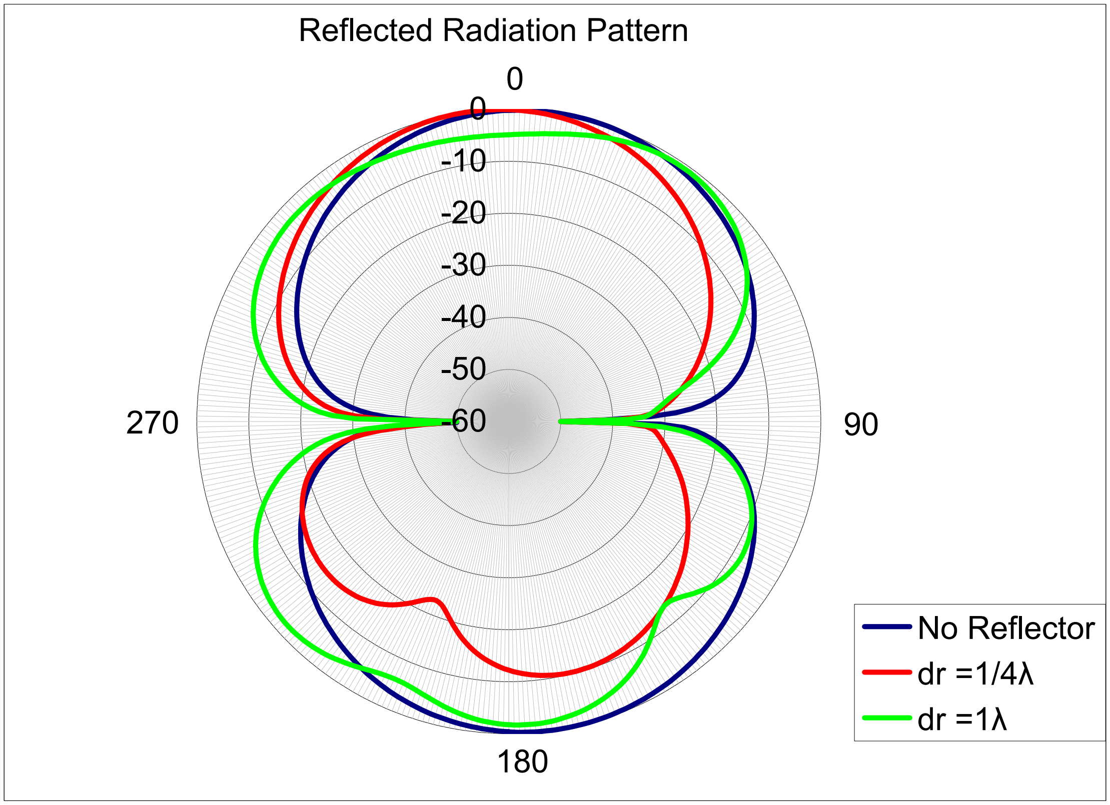

Figure 2.22: Simulated Radiation Pattern as a Function of Reflector Spacing.

The amount of energy that is reflected is directly proportional to the size of the reflector. Figure 2.23 shows a performance comparison between a slot antenna with a finite and one with an infinite reflector plate placed at ¼λ away from the antenna. As expected, the 3D radiation plot of the antenna with the infinite ground plane eliminates the back lobe associated with the antenna that has a finite reflector plate and concentrates all the energy toward the top of the antenna. A trade-off must be made between the reflector size and front-to-back lobe ratio. Once the reflector plate design is completed, the antenna dimensions must be optimized in order to obtain the desired bandwidth and return loss.

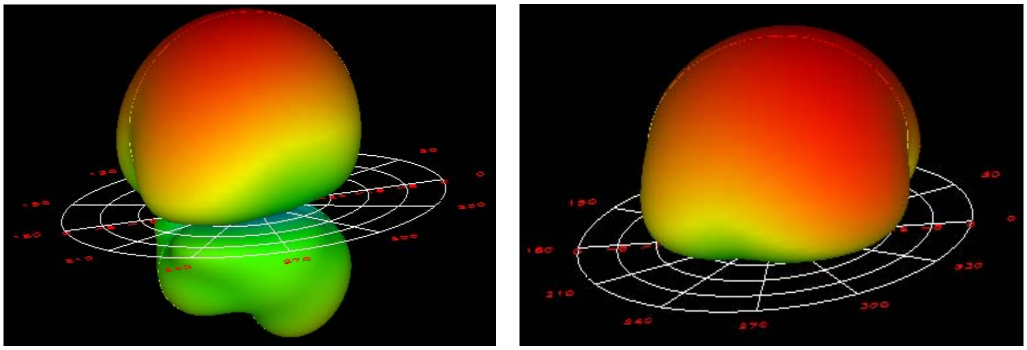

(a) (b)

Figure 2.23: 3D Radiated Field. (a) Slot Antenna with a Finite Reflector Plate, and (b) Slot Antenna with Infinite Reflector Plate.

Table 2.3 presents simulated antenna characteristics of the slot antenna with different reflector plate sizes placed at a ¼λ.

Table 2.3: Comparison Between the Simulated Antenna Parameters with no Reflector, Finite Reflector, and Infinite Reflector Placed at $d_r = ¼\lambda$.

Antenna Parameter	No Reflector	Finite d_r =1/4λ	Infinite dr =1/4λ
Power Radiated (mW)	2.33	1.95	3
Directivity (dB)	5.29	8.6	8.07
Gain (dB)	5.15	8.2	8.05
Efficiency (%)	96.8	91.2	99
Back lobe Attenuation (dB)	0	10	∞

From Table 2.3, efficiencies of 91.2% or greater can be achieved in the three cases with the assumption that the ground plane is a perfect conductor. In addition, it is observed that the back lobe attenuation mainly depends on the reflector plate size and spacing. Also, it can be noted that the gain and directivity of the antenna almost double with the addition of a reflector plate.

2.7 Result and Comparison

2.7.1 2.5GHz Narrow Slot Antenna

The optimized CPW-fed narrow slot antenna was fabricated on a FR-4 board using the LPKF ProtoMat 91s milling tool and measured with the HP-8753D Vector Network Analyzer (VNA). Conventional SOLT calibration standards were utilized to remove the systematic errors from the measured return loss (RL). For calibration results and standard definitions refer to Appendix C. Figure 2.24 illustrates a photograph of the fabricated antenna, and Figure 2.25 shows a comparison between the measured and simulated RL. The frequency shift between the simulated and measured data is due to variation of dielectric constant ε_r across the FR-4 substrate and the fact that the SMA connector parasitics were not taken into account in the simulation.

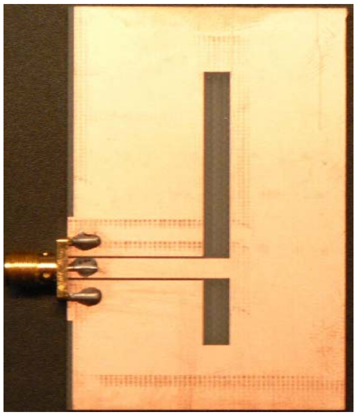

Figure 2.24: Photograph of the Narrow Slot Antenna Fabricated on a FR-4 Board.

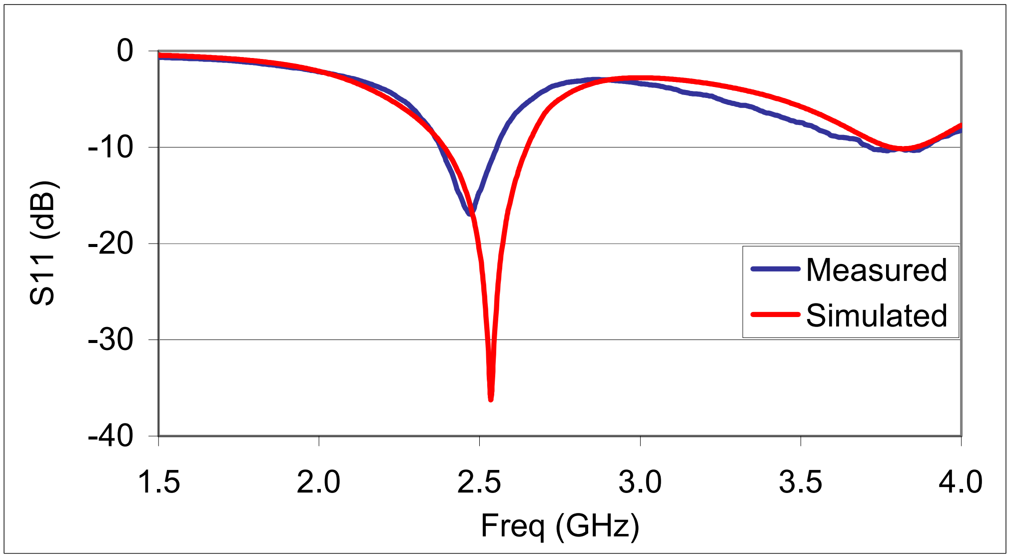

Figure 2.25: Narrow Slot Antenna Measured vs. Simulated Data.

Copper tape was utilized to physically tune the antenna and compensate for fabrication errors, ε_r tolerance within the substrate, and the SMA connector. The re-tuned antenna measurements are illustrated in Figure 2.26 and show a great deal of correlation to the simulated data. The measured and simulated RL were found to be 36.5 and 33dBm at 2.51GHz and 2.48GHz respectively with an impedance bandwidth of 10% measured at a VSWR ≤ 2. The gain of the antenna was measured to be 4.5dB, which compares to the simulated gain of 4.65dB. The measured and simulated phase of the tuned narrow slot antenna is presented in Figure 2.27.

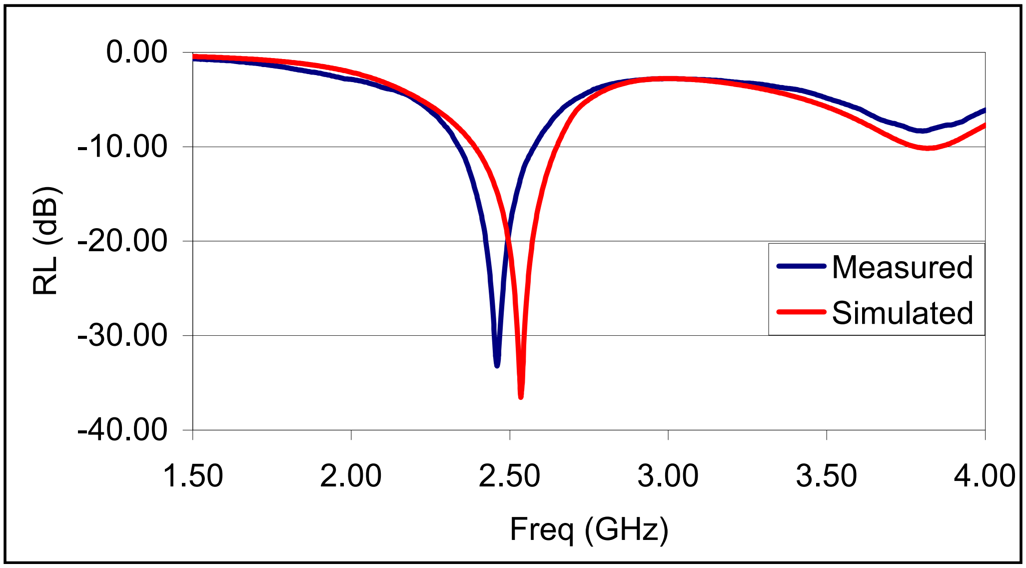

Figure 2.26: Measure vs. Simulated RL of the Tuned Narrow Slot Antenna.

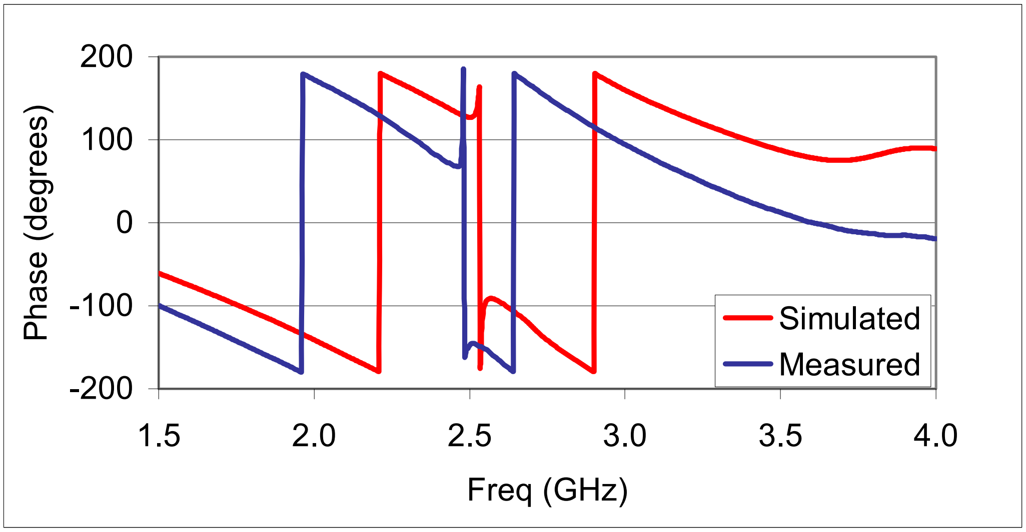

Figure 2.27: Measured vs. Simulated Phase of the Narrow Slot Antenna.

2.7.2 Radiation Pattern Measurements

The coordinate system for the narrow slot antenna radiation pattern measurements is illustrated in Figure 2.28. The feed of the antenna is oriented in the x-direction at Φ=0 degrees, and linearly polarized in the x-direction. To measure the radiated fields in the electric plane **E,** the antenna is fixed at θ=0 degrees and rotated about the z-axis in the Φ direction from 0 degrees to 360 degrees. On the other hand, the magnetic field **H** is obtained by fixing the antenna at Φ=0 degrees and rotated about the x-axis in the θ direction from 0 degrees to 360 degrees.

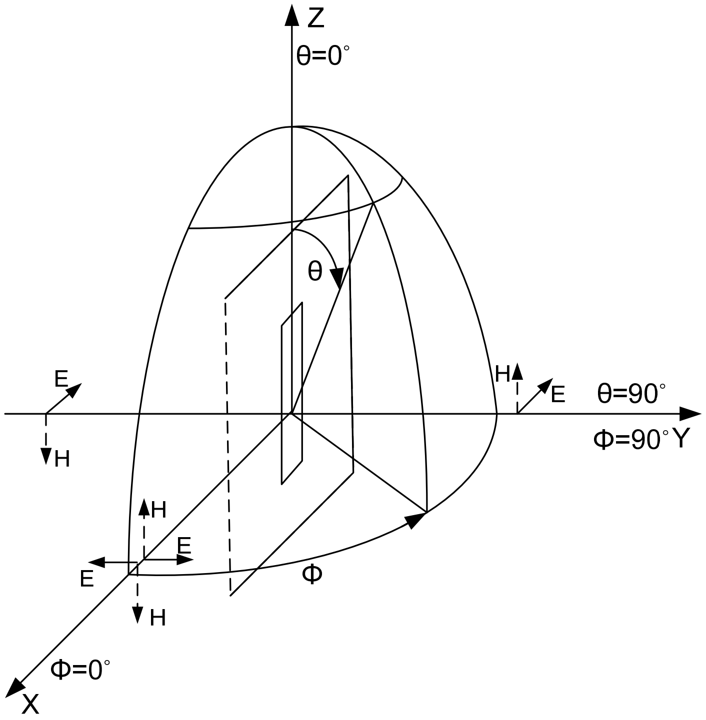

Figure 2.28: Radiation Pattern of a Vertical Slot and Coordinate System.

The radiation pattern of the antenna was obtained with the aid of the anechoic chamber, the HP-8753D VNA, and DAMs' computer tool. Figure 2.29 illustrates a visual of the setup utilized to measure the radiation pattern of the slot antenna as well as a comparison that shows good agreement between the simulated and measured data. The measured narrow slot antenna's coordinates utilized in Figure 2.29a are identical to those of Figure 2.28.

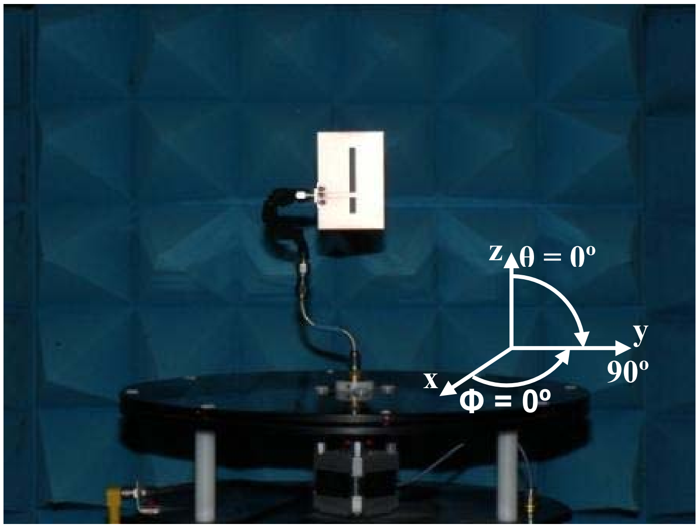

(a)

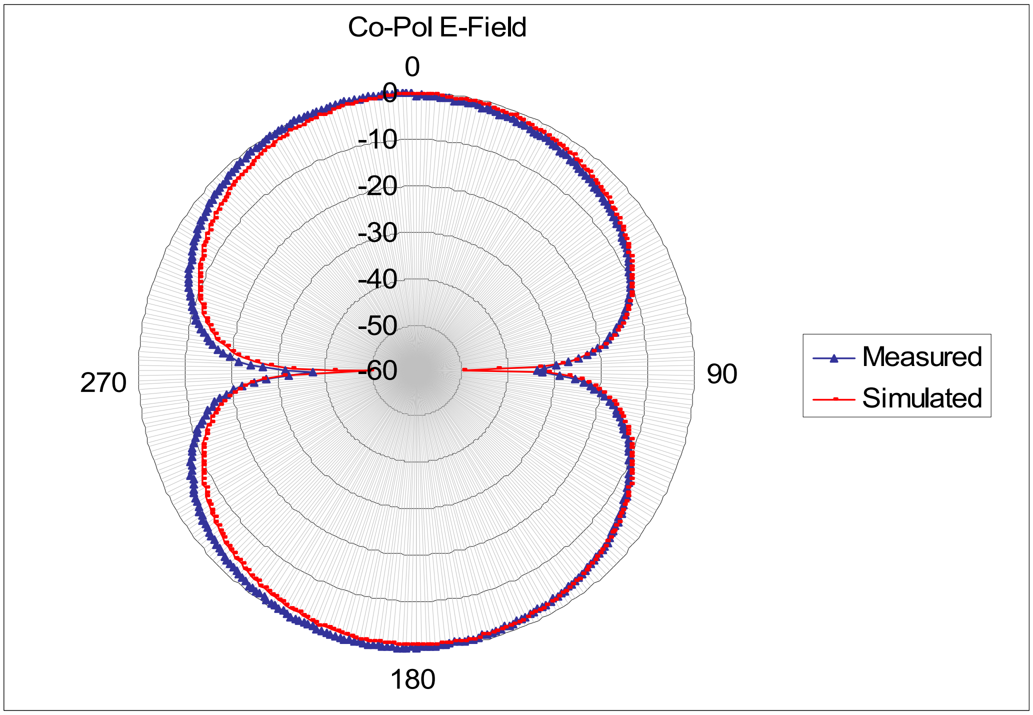

(b)

Figure 2.29: (a) Photograph of the Narrow Slot Antenna E-plane Measurement Setup. (b) Measured vs. Simulated Co-polarized E-plane for the Narrow Slot Antenna.

On the other hand, the coordinate system for the magnetic plane measurements deviates from the coordinate system described in Figure 2.28. As illustrated in Figure

2.30a, the antenna is fixed at θ=90 degrees and rotated about the z-axis in the Φ direction from 0 degrees to 360 degrees. The measured and simulated results of the co-polarized magnetic planes are presented in Figure 2.30b. Furthermore, the cross-polarized electric and magnetic planes are depicted in Figure 2.31 and Figure 2.32.

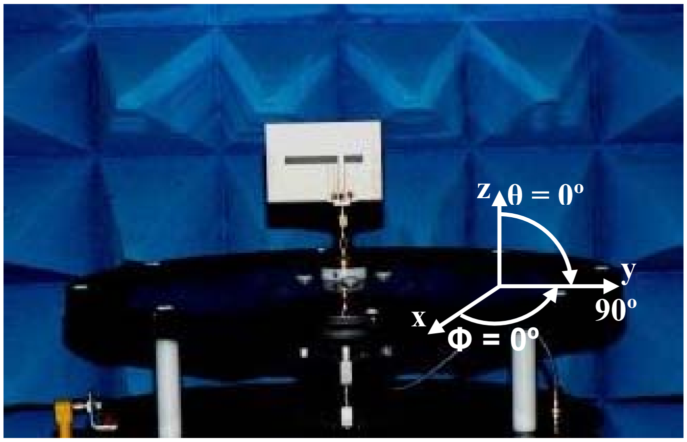

(a)

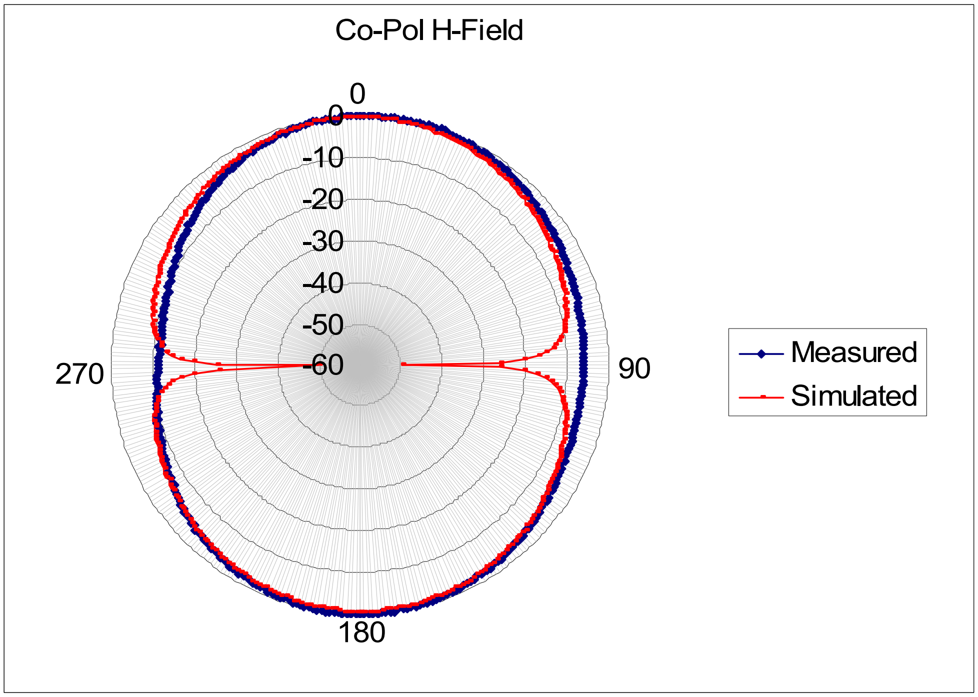

(b)

Figure 2.30: (a) Photograph of the Narrow Slot Antenna H-plane Measurement Setup. (b) Measured vs. Simulated Co-polarized H-plane for the Narrow Slot Antenna.

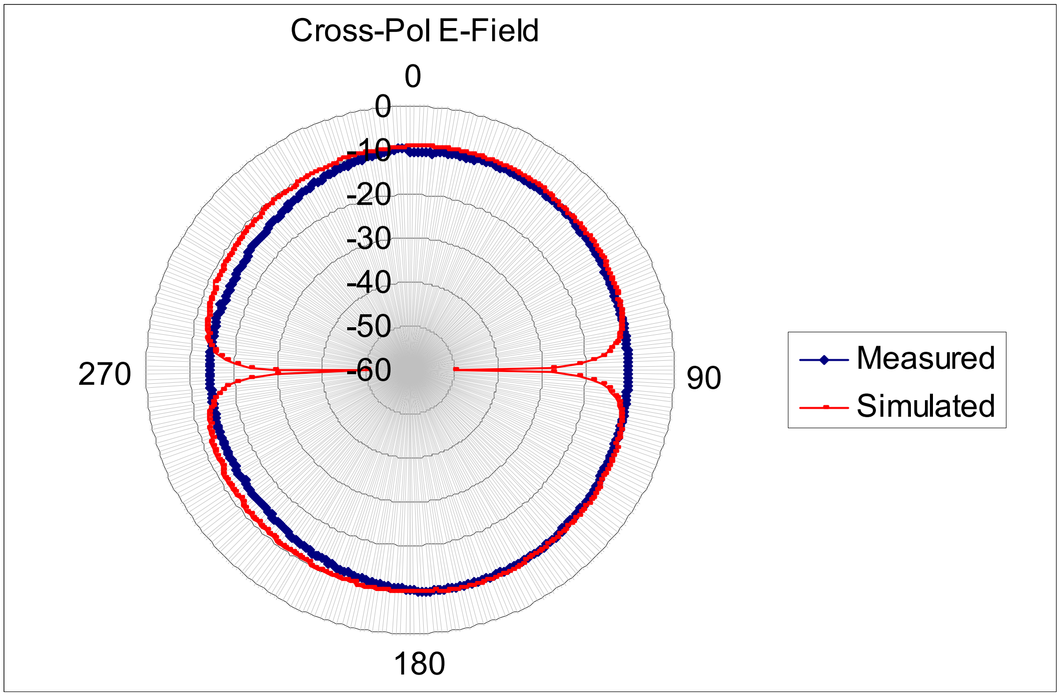

Figure 2.31: Measured vs. Simulated Cross-polarized E-plane.

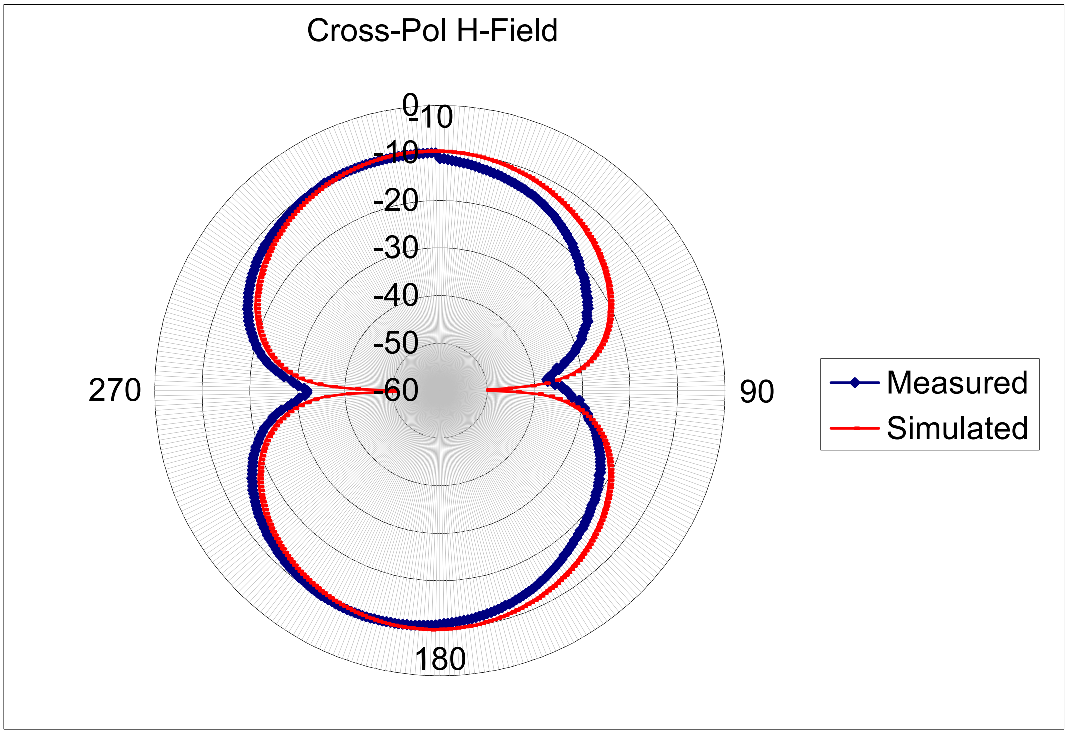

Figure 2.32: Measured vs. Simulated Cross-polarized H-plane

2.7.3 2.5GHz Wide Slot Antenna with U-shaped Tuning Stubs Results

The optimized wide slot antenna was also fabricated on an FR-4 board, and measured using the HP-8753D VNA along with the same SOLT calibration standards used to measure the narrow slot antenna. A comparison between the simulated and measured RL is shown in Figure 2.33. The results illustrate that wide slot antennas are less sensitive to fabrication and dielectric constant variations within the FR-4 substrate. The discrepancy between the simulated and measured data is mainly due to the CPW-to-SMA connector transition and connector losses, which were not taken into account during the calibration process. The measured and simulated return loss was found to be 28dB and 42dB, respectively, at an operational frequency of 2.5GHz. The measured gain of the antenna was found to be 5.4dBi, which compares well to the simulated gain of 5.1dBi.

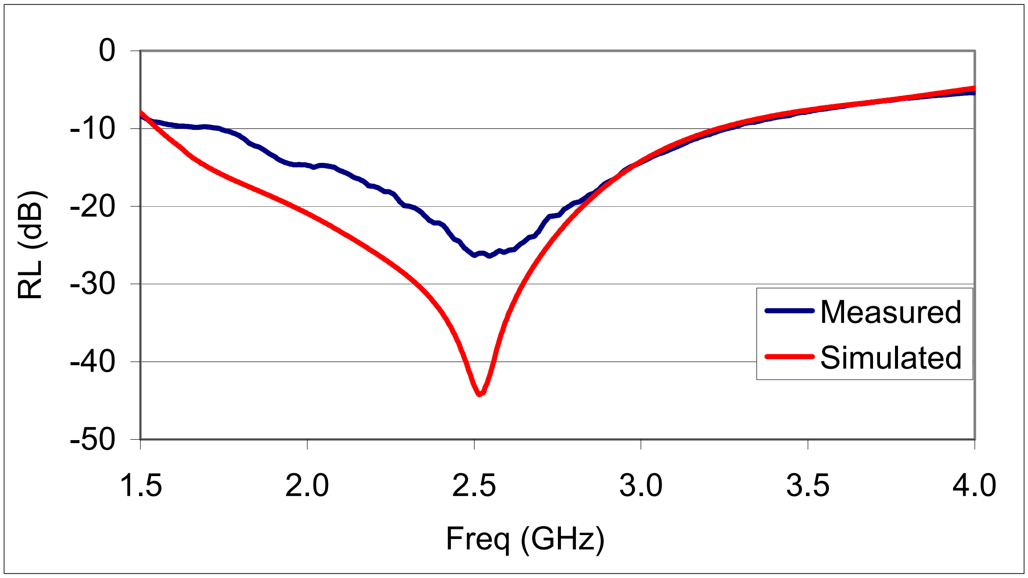

Figure 2.33: Measured vs. Simulated Return Loss of the 2.5GHz Wide Slot Antenna with U-shaped Tuning Stubs.

A comparison between the simulated and measured impedance of the wide slot antenna is shown in Figure 2.34. Figure 2.34b reveals that the antenna possesses multiple resonances and is well matched at the design frequency of 2.5GHz.

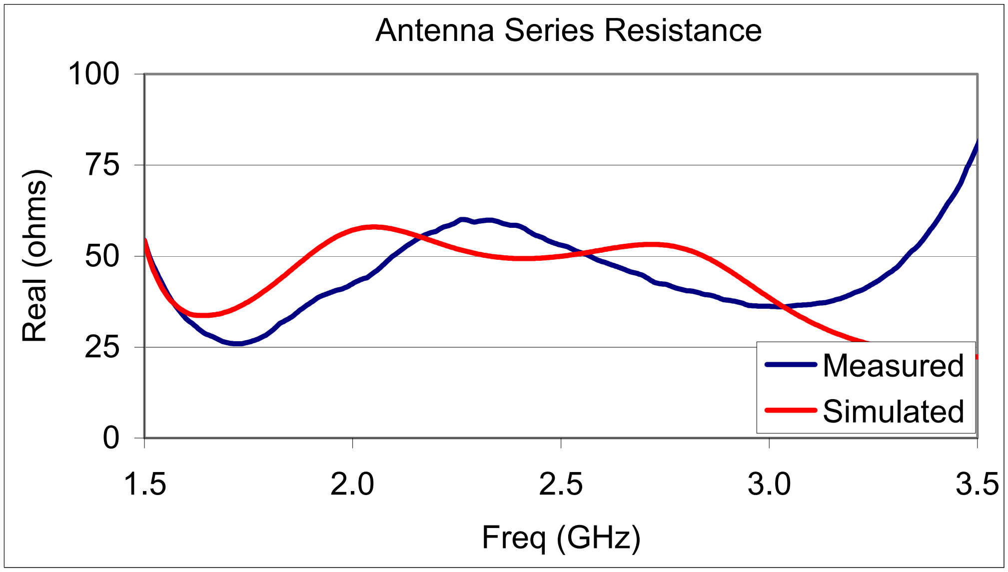

(a)

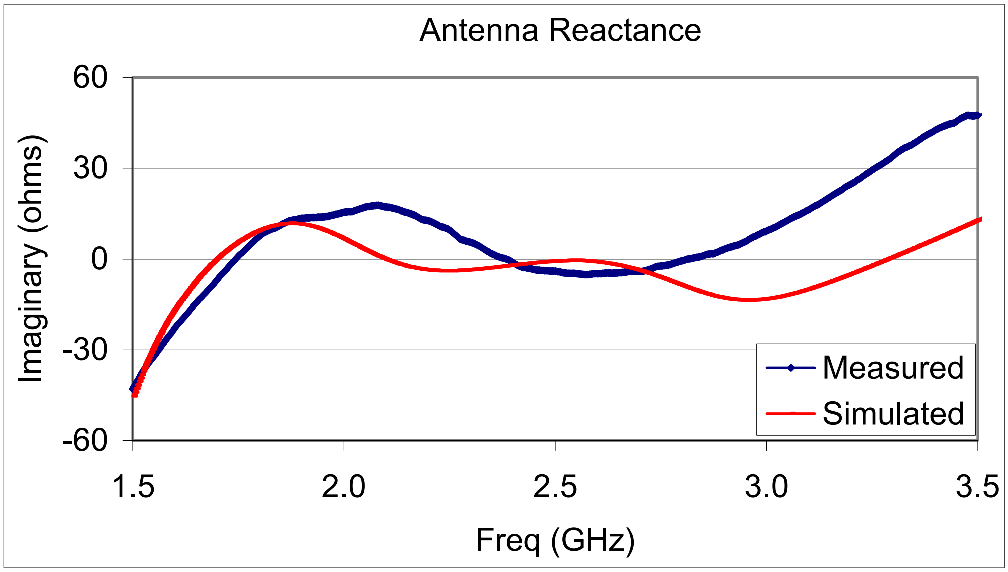

(b)

Figure 2.34: Measured vs. Simulated Wide Slot Antenna Impedance. (a) Real and (b) Imaginary.

As illustrated in Figure 2.35 a bandwidth of approximately 69% was obtained referenced to a VSWR≤2, which agrees with the simulated bandwidth of 70%.

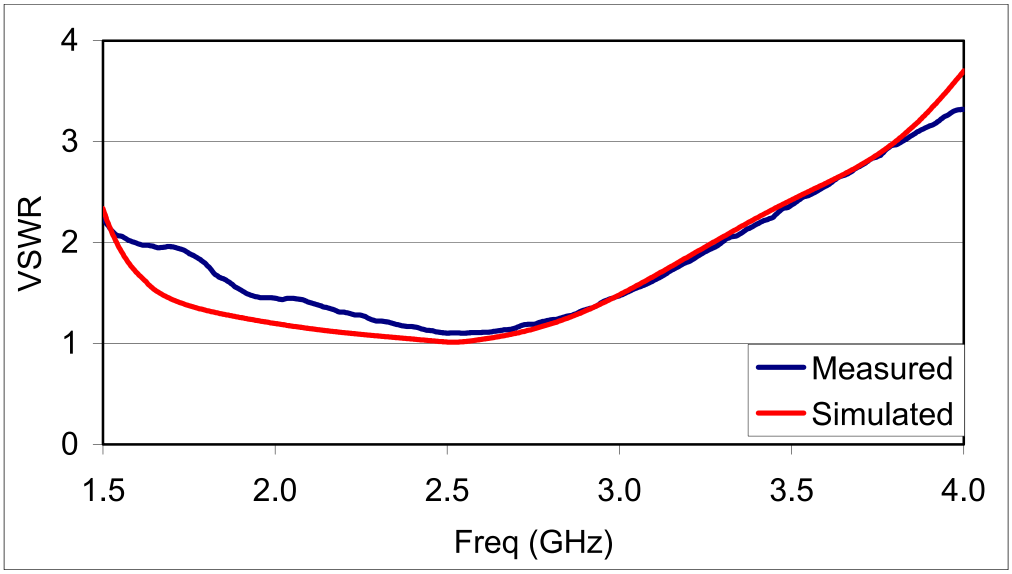

Figure 2.35: Measured vs. Simulated VSWR.

The coordinate system presented in Figure 2.28 remains valid for the wide slot antenna radiation pattern measurements presented in Figure 2.36. In addition, the wide slot antenna was measured under the same conditions previously mentioned in the narrow slot antenna measurements. The antenna setup for the co-polarized electric field is illustrated in Figure 2.36a, and the measurement results are depicted in Figure 2.36b. The complementary magnetic plane of the wide slot antenna and a visual of the setup are also presented below. The result shows a high degree of correlation between the simulated and measured radiation patterns.

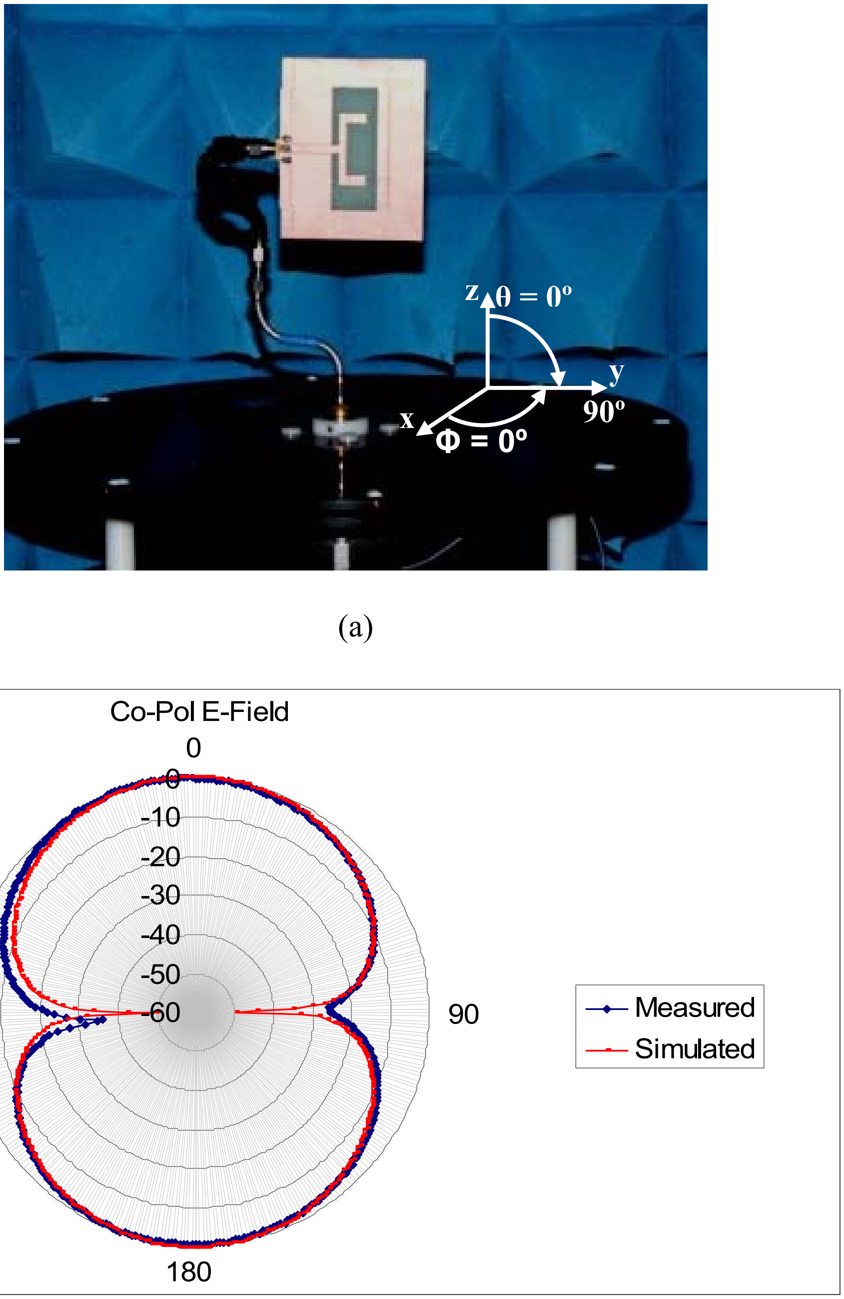

(a)

(b)

Figure 2.36: (a) Photograph of the Wide Slot Antenna E-plane Measurement Setup. (b) Measured vs. Simulated Co-polarized E-plane for the Narrow Slot Antenna.

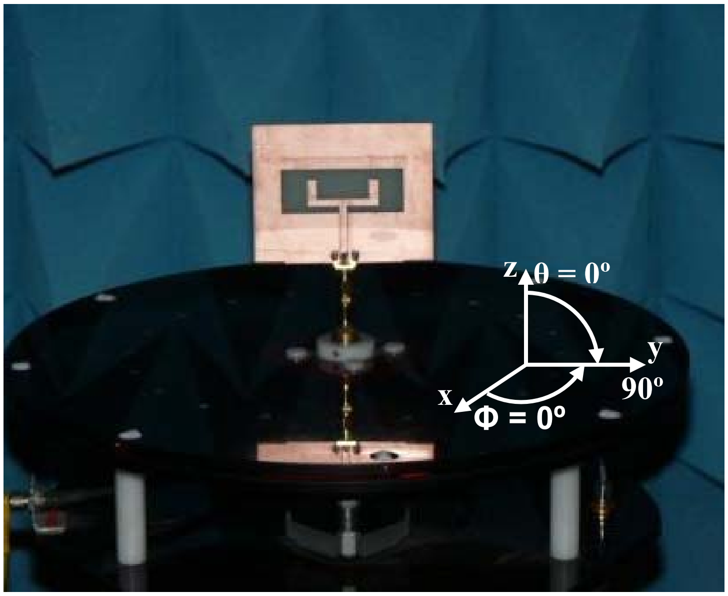

(a)

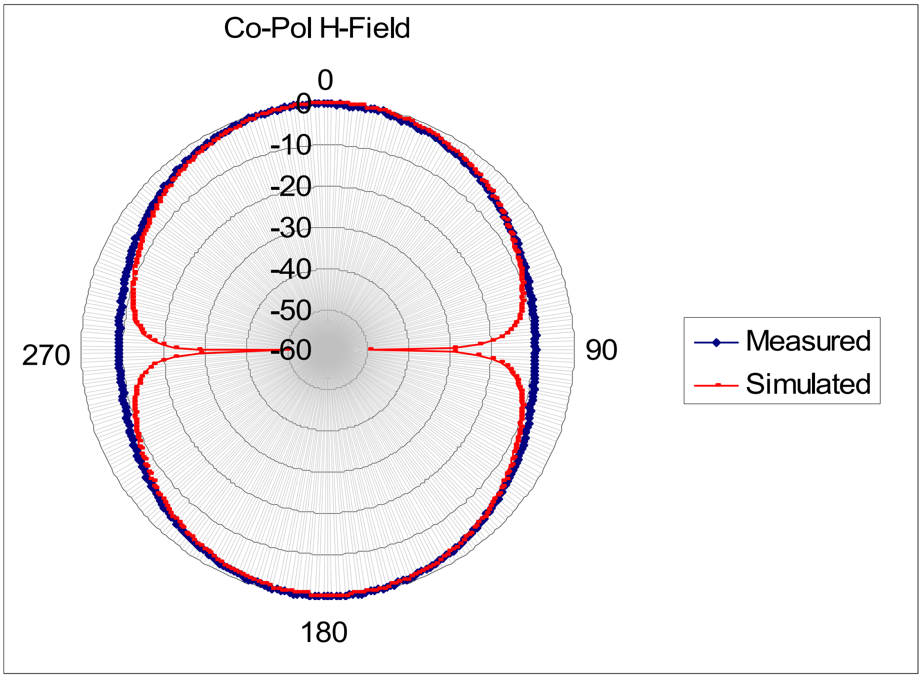

(b)

Figure 2.37: (a) Photograph of the Wide Slot Antenna H-plane Measurement Setup. (b) Measured vs. Simulated Co-polarized H-plane for the Narrow Slot Antenna.

2.8 Chapter Summary and Conclusions

In this chapter an in-depth analysis of slot antennas and their characteristics were presented. In the process, a parametric study of the series resistance of the narrow slot antenna as a function of the feed point d_S was provided. In addition, the effects of a reflector plate on the impedance and radiation pattern of the wide slot antenna was studied. The two low frequency antenna prototypes consisting of an offset-CPW-fed slot and a center-CPW-fed wide slot antenna with U-shaped tuning stubs were developed and presented a high degree of correlation with the simulated data.

The wide slot antenna presented many advantages over the narrow slot antenna. For instance, the wide slot antenna is less sensitive to discrepancy in dielectric constant of the substrate and the fabrication tolerances. Also, the wide slot antenna provides a much wider bandwidth than the narrow slot antenna presented in Section 2.3. Furthermore, the added tuning capability eases the design and optimization of the antenna, and can be easily altered to obtain a wider range of operation. Finally, since the ground plane of the antenna is symmetric, wire bonding is not required to reduce the higher order modes otherwise found in the offset-fed narrow slot antenna.

Chapter 3

2.5GHz Detector Circuit Design – Integration of Rectenna Element

3.1 Introduction

The second part of the Rectenna element consists of a detector circuit. These devices are used in many applications such as: power monitoring, automatic gain control circuits, automatic braking circuits, and signal strength indicators. In addition to these applications, diodes can be utilized as envelope detectors, doublers, mixers, and square-law detectors depending on the power levels at which the diode is operated and the treatment of higher order harmonics.

This thesis work mainly concentrates on square-law detectors and their characteristics. This chapter presents a brief background theory of square-law detectors as well as the design and optimization of detector circuits with the aid of Agilent's Advanced Design Systems (*ADS*) CAD software. Also, a theoretical overview of CPW-to-Microstrip transitions will be presented along with the development of a via-less CPW-to-Microstrip transition used in this thesis. The implementation of the transition is necessary in order to integrate the CPW-fed slot antenna with the microstrip detector circuit. Finally, a comparison is made between the two components of the Rectenna element realized in a single FR-4 board and individual Rectenna elements connected by a Male-to-Male (M-M) connector.

3.1.1 Background Theory

Detectors are essential components in wireless communication and sensory systems. The two main types of diode detectors are envelope and square-law detectors. Envelope detectors are largely used in RF circuits to demodulate an amplitude-modulated signal by providing an output voltage that is directly proportional to the envelope of the incoming signal. Square-law detectors, on the other hand, are basically a power measuring device, which provides a DC output voltage that is directly proportional to the input RF power or the square of the input voltage as its name implies [19].

Rectification is accomplished by using nonlinear devices such as Schottky diodes. Equation 3.1 describes the small-signal voltage to current relationship of a commercially available Schottky diode [20].

$$I(V) = I_S (e^{(\alpha V - IRs)} - 1) \tag{3.1}$$

where $\alpha = q / nkT$, q is the charge of an electron, k is Boltzmann's constant, T is the temperature, n is the ideality factor, and I_s is the saturation current. Figure 3.1 illustrates the I-V characteristics of the commercially available HSMS-285X Schottky diode family series. Typical values for the diode's series resistance R_s are found in the SPICE parameter table of the device data sheet [20].

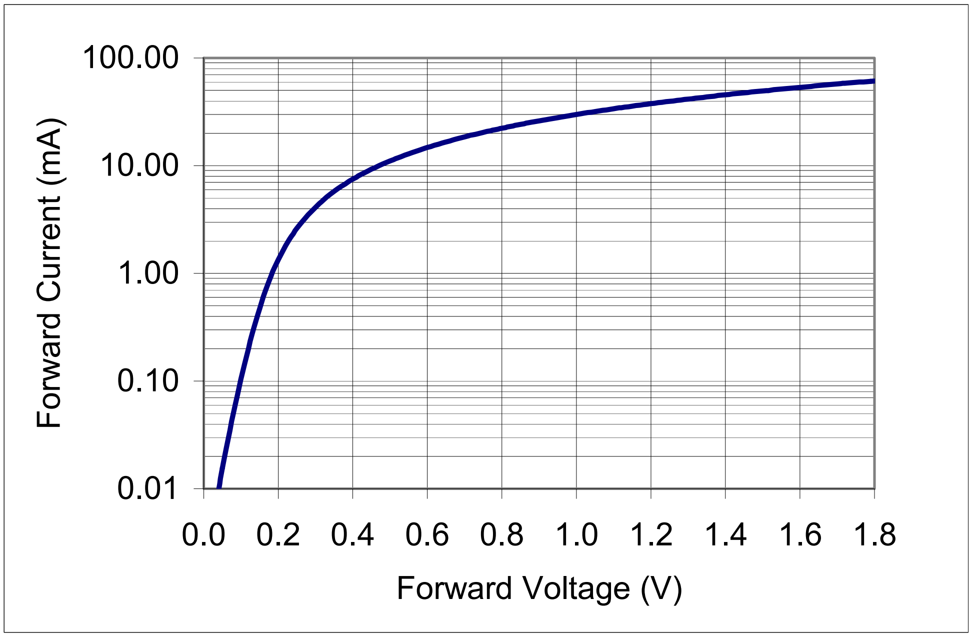

Figure 3.1: Typical Forward Current vs. Forward Voltage in Logarithmic Scale Representation.

In a sense, all detectors present square-law characteristics at low power levels. So, if the applied voltage also contains a small RF signal represented by equation 3.2

$$V = V_0 + v_0 \cos(w_0 t) \tag{3.2}$$

where V_0 is the applied bias voltage and v_0 is the magnitude of the RF signal. The diode's current can be expressed as a Taylor's series expansion which provides the first three harmonics generated by the rectification process [21].

$$I = I_0 + v_0 G_d \cos(w_0 t) + \frac{v_0^2}{2} G_d^{'} \cos^2(w_0 t)$$

$$I = I_0 + \frac{v_0^2}{4} G_d^{'} + v_0 G_d \cos(w_0 t) + \frac{v_0^2}{4} G_d^{'} \cos(2 w_0 t) \tag{3.3}$$

The above Taylor's series expansion only remains valid for sufficiently low power levels ($P_{in} \leq -20$dBm). If the input power is too large, small-signal behavior will not apply and the output will become saturated. The dynamic range of the device is dictated by the noise floor at the lower end (P_{in} < -55dBm) and by distortions at the upper end. The higher order harmonics generated by the diode can be easily suppressed by implementing a simple low pass filter as illustrated in Figure 3.2.

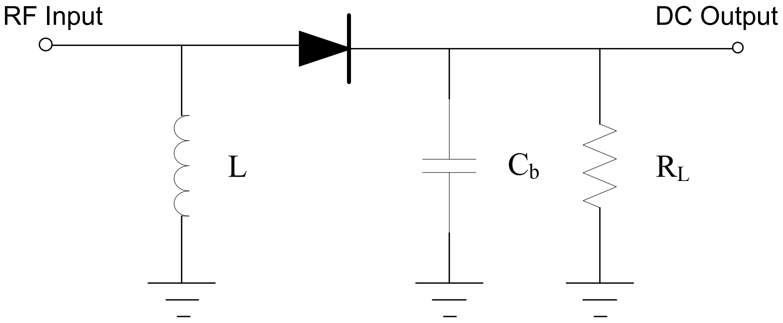

Figure 3.2: Conventional RF Detector Circuit Schematic.

The input inductor serves as a DC return path for the diode, while the output bypass capacitor acts as an RF short that separates the RF components from the output DC voltage, which keeps most of the power across the diode terminals. Finally, the output load resistance increases the overall output voltage of the detector. All of the components described above play a significant role on the output voltage and the sensitivity of the device. Sensitivity is a figure of merit that describes the quality of the detector, and it is representative of how much output voltage is obtained for a given input RF power.

According to Agilent Technologies [22], the junction capacitance C_j, load resistance, and mismatch losses also dictate the sensitivity of the detector. Equations 3.4 - 3.7 describe the sensitivity of the detector from an ideal case to a more realistic scenario.

$$\gamma = \frac{0.52}{I_S}\left(\frac{V}{W}\right) \tag{3.4}$$

$$\gamma_1 = \frac{0.52}{I_S(1+\omega^2 C_j^2 R_S R_j)}\left(\frac{mV}{\mu W}\right) \tag{3.5}$$

$$\gamma_2 = \frac{0.52}{I_S(1+\omega^2 C_j^2 R_S R_j)\left(1+\frac{R_j}{R_L}\right)}\left(\frac{mV}{\mu W}\right) \tag{3.6}$$

$$\gamma_3 = \gamma_2(1-\Gamma^2)\left(\frac{mV}{\mu W}\right) \tag{3.7}$$

Equation 3.4 is only valid for an ideal diode with a zero bias current where the parasitic effects, reflections, and load resistor are neglected. A more reasonable approximation is presented by equation 3.5 where one can observe that some portion of the RF signal is bypassed by the junction capacitance C_j which decreases the overall sensitivity of the device. Finally, the mismatch loss, which plays a major role in the sensitivity of the device, is given by equation 3.7. In Section 3.2 of this chapter a comparison between the simulated detector circuits with and without a matching network are presented, which demonstrates the significance of the mismatch loss. The detector circuit for the proposed Rectenna element is similar to the detector circuit presented in Figure 3.2. The difference lies in that for the Rectenna element, the detector circuit requires some sort of filtering mechanism to prevent higher order harmonics from re-radiating through the antenna.

3.2 Detector Circuit Design

In this section the development of a detector circuit that uses the HP8250 zero-bias Schottky diode is presented. This process is done with the aid of *ADS*. As discussed in Chapter 1, the detector circuit for the Rectenna element presented by Nahas [3] consists of a matching network, a step impedance low pass filter, a fast rectifier, and an output DC filter. The input filter is usually designed to operate at a slightly higher cut-off frequency in order to achieve the lowest possible attenuation at the design frequency. Distributed elements are used in this design to reduce the packaging parasitics found in lumped components. This is necessary since packaging parasitics are much more significant at millimeter wave and infrared frequencies.

For the low frequency Rectenna prototype, a distributed low pass filter was designed to work at a cut-off frequency of 3.2GHz and provide at least a 20dB of insertion loss (IL) at the second harmonic of 5GHz. In order to obtain the desired attenuation, a five element distributed filter was realized. The normalized element values for a maximally flat low pass filter obtained using the table presented by Pozar [21] are shown below.

$g_1 = 0.618 = L_1$
$g_2 = 1.618 = C_2$
$g_3 = 2.000 = L_3$
$g_4 = 1.618 = C_4$
$g_5 = 0.618 = L_5$

The electrical length (βl_i) of each section was obtained using the following equations

$$\beta\ell = \frac{LR_0}{Z_H} \tag{3.8}$$

$$\beta\ell = \frac{CZ_L}{R_0} \tag{3.9}$$

where L and C are the normalized element values of inductance and capacitance, respectively and R_0 is the reference impedance. Z_H and Z_L represent the sections of very high and very low characteristic impedance of the line. According to Pozar [21], the Z_H/Z_L ratio should be as high as possible; therefore, the actual values of Z_H and Z_L are usually chosen to be the highest and lowest characteristic impedance that can be fabricated. These types of filters are widely known as step impedance filters due to the dramatic changes in characteristic impedance from one section to the other. After obtaining the electrical length βl_i shown in Table 3.1, the *ADS LineCalc* computer tool was utilized to determine the physical dimensions of the filter, which are also tabulated in Table 3.1.

Table 3.1: Step Impedance Filter Dimensions.

Section	$Z_i = Z_L$ or Z_H	βl_i	W_i (mm)	l_i (mm)
1	120 Ω	14.75°	0.368	2.92
2	20 Ω	37.08°	11.05	6.38
3	120 Ω	47.75°	0.368	9.42
4	20 Ω	37.08°	11.05	6.38
5	120 Ω	14.75°	0.368	2.92

Figure 3.3 shows the layout of the step impedance filter as drawn in Agilent's Momentum, in which the thin and wide sections of transmission line are more inductive and capacitive, respectively.

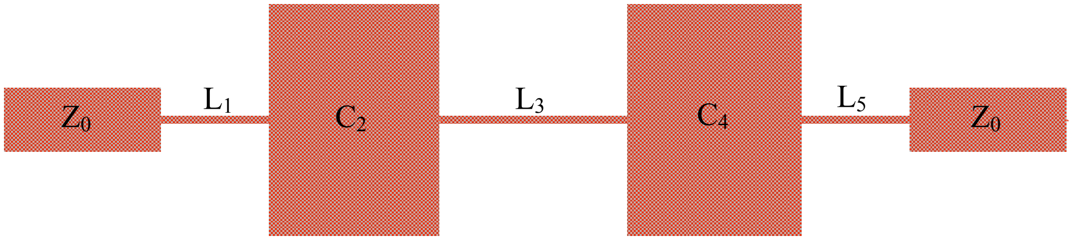

Figure 3.3: Step Impedance Low Pass Filter Momentum Layout.

The simulated results depicted in Figure 3.4 show that the filter has a 3dB cut-off frequency of approximately 3.2GHz and presents an insertion loss (IL) of 0.5dB at the Rectenna element design frequency of 2.5GHz.

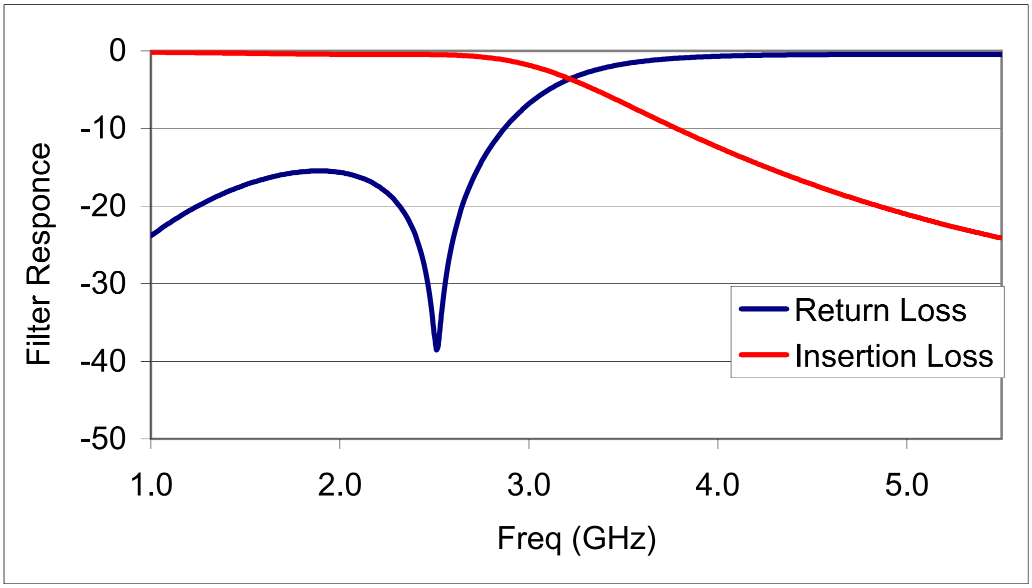

Figure 3.4: Step Impedance Low Pass Filter Response.

One drawback of the filter presented above is that it requires many sections to achieve the desired attenuation, which in turn increases the size of the Rectenna element dramatically. In addition, the step impedance low pass filter presents more losses than the ¼λ shorted stub used in this design.

To reduce the size and losses of the input low pass filter, a ¼λ shorted stub was implemented in order to prevent the higher order harmonics from re-radiating through the antenna. Figure 3.5 shows the *ADS* simulated response for the ¼λ shorted stub. From this figure, it is observed that the ¼λ stub looks like an open circuit at the design frequency of 2.5GHz while shorting the 5GHz harmonic to ground.

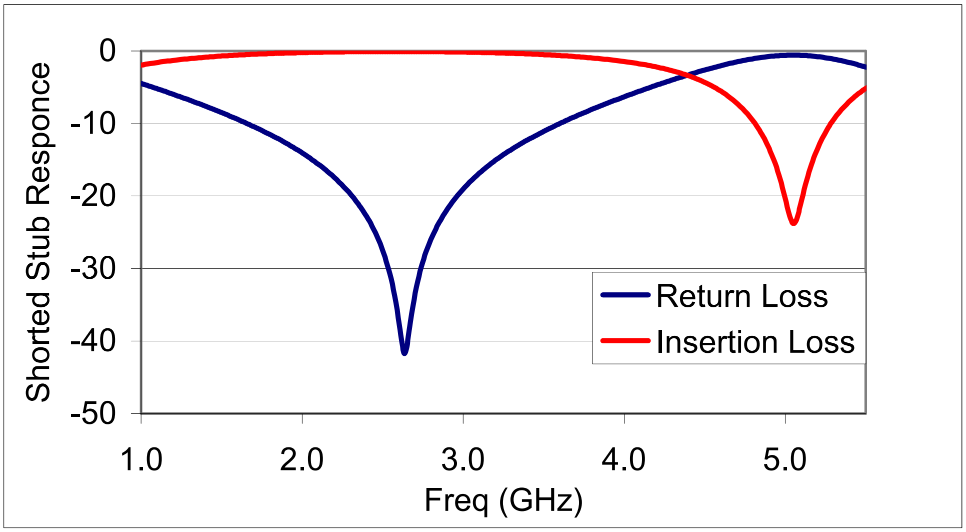

Figure 3.5: ¼λ Shorted Stub IL and RL.

In addition, utilizing the shorted stub only presents a simulated IL of 0.07dB at the design frequency and attenuates the second order harmonic by 25dB. Furthermore, it provides a DC path to ground allowing the device to become self-biased; keeping all the power across the diode's terminals. The harmonic balance simulation presented in Figure 3.6 further illustrates this concept.

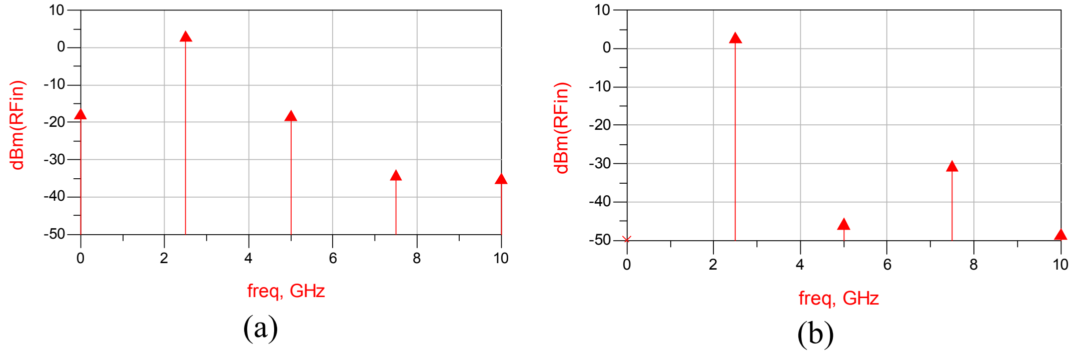

(a) (b)

Figure 3.6: Harmonics Generated by the Rectification Process at the Input of the Detector. (a) Without ¼λ Stub, and (b) with a ¼λ Stub Present.

Figure 3.6b shows that the shorted stub provides a DC path to ground and attenuates the higher order harmonics preventing them from reaching the source; in this case the antenna. The downside to this technique is that ¼λ shorted stub resonates at odd multiples of the resonant frequency, which is illustrated by the 7GHz harmonic in Figure 3.6, which is not attenuated.

The same sort of behavior is observed at the output of the detector where the output DC voltage has to be separated from the high frequency components. Figure 3.7 shows that all the higher harmonics are attenuated effectively providing an isolation of about 40dB at the design frequency. This was accomplished by implementing a shunt open-circuited stub at the output of the detector, which provides the same susceptance as that of the bypass capacitor.

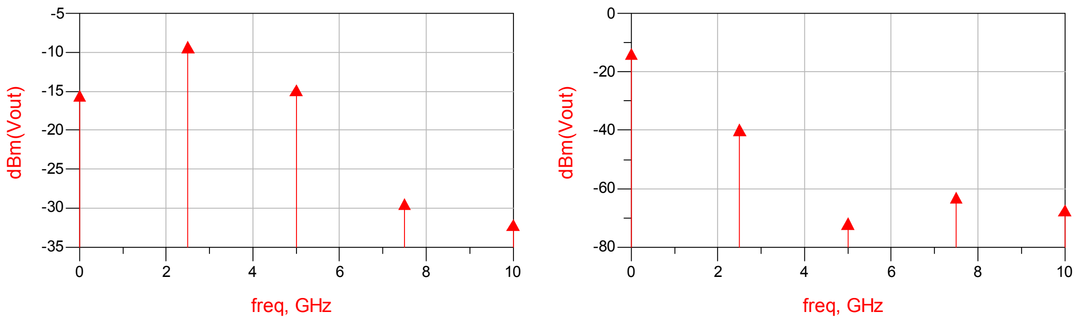

(a) (b)

Figure 3.7: Harmonics Generated by the Rectification Process at the Output of the Detector with ¼λ Stub in Place. (a) Without the Bypass Capacitor and the RF Block Inductor. (b) With the Bypass Capacitor and the RF Block Inductor in Place.

As mentioned before, the matching network between the antenna and the detector circuit plays a big role in the output voltage and sensitivity of the detector. This behavior is illustrated in Figure 3.8, where Γ_S and Γ_{IN} represent the source and input reflection coefficient, respectively, and a_1 and b_1 represent the incident and reflected wave at the assigned reference plane, respectively.

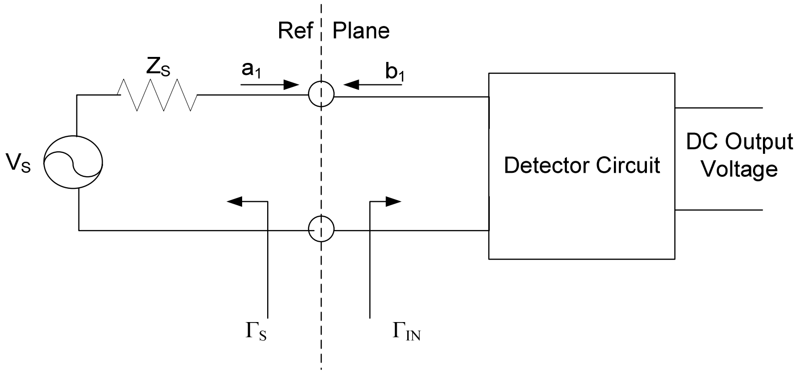

Figure 3.8: Detector Input Port Interface.

The power available from the source can be characterized as the power delivered by the source under a conjugately matched load; in this case, the load is the input impedance of the detector circuit [23]. So, the power available from the source is given by equation 3.10.

$$P_{AVS} = \frac{\frac{1}{2}|b_S|^2}{1-|\Gamma_S|^2} \tag{3.10}$$

The power delivered to the detector is defined as the difference between the incident and the reflected power at the input reference plane, and it is expressed by equation 3.11.

$$P_{IN} = \frac{1}{2}|a_1|^2 - \frac{1}{2}|b_1|^2 = \frac{1}{2}|a_1|^2\left(1-|\Gamma_{IN}|^2\right) \tag{3.11}$$

where,

$$a_1 = \frac{b_S}{1-\Gamma_S\Gamma_{IN}} \tag{3.12}$$

and,

$$P_{IN} = \frac{1}{2}|b_S|^2 \frac{1-|\Gamma_{IN}|^2}{|1-\Gamma_S\Gamma_{IN}|^2} \tag{3.13}$$

where b_S is the reflected wave looking into the source.

According to [23], the power delivered to the detector (P_{IN}) and the power available from the source (P_{AVS}) can be related by the mismatch factor (M_S) at a given reference plane.

$$P_{IN} = P_{AVS} \cdot M_S \tag{3.14}$$

This factor is utilized to quantify the amount of P_{AVS} that is delivered to the input of a given device, and it is expressed by equation 3.15.

$$M_S = \frac{(1-|\Gamma_S|^2)\cdot(1-|\Gamma_{IN}|^2)}{|1-\Gamma_S\Gamma_{IN}|^2} \tag{3.15}$$

so,

$$P_{IN} = P_{AVS}\left(\frac{(1-|\Gamma_S|^2)\cdot(1-|\Gamma_{IN}|^2)}{|1-\Gamma_S\Gamma_{IN}|^2}\right) \tag{3.16}$$

It should be observed that when $\Gamma_{IN} = \Gamma_S^*$, the mismatch factor is equal to unity, thus under this condition $P_{IN} = P_{AVS}$. The analysis presented above is valid for any given reference plane.

This concept is further reinforced by analyzing the output voltage and sensitivity of the device by performing *ADS* simulations for the detector circuit with and without a matching network. The simulated result presented in Figure 3.9 and Figure 3.10 show that the matching network is a key component of the detector circuit, since it dictates the output voltage and sensitivity of the device. It is observed that a decrease in output voltage and thus sensitivity occurs when the source is not conjugately matched to the detector's input impedance since some of the power gets reflected back to the source. This behavior agrees with the literature and equations presented previously.

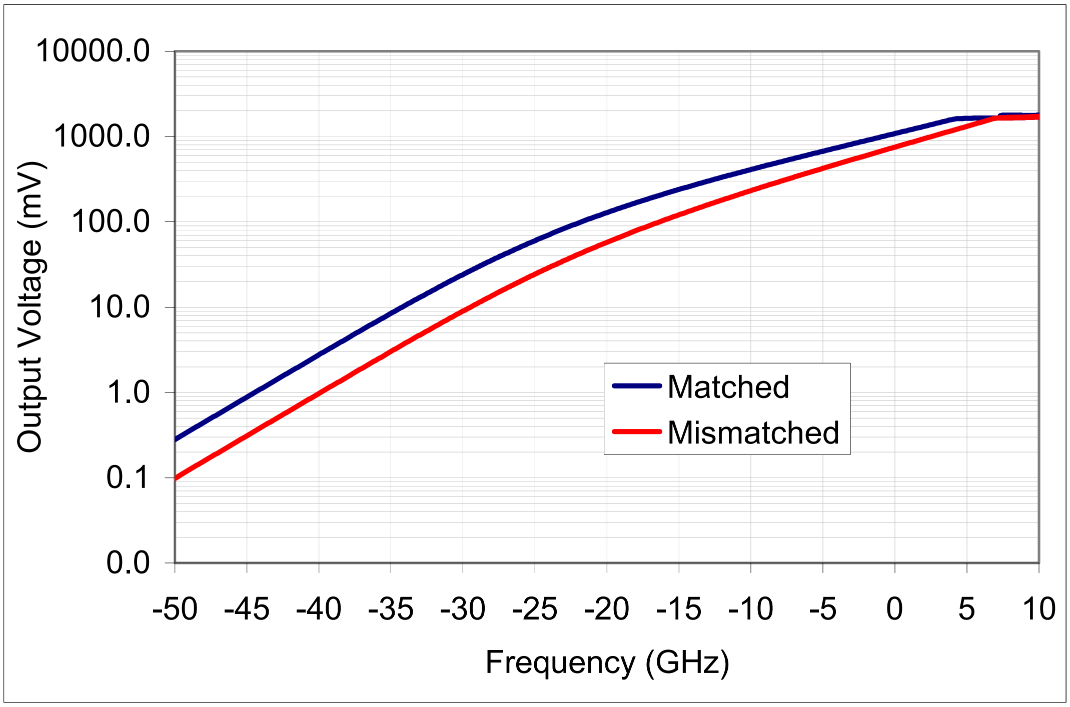

Figure 3.9: Simulated Output Voltage vs. Input Power. Red plot = no Matching Network; Blue Plot = Matching Network in Place.

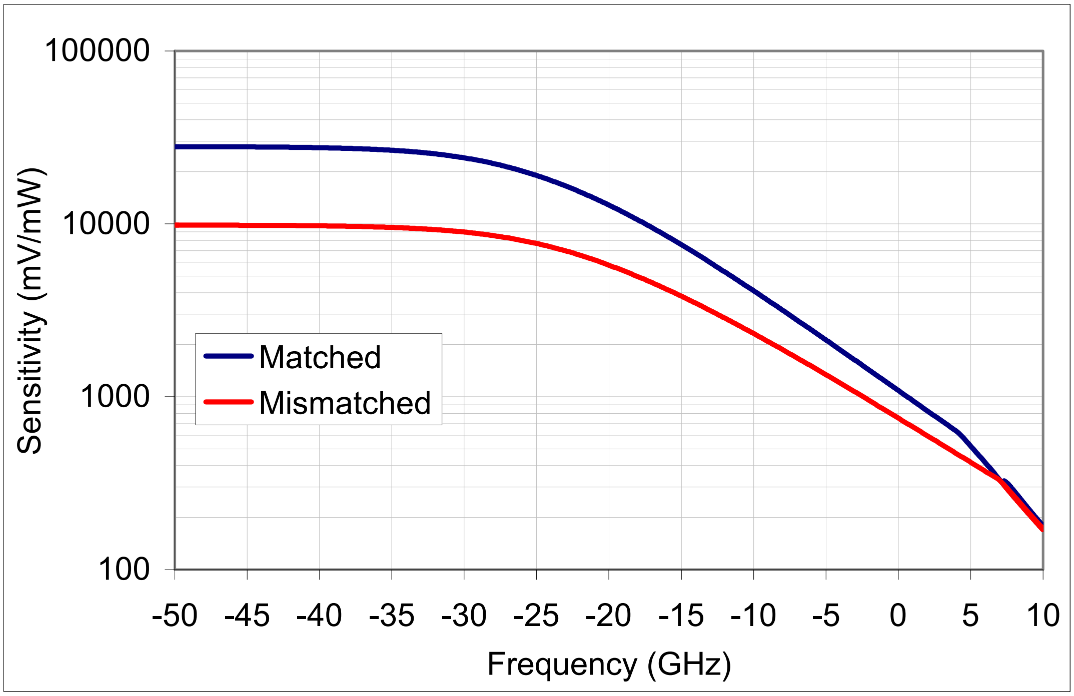

Figure 3.10: Simulated Detector Sensitivity. Red = no Matching Network, Blue Plot = Matching Network in Place.

An optimized detector layout along with the simulated return loss of the detector is illustrated in Figure 3.11. Figure 3.11b shows that the detector is well matched at the design frequency providing maximum power transfer, and therefore, increasing the detector's output voltage and sensitivity.

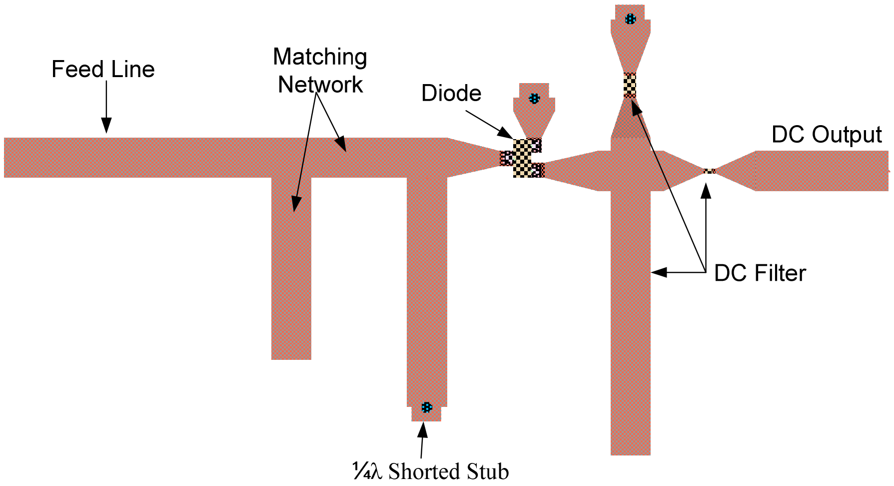

(a)

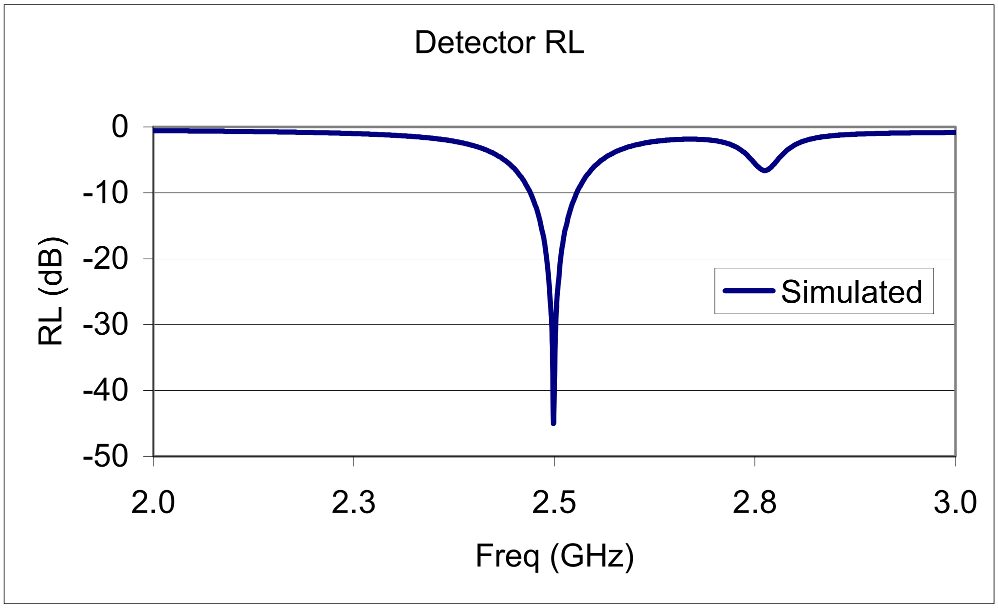

(b)

Figure 3.11: (a) Optimized Detector Circuit Layout. (b) Simulated 2.5GHz Detector Return Loss.

3.3 Rectenna Element Integration

As previously mentioned, a Rectenna element is composed of an antenna section integrated with a detector circuit. In order to assemble the low frequency Rectenna elements prototype within a single FR-4 board, a CPW-to-Microstrip transition is required since the feeding mechanism of the antenna differs from that of the detector circuit. Even though the CPW and microstrip lines operate in a quasi-TEM mode, their electric and magnetic field distribution are not the same. If the transition is not properly designed, some of the incident power at the transition can be reflected, or radiated into free space, which can interfere with the antenna's radiation characteristics. In this section, a brief description of a via-less CPW-to-Microstrip transition is described along with its integration to the CPW-fed wide slot antenna.

3.3.1 Via-less CPW-to-Microstrip Transition

Historically the demand for high density and high performance microwave and millimeter wave circuits has increased dramatically making RF devices more compact and highly integrated. These devices are often fabricated using a combination of transmission lines such as the low frequency prototype presented in this chapter. For this design, a low loss, well matched, via-less CPW-to-Microstrip transition was realized to ease the field distribution from the CPW-fed slot antenna to the microstrip detector circuit.

A cross-section representation of each segment of the transition is depicted in Figure 3.12. Here, it is observed that the transition consists of two segments: a CPW-to-grounded coplanar waveguide (GCPW) and a GCPW-to-Microstrip segment.

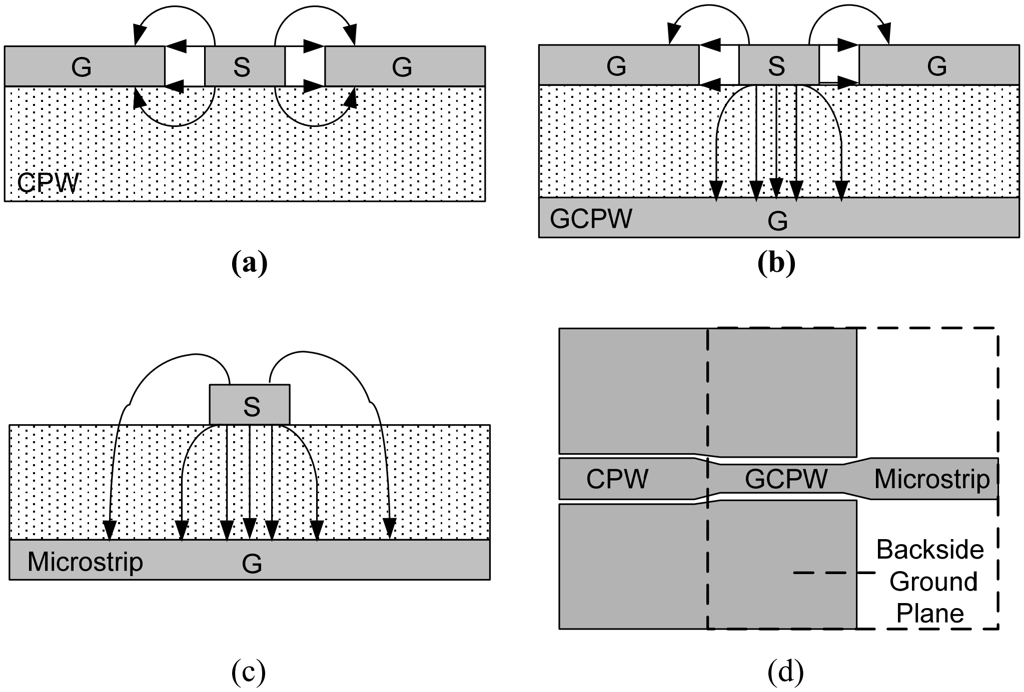

Figure 3.12: Via-less CPW-to-Microstrip Transition Sections. (a) CPW, (b) GCPW, (c) Microstrip Cross-sections, (d) Transition Top View.

The GCPW section depicted in Figure 3.12b is responsible for electrically shorting the CPW and Microstrip grounds together. This is accomplished by making the width of the GCPW's ground be a ¼λ wide, which becomes a short circuit at the design frequency of 2.5GHz. In addition, it should be noted that the GCPW section eases the field distribution of the CPW-to-Microstrip transition, thus reducing the power loss due to radiation and reflection present at the interface.

The width of the midsection center conductor and tapering angle of the transition presented in Figure 3.12d were optimized in Momentum while monitoring its insertion loss (IL), RL, and radiation characteristics. The optimized transition presented an IL better than 0.4dB over a frequency range of 1GHz to 3.6GHz, which is illustrated in

Figure 3.13. In addition, a RL better than 25dB was achieved at the design frequency and an S11 ≥ 15dB over a frequency range of 1GHz to 4GHz, also illustrated in Figure 3.13.

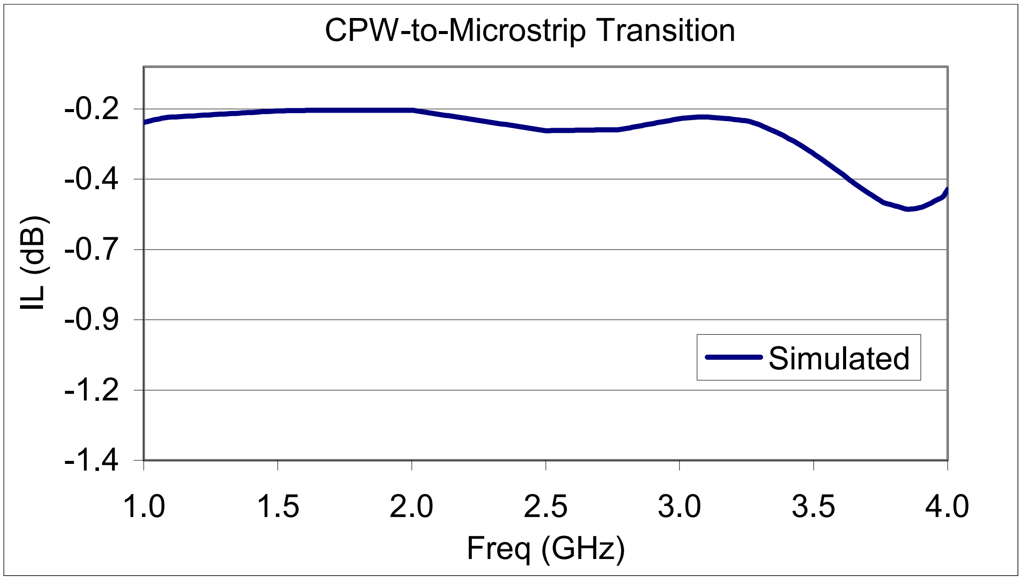

(a)

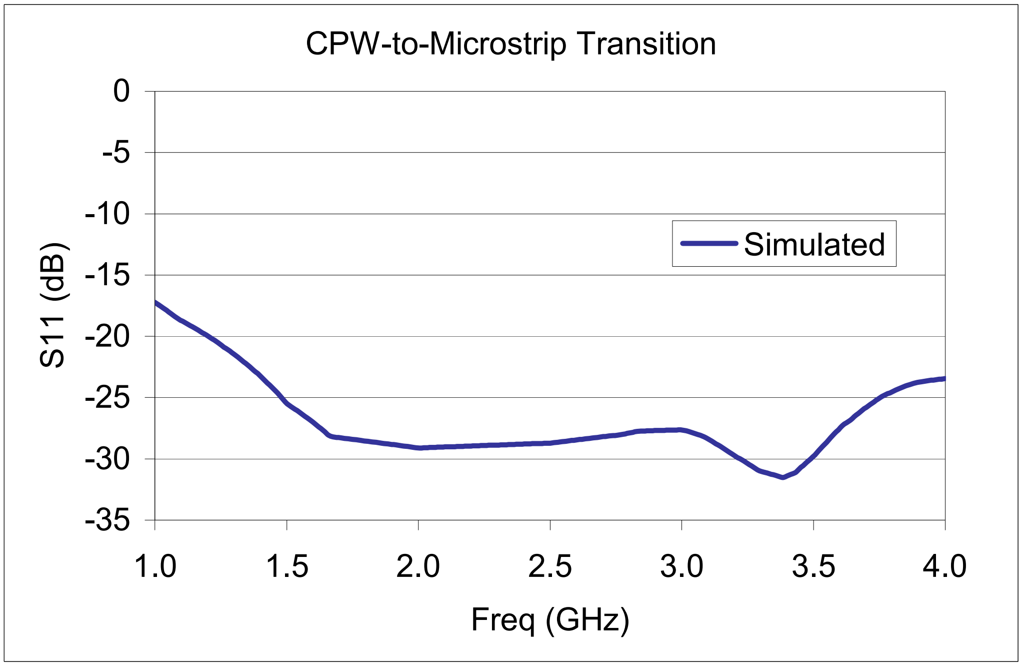

(b)

Figure 3.13: CPW-to-Microstrip Transition Simulated Data. (a) Insertion Loss and (b) Return Loss.

The slot antenna with the transition incorporated was re-simulated to study its effects on the antenna's RL and radiation characteristics. This data was extracted from Momentum and compared to the wide slot antenna characteristics previously presented in Chapter 2. Figure 3.14 shows the integrated layout in Momentum along with the simulated RL comparison between the wide slot antenna with and without the transition. The simulated results presented in Figure 3.14b shows that the transition does not have a significant effect on the RL of the antenna at the design frequency of 2.5GHz. The main difference between the two simulations is the fact that the bandwidth of the antenna with the transition decreased by 8%.

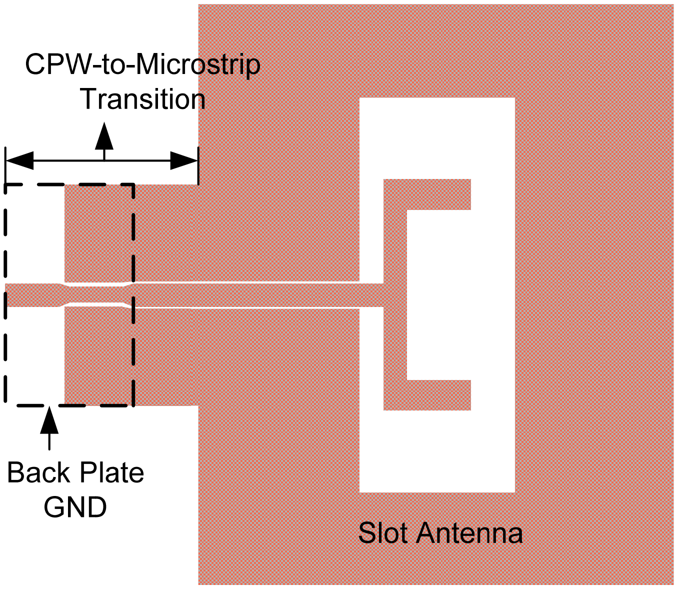

(a)

Figure 3.14: 2.5GHz Wide Slot Antenna and CPW-to-Microstrip Transition Integration. (a) Momentum Layout and (b) RL Comparison Between the Simulated Antenna with and without the Transition.

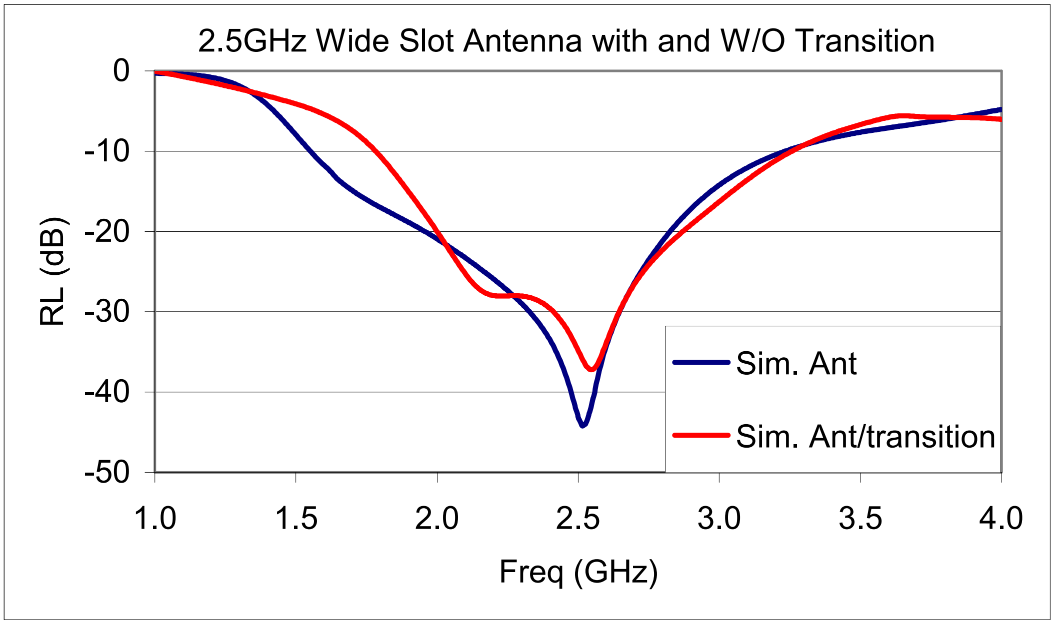

(b)

Figure 3.14: (Continued)

Figure 3.15 illustrates a comparison between the simulated radiation pattern for the antenna with and without the transition. These simulated results show that integrating the transition presents little or no effect on the radiation characteristics of the antenna.

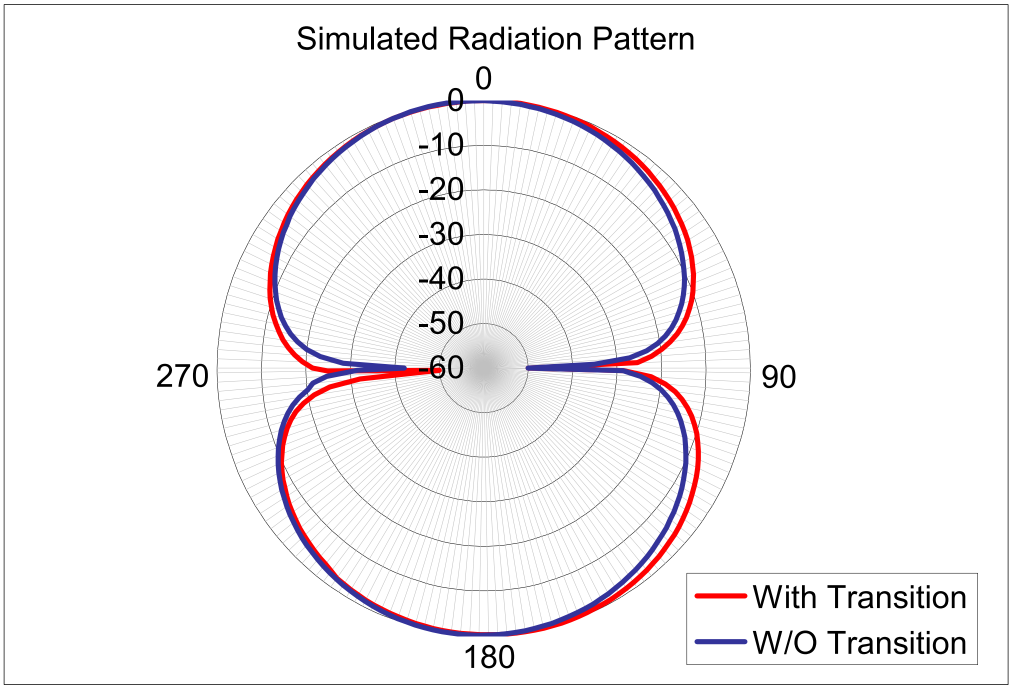

Figure 3.15: Radiation Pattern Comparison Between the Simulated Wide Slot Antenna with and without the Transition in Place.

3.4 Results and Comparison

3.4.1 2.5GHz Detector Circuit

The optimized detector circuit was fabricated on an FR-4 board using the same techniques previously mentioned in Section 2.6.1. To measure the RL of the fabricated detector two types of calibrations were performed in order to remove the systematic errors from the measured data. The RL of the detector was first measured using the same SOLT calibration technique mentioned in Section 2.6.1. This technique does not take into account the connector losses since the calibrated reference plane is at the edge of the connector as depicted in Figure 3.16. Previously, it was mentioned that these connector losses were responsible for the losses found in the measured antenna's RL. The second calibration technique used to measure the detector circuit consisted of a Thru-Reflect-

Line (TRL) calibration. The TRL's design and results are described in Appendix C. This calibration technique takes into account the connector losses by putting the reference plane at the edge of the matching network.

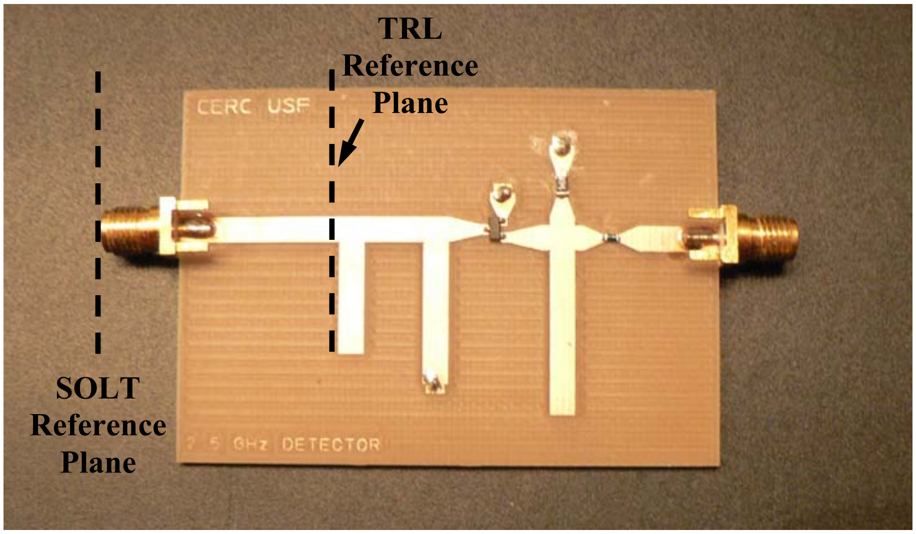

Figure 3.16: Photograph of the Fabricated 2.5GHz Detector Circuit with SOLT and TRL Calibration Reference Plane.

The RL of the detector circuit was measured using an HP-8753D VNA. Measurements performed with the SOLT calibration show that the SMA connector used limits the RL of the detector circuit to approximately 28dB, which is depicted in Figure 3.17. This result agrees well with the discrepancy found in Chapter 2 between the simulated and measured antenna RL. It should also be noted that the measurement performed with the TRL calibration agrees very well with the simulated data since more losses are taken into account. As mentioned in Chapter 2, the shift in frequency is mainly due to the inaccuracy of the FR-4 dielectric constant.

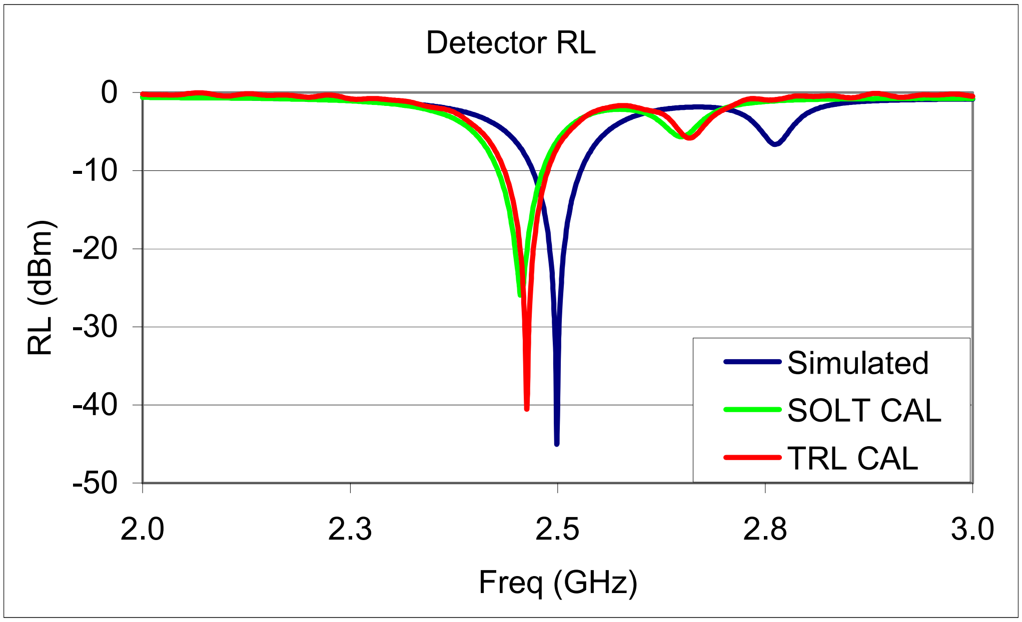

Figure 3.17: 2.5GHz Detector Circuit Simulated vs. Measured RL Using Different Calibration Techniques.

Now that the detector circuit is well matched to the source impedance of 50 Ω, it was tested for its performance by measuring the square-law region and sensitivity. A diagram of the square-law measurement setup along with a brief description on how to make square-law measurements is presented in Appendix B. The equipment utilized for this measurement consisted of an RF source, in this case the internal source of the HP-8753D VNA, the Anritsu ML-2438A power meter, a variable step attenuator, and the HP-3478A digital multimeter. The accuracy of the measurement is limited by the ability of the variable step attenuator to accurately provide the same attenuation between measurements, and by the digital multimeter's ability to detect small voltages. Table 3.2 presents the measured input power and output DC voltage as a function of attenuation setting. Here, it is observed that the variable step attenuator presents up to 0.2dB error tolerance between input power measurements.

Table 3.2: Measured Input Power and Output Voltage as a Function of Attenuation Setting.

Attenuator Setting	Input Power in (dBm) ± 0.2dBm	Output Voltage (mV)	Input Power in (mW) ± 1mW	Sensitivity in (mV/mW)
0	8.06	2223	6.397	347.488
2	6.05	2014	4.027	500.103
4	3.97	1793	2.495	718.754
6	2.02	1587	1.592	996.729
8	-0.05	1351	0.989	1366.644
10	-2.18	1153	0.605	1904.712
12	-4.18	956	0.382	2502.983
14	-6.27	772	0.236	3270.524
16	-8.18	619	0.152	4070.902
18	-10.25	485	0.0944	5137.381
20	-11.90	394	0.0646	6102.337
22	-13.90	303	0.0407	7437.768
24	-15.98	229	0.0252	9074.767
26	-17.95	172.3	0.0160	10746.95
28	-20.02	126.70	9.954e-3	12728.48
30	-21.90	93.12	6.457e-3	14422.58
32	-23.93	66.74	4.046e-3	16496.29
34	-26.05	46.43	2.483e-3	18698.15
36	-28.07	32.00	1.56e-3	20518.71
38	-30.14	21.3	9.68e-4	21997.82
40	-32.11	14.00	6.15e-4	22757.68
42	-34.09	9.29	3.9e-4	23824.06
44	-36.18	5.95	2.41e-4	24689.77
46	-38.15	3.93	1.53e-4	25668.03
48	-40.23	2.56	9.48e-5	26992.3
50	-42.40	1.6	5.75e-5	27804.81
52	-44.39	1.1	3.64e-5	30226.84
54	-46.5	0.7	2.24e-4	31267.85
56	-48.49	0.45	1.42e-5	31784.29
58	-50.65	0.3	8.61e-6	34843.46
60	-52.45	0.2	5.69e-6	35158.47

From the data presented above, the square-law region of the detector can be identified by plotting the output DC voltage as a function of the input power. The square-law region is the section of the plot that follows a linear relationship between the input power and output DC voltage. The dynamic range of this detector was found to be approximately from -17dBm to -50dBm. This range is dictated by distortions at high power levels and by the noise floor at low power levels. This behavior along with the sensitivity of the device is illustrated in Figure 3.18. The sensitivity of the device was obtained by plotting the ratio of output voltage to input power (W) vs. the input power (dBm).

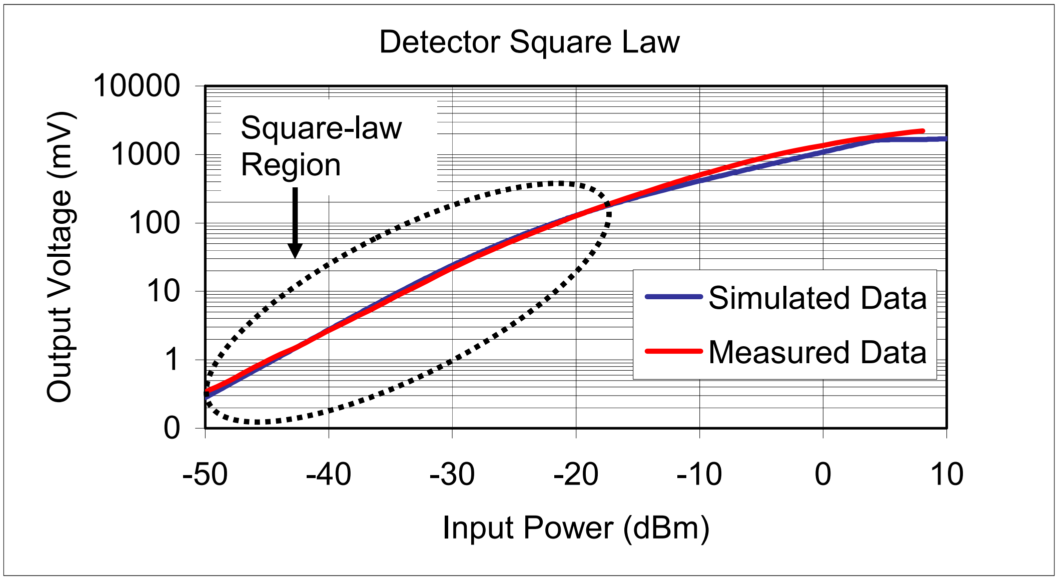

(a)

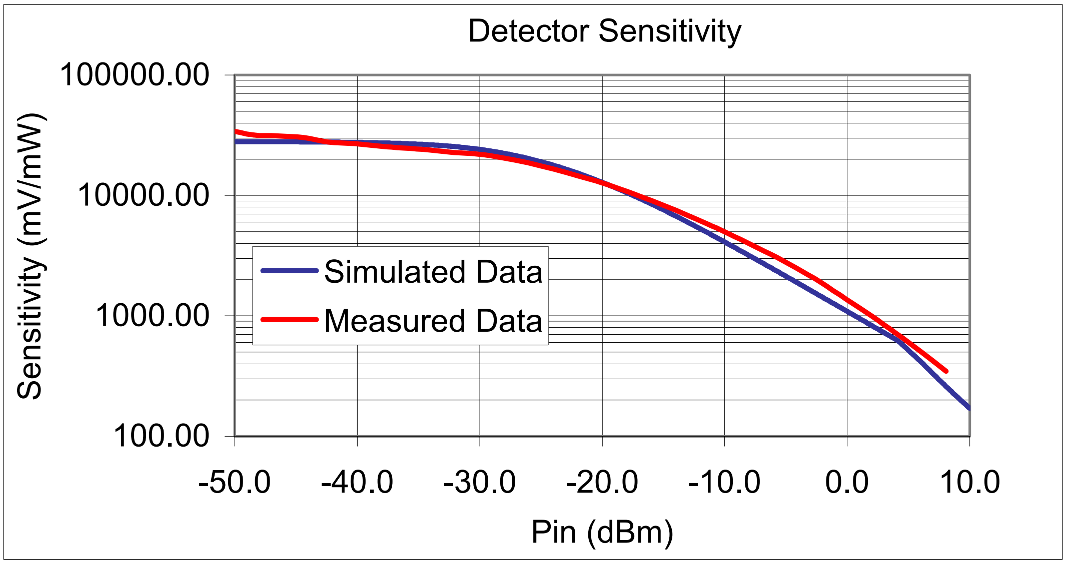

(b)

Figure 3.18: Simulated vs. Measured Detector Performance. (a) Square -Law Region and (b) Sensitivity.

3.4.2 Via-less CPW-to-Microstrip Transition Results

The CPW-to-Microstrip transition was also fabricated on a FR-4 board and measured using the HP-8753D VNA. A visual of the fabricated transition is depicted in Figure 3.19.

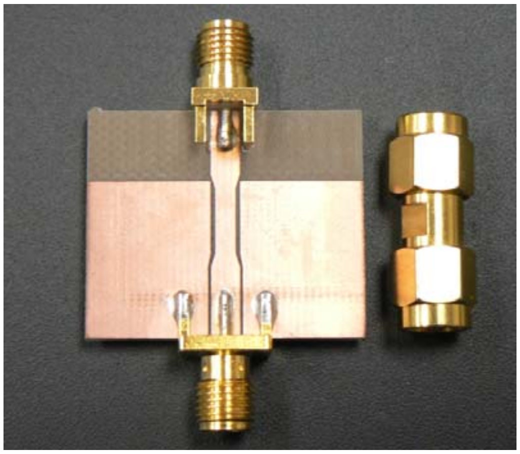

Figure 3.19: Visual of the 2.5GHz Via-less CPW-to-Microstrip Transition.

It is observed that the transition is not bigger then a regular SMA M-M connector. From the measured results it is observed that the CPW-to-Microstrip transition presents an IL better than 0.4dB over a frequency span of 1GHz – 3.6GHz and an IL of 0.2dB at the design frequency of 2.5GHz. The discrepancies between the simulated and measured data are mainly due to the connector losses and dielectric constant variations within the FR-4 board.

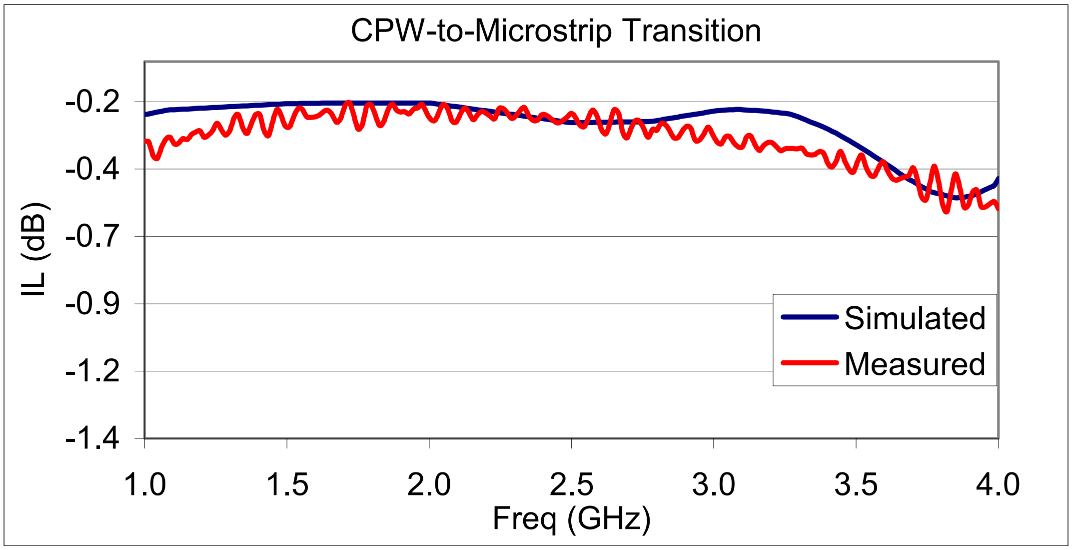

(a)

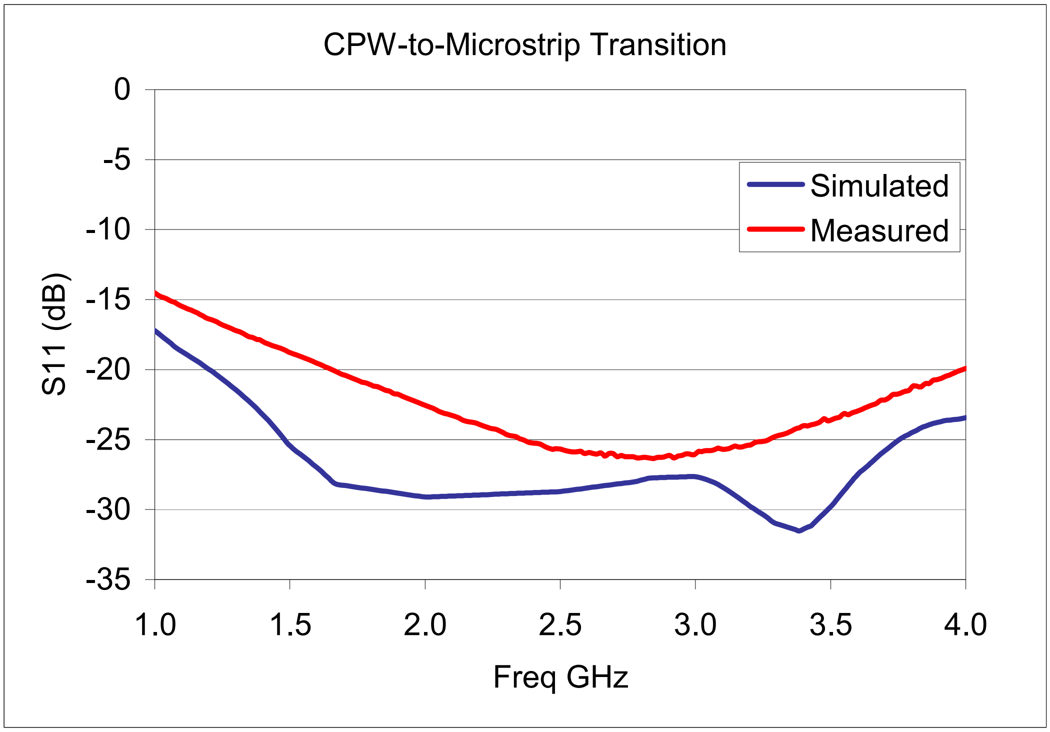

(b)

Figure 3.20: Simulated vs. Measured CPW-to-Microstrip Transition. (a) Insertion Loss and (b) Return Loss.

3.4.3 Antenna/CPW-to-Microstrip Integration Results

The antenna was integrated with the CPW-to-Microstrip transition on a single FR-4 board in order to check its performance. An image of the fabricated antenna as well as a comparison between simulated and measured RL is presented in Figure 3.21. The measurement correlates well to the simulated slot antenna. The antenna and transition integration still sustain a 70% bandwidth measured at a RL ≥ 10dB. In addition, it provides a RL = 22dB at the design frequency of 2.5GHz. As mentioned before, the SMA connector adds losses to the measurements which will not be present in the full Rectenna element integration consisting of the slot antenna, the CPW-to-Microstrip transition, and the detector circuit.

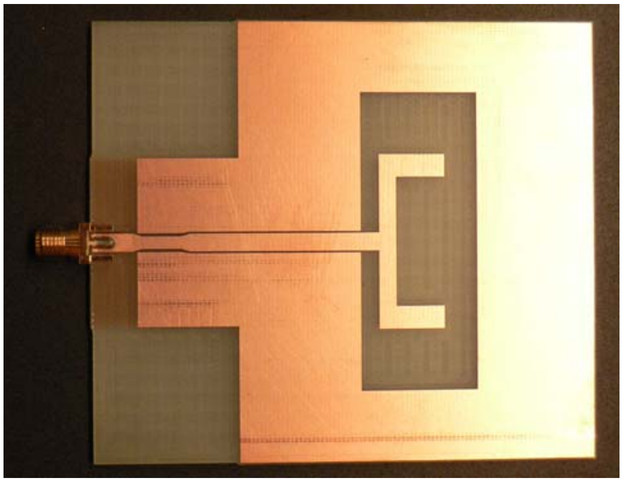

(a)

Figure 3.21: (a) Visual of the Fabricated Slot Antenna/Transition. (b) Comparison Between the Simulated Antenna with and without Transition and Measured Antenna with Transition.

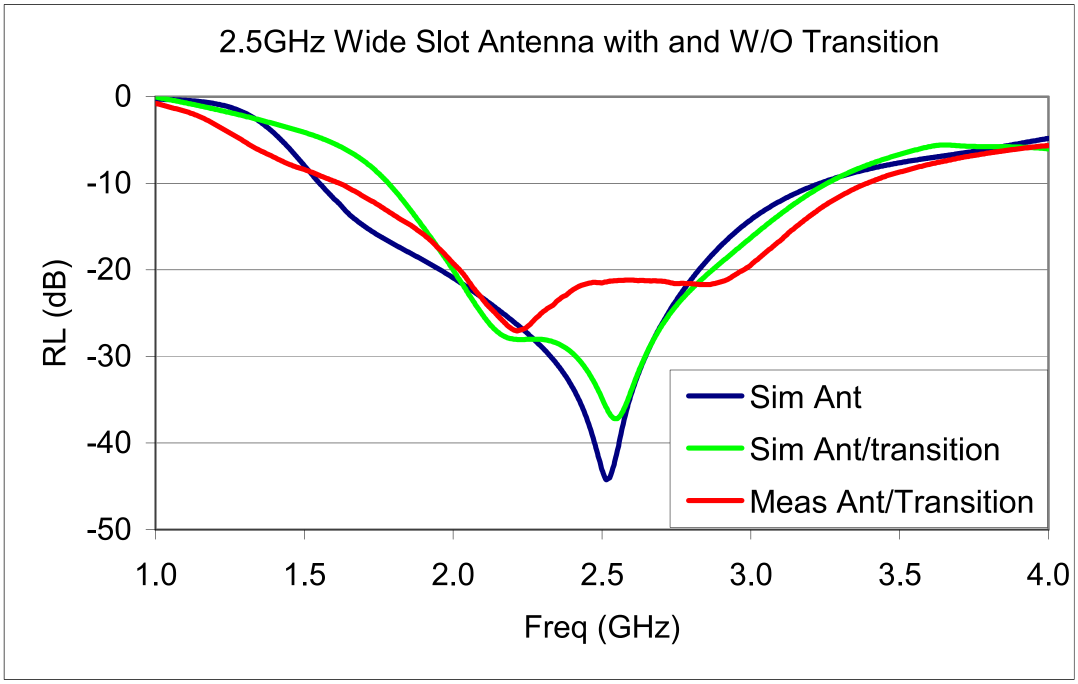

(b)

Figure 3.21: (Continued)

Finally the radiation pattern of the integrated antenna was captured using the same techniques presented in Chapter 2 and compared to the simulated radiation pattern. The results depicted in Figure 3.22 shows good agreement to the simulated radiation pattern. From these results it is concluded that the transition presents little or no affect on the antenna return loss and radiation characteristics of the slot antenna.

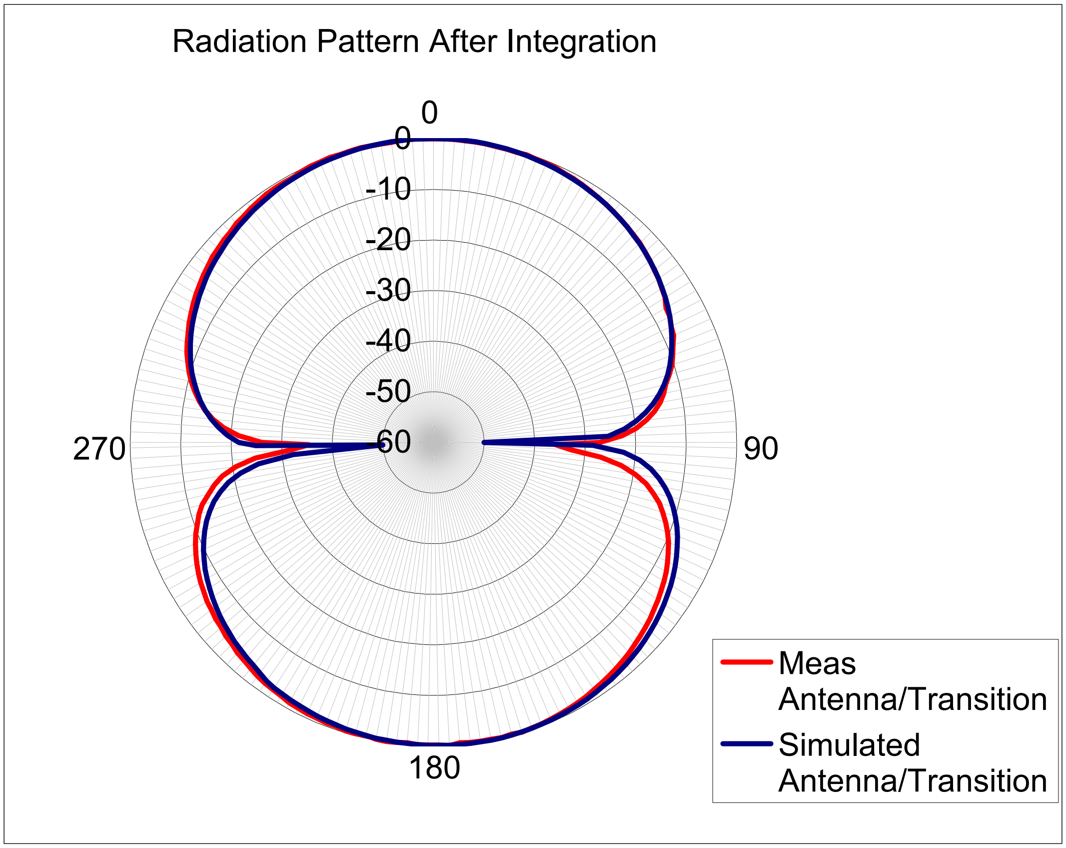

Figure 3.22: Simulated vs. Measured Radiation Pattern for the Integrated Antenna.

3.4.4 2.5GHz Rectenna Element Integration

After characterizing each of the Rectenna elements individually, they were fabricated on a single FR-4 board, and measured for its sensing characteristics. A visual of the fully integrated Rectenna element is depicted in Figure 3.23. The Rectenna elements connected by a M-M connector were measured and compared to the fully integrated Rectenna. The setup of the measurement is depicted in Appendix B. Figure 3.24 illustrates a comparison of the output voltage from both the Rectenna element and the individual devices connected by a M-M barrel. The output DC voltage is plotted as a function of the input power delivered to the detector circuit by the receiving antenna. Both measurements were taken at a transmitting - receiving distance of 4.5 feet.

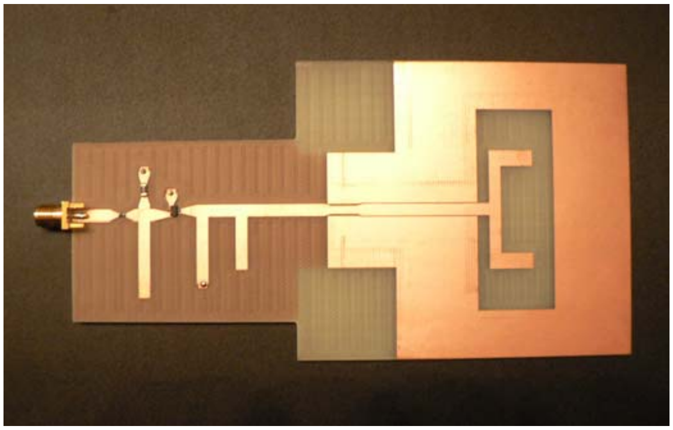

Figure 3.23: Photograph of the Fully Integrated Rectenna Element.

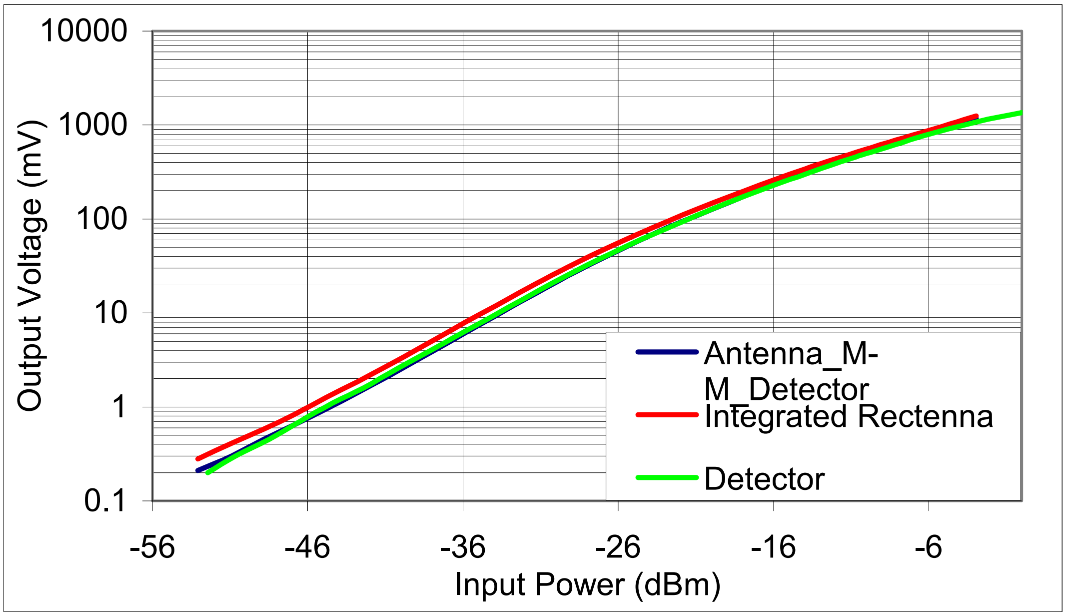

Figure 3.24: Comparison Between the Measured Rectenna Element in a Single FR-4 Board vs. the Rectenna Element Connected by M-M Barrel.

The Rectenna element fabricated within a single FR-4 board provides a higher output voltage than the Rectenna elements connected by a M-M connector. This is due to the fact that the integrated Rectenna is better matched at the design frequency, thus reducing the M_s which translates into maximum power transfer.

The input power presented in Figure 3.24 was obtained by measuring the input power incident to the transmitting antenna and then using Friis transmission equation 3.17 to calculate the power received by the slot antenna.

$$\frac{P_r}{P_t} = e_{cdt} \cdot e_{cdr} \cdot \left(1 - |\Gamma_t|^2\right) \cdot \left(1 - |\Gamma_r|^2\right) \cdot \left(\frac{\lambda}{4\pi R}\right)^2 D_t(\theta_t, \phi_t) \cdot D_r(\theta_r, \phi_r) |\hat{\rho}_t \cdot \hat{\rho}_r|^2 \quad (3.17)$$

If both the transmitting and receiving antennas are well matched and aligned for maximum directional radiation and reception, given that there are no polarization losses, equation 3.17 reduces to its simplest form presented by equation 3.18.

$$\frac{P_r}{P_t} = \left(\frac{\lambda}{4\pi R}\right)^2 G_{0t} G_{0r} \quad (3.18)$$

where $\left(\frac{\lambda}{4\pi R}\right)^2$ is the free-space loss factor, which takes into account the losses due to the spherical spreading of the energy by the antenna. P_t and P_r represent the transmitting and receiving power, respectively, and G_{0t} and G_{0r} represent the maximum gain of the transmitting and receiving antenna, respectively. For these calculations it was assumed that both antennas were well matched at the design frequency and were aligned to remove the polarization losses. Under these conditions, the antenna's P_r is the summation of P_t, G_{0t}, G_{0r}, and the free-space loss factor as long as the terms are expressed in dB. Appendix B presents the measurement setup along with the data obtained for the Rectenna element with and without a M-M connector.

3.5 Chapter Summary and Conclusions

In this chapter a brief description of the background theory, design, and testing of a detector circuit was presented. Measured data correlated very well to the simulated data. The detector circuit offers a dynamic range of -17dBm to -50dBm, which agrees well with the literature. In addition, by comparing the measured RL using two types of calibration techniques, it was concluded that the discrepancies between the simulated and measured RL is mainly caused by the SMA connector parasitics. Also in this chapter, the sketch of the design of a via-less CPW-to-Microstrip was presented showing a great deal of correlation to the simulated data. This transition presents an IL better than 0.4dB over a frequency range of 2.6GHz and a RL better than 15dB over a frequency span of 4GHz. Finally, the Rectenna elements were fabricated within a single FR-4 board and compared to the Rectenna elements connected by a M-M barrel. The measured result shows that the fully integrated Rectenna element provides a higher output DC voltage than the Rectenna element connected by a M-M barrel.

Chapter 4

94GHz Antenna Design

4.1 Introduction

4.1.1 Millimeter Wave Band Characteristics

In the past twenty years the interest in millimeter wave devices has increased dramatically due to the realization that there are some limitations to what can be achieved with microwave, infrared, and optical systems. Infrared and optical systems provide extremely high resolution, but they suffer from many disadvantages such as dust, smoke, and fog conditions which degrade the overall performance of the system. According to Bhartia and Bahl [24], the resolution of millimeter wave sensors is not significantly lower than that obtained with infrared and optical sensors, and in conjunction with other techniques such as injection locking, phase locking, and power combining of multiple diodes, sensory system performance can be improved. The short wavelength characteristic of millimeter waves in combination with its interaction with atmospheric constituents and wide operating bandwidths provide many advantages as well as some disadvantages.

4.1.2 Advantages and Disadvantages

One of the main advantages at millimeter wave frequencies come from its short wavelengths characteristics which translate into a reduction of component size. This significant reduction in the component size allows for the production of compact systems, which are desirable for missiles, satellites, and aircraft applications. In addition, compact antenna arrays can be realized to provide narrow beamwidths, which in turn provide greater resolution and precision in target tracking and discrimination applications. Devices that operate at millimeter wave frequencies also present extremely wide bandwidth. The millimeter wave band ranges anywhere from 10mm to 1mm in wavelength. Figure 4.1 illustrates that the main windows in the millimeter wave range exist at 8.6, 3.2, 2.1, and 1.4mm wavelength corresponding to frequencies of 35, 94, 140, and 220GHz, respectively. As seen in Figure 4.1, the bandwidths available at each of these windows are extremely large, and are approximately equal to 16, 23, 26, and 70GHz, respectively [25].

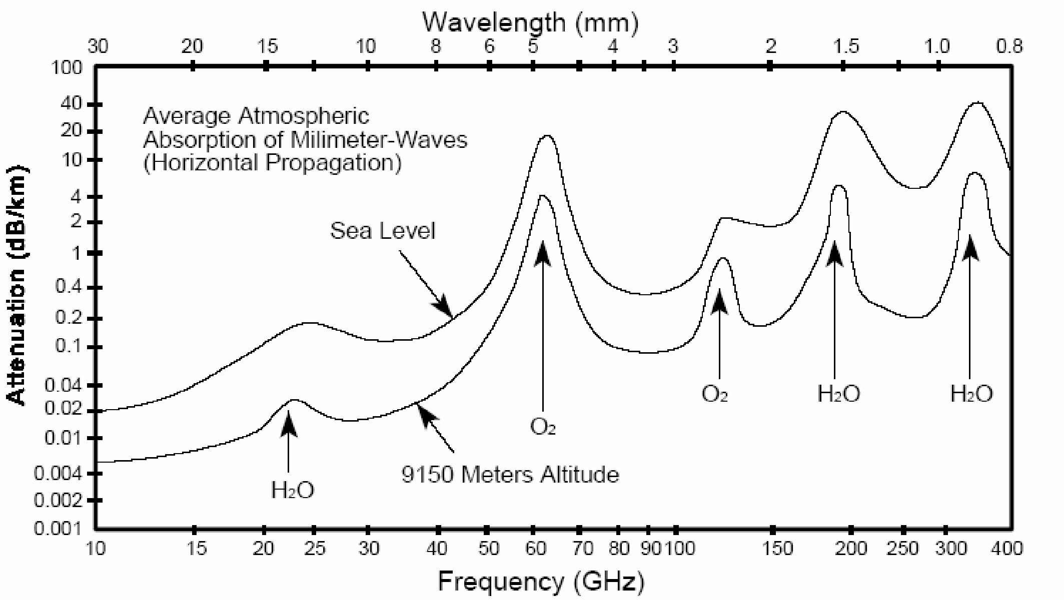

Figure 4.1: Millimeter Wave Atmospheric Absorption for Horizontal Propagation [25].

These large bandwidths allow for high information rate capability, which enables obtaining fine target signature, very high range resolution for precision tracking, target identification in radars, and high sensitivity radiometers. Finally, environmental interaction characteristics of millimeter wave devices such as atmospheric attenuation and losses due to aerosol, dust, smoke, and battlefield contaminants are lower than in infrared and optical frequencies; making millimeter wave systems ideal for military applications.

Even though millimeter wave frequencies provide multiple advantages over microwave, infrared, and optical frequencies, there are some obvious limitations. For instance, smaller component size increases the need for higher precision in manufacturing, thus increasing the overall cost of the device. Furthermore, millimeter wave component production quantities are lower which subsequently increases the cost of the devices needed for system design, integration, and characterization. Furthermore, the inherently narrow beamwidth of millimeter wave antennas is not suitable for large volume searches. Another disadvantage is that the range capability of radars at millimeter wave is reduced in bad weather, and the backscattering in rain, which can imitate targets, is also a limitation of millimeter wave systems. The atmospheric attenuation due to precipitation rate is illustrated in Figure 4.2 [25].

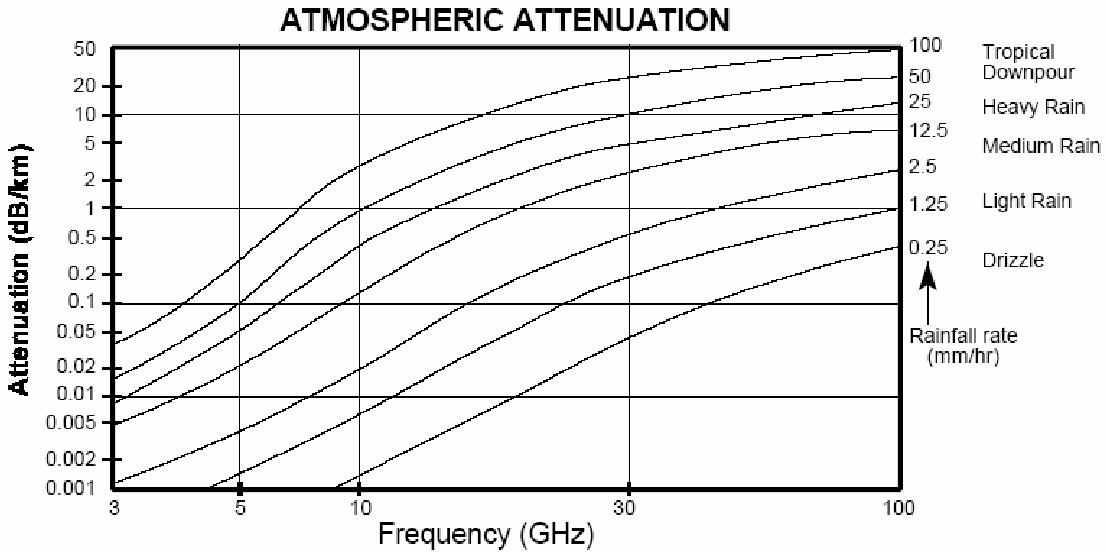

Figure 4.2: Atmospheric Attenuation Due to Precipitation Rate [25].

Wicker and Webb [26] provided some of the advantages of millimeter waves over microwave and optical frequencies for radar applications, which are illustrated in Table 4.1. Here it is observed that millimeter wave frequencies present at least fair operation under any of the mentioned circumstances.

Table 4.1: Radar System Performance in Millimeter Wave, Microwave, and Optical Frequencies.

Radar Characteristics	Microwave	Optical	Millimeter Wave
Tracking accuracy	Poor	Good	Fair
Classification/ identification	Poor	Good	Fair
Covertness	Poor	Good	Fair
Volume search	Good	Poor	Fair
Adverse weather performance	Good	Poor	Fair
Performance in smoke, aerosol, dust, etc.	Good	Fair	Good

Based on the brief description of millimeter waves mentioned above and the frequency scalability of microwave components, it was decided to scale the slot antenna presented in Chapter 2 up in frequency, and study its characteristics at 94GHz. The 94GHz frequency window was chosen since it is one of the military frequency bands, and provides multiple commercial applications as well.

4.1.3 Applications

Even though millimeter wave systems cannot replace microwave or optical systems entirely, they do provide a wide range of applications in the four major areas of wireless communications. Table 4.2 presented by Bhartia and Bahl [24] summarizes some of the main applications of millimeter waves. The successful design and characterization of the

Rectenna element mentioned in the preceding chapters at millimeter wave frequencies could significantly lower the overall cost of millimeter wave systems.

Table 4.2: Millimeter Wave Applications in the Four Major Areas of Wireless Communication [24].

Radar

- Low angle tracking
- Secure military radar
- Interference free radar
- High resolution radar
- Imaging radar
- Ground Mapping
- Space object identification
- Harbor surveillance radar
- Target characteristics
- Hand-held radar
- Radar cross-section measurements
- Remote sensing of environment
- Surveillance
- Target acquisition
- Navigation
- Obstacle detection
- Missile guidance
- Fuses
- Airport surface detection radar
- Target designators
- Range finders
- Active missile seekers

Communications

- Secure military communications
- Point to point extremely wideband communications
- Interference free communications
- Satellite to satellite communications
- Earth to space communications
- LPJ communications
- Railroad communications

Radiometry

- Remote sensing of the environment
- Radio astronomy
- Ship detection
- Space-based radiometers
- Ground target detection
- Missile detection
- Missile guidance
- Clear air turbulence sensor

Instrumentation

- Plasma diagnostics
- Rocket exhaust plume measurements
- Remote vibration sensor
- Model radar cross-section measurements
- Automatic braking
- Spectroscopy
- Prediction of blast focusing

4.2 94GHz CPW-fed Slot Antenna Design

In the past three decades millimeter wave sources, circuits, and systems have received a great deal of attention. Antennas, on the other hand, have not been extensively studied at millimeter wave frequencies. This is probably due to the fact that microwave antennas can be scaled up in frequency and still present similar radiation characteristics. According to Bhatia and Bhal [24] the recent commercial and military applications in areas such as high-resolution radars, missile guidance, short-range communication systems, and radiometric sensors have emphasized the need for the development of a wide variety of antennas that satisfy each system's requirements. Many antenna configurations such as leaky wave antennas, dielectric rod antennas, and microstrip antennas have been studied and developed. In order to reduce the cost, size, and weight of the millimeter wave system, a low profile planar antenna is needed.

The slot antenna design presented in Chapter 2 fits this description and can be easily integrated with IC and CMOS technology. In addition, slot antennas can be conformed to different surfaces in aircraft, missiles, rockets, space shuttles and so forth. In order to successfully implement the wide slot antenna presented in Chapter 2 at millimeter wave frequencies some key considerations have to be taken into account. For instance, at microwave frequencies substrates are usually much thinner than the dielectric wavelength (λ_d). This is not the case at millimeter wave frequencies, where the commercially available substrate thicknesses are usually comparable or thicker than λ_d. The likelihood of surface waves propagating through the substrate increases with the increase in the dielectric constant and thickness of the substrate.

4.2.1 Surface Wave in Silicon

A high resistive silicon substrate was chosen for this design since it can be easily integrated with IC and CMOS technologies. In order to design a high performance antenna on a silicon substrate at millimeter wave frequencies some limitations need to be overcome. The high dielectric constant of the silicon substrate (ε_r = ~11.7), and the discontinuities present within the radiating element imply that surface waves can be easily generated and propagated through the substrate; potentially increasing side lobe levels, coupling between radiating elements, and reducing the antenna's efficiency.

At 94GHz the dielectric wavelength of silicon is approximately 100µm, which is thinner than some of the commercially available silicon wafers (400µm, 250µm, and 100µm). According to Luy et al. [27], the two possible surface wave modes for a grounded silicon substrate are designated as the transverse magnetic (TM) and the transverse electric (TE) modes. The cut-off frequencies for a given Nth order TE or TM mode are provided by equations 4.1 and 4.2.

$$fc_{TM} = \frac{c_0 N}{2h\sqrt{\varepsilon_r - 1}} \tag{4.1}$$

$$fc_{TE} = \frac{c_0 (2N+1)}{4h\sqrt{\varepsilon_r - 1}} \tag{4.2}$$

where c_0 is the speed of light in free space, h is the substrate thickness, and ε_r is the dielectric constant. Peter [28] also stated that the cut-off frequency of the first order microstrip mode is given by equation 4.3.

$$fc,_{HE1} = \frac{c_0 Z_0}{2\eta_0 h} \tag{4.3}$$

where η_0 = 377Ω is the free space characteristic impedance and Z_0 is the characteristic impedance of the line. From equations 4.1 and 4.2 it can be observed that the thickness and the dielectric constant of the substrate has a major effect on the cut-off frequency of the higher order modes. It should also be noted that the TM_0 mode has a zero cut-off frequency and is always present in the substrate. As the substrate thickness increases, more surface waves can exist, which makes coupling of the lower order modes stronger. According to Gauthier et al. [29], the higher order modes can be made non-propagating by minimizing the substrate thickness. The recommended substrate thickness is on the order of $\lambda_d/10$. For this reason, it was decided to design the 94GHz wide slot antenna with U-shaped tuning stubs on a 10μm high resistivity silicon membrane.

4.2.2 Substrate Thickness Characterization Using Momentum

The 94GHz slot antenna design started by investigating the effects of the substrate thickness on the radiation characteristics of the antenna. A parametric study was performed in Momentum by varying the substrate thickness to 400μm, 250μm, 100μm, and 10μm while monitoring the antenna’s efficiency and 3D radiation pattern. The Momentum 3D plot presented in Figure 4.3 illustrates how the substrate thickness affects the radiation characteristics of the antenna. Figure 4.3a through 4.3c show that a large portion of the radiated fields goes into the substrate. In addition, dominating side lobes are observed when the substrate thickness is comparable to the dielectric wavelength. Momentum, however, assumes an infinite substrate, which can be misleading when it comes to surface waves. In a finite substrate, the field can propagate through the substrate and radiate at the edges presenting end-fire radiation. As illustrated in Figure 4.3, the

10μm substrate thickness closely resembles the radiation pattern presented by the 2.5GHz antenna prototype.

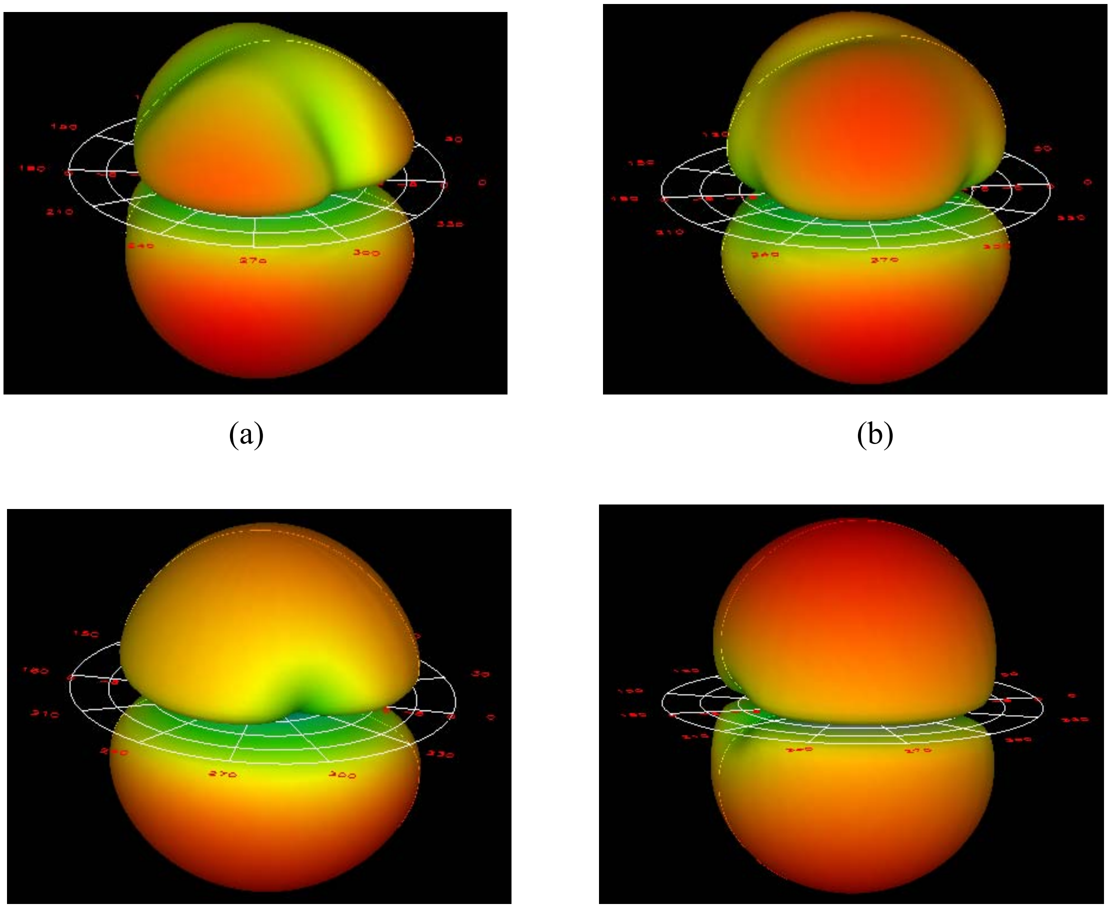

(a) (b)

(c) (d)

Figure 4.3: 3D Radiation Pattern for the 94GHz Slot Antenna as a Function of Substrate Thickness. (a) 400μm, (b) 250μm, (c) 100μm, and (d) 10μm.

The parametric study presented above also illustrates that the antenna's efficiency is strongly dependent on the substrate thickness, which is presented in Table 4.3. The simulated result shows that the antenna efficiencies at 400μm, 250μm, 100μm, and 10μm are 19, 19.6, 46.9, and 99%, respectively. As in the 2.5GHz prototype, a perfect conductor was assumed in the simulation process.

Table 4.3: Slot Antenna Efficiency, Directivity, and Gain as a Function of Substrate Thickness.

Substrate Thickness (μm)	Directivity (dB)	Gain (dB)	Efficiency (%)
400	4.11	-3.115	19
250	5.74	-1.33	19.6
100	4.90	1.55	46.9
50	5.07	2.297	52.86
10	4.628	4.61	99

The Momentum layout of the 94GHz slot antenna on a 10μm silicon membrane is presented in Figure 4.4. Also in Figure 4.4, the simulated RL along with the phase of the 94GHz slot antenna is presented. The simulated result illustrates that the antenna is well matched at the design frequency of 94GHz and presents an impedance bandwidth of approximately 55% referenced to a RL ≥ 10dB. The phase plot also shows that the antenna goes through multiple resonances, which agrees well with the low frequency prototype presented in Chapter 2. Since large bandwidths are not required for this thesis work, the antenna was optimized to present a perfect match at the design frequency. If necessary, the bandwidth of the antenna can be easily increased by optimizing the tuning stub placement, length, and width.

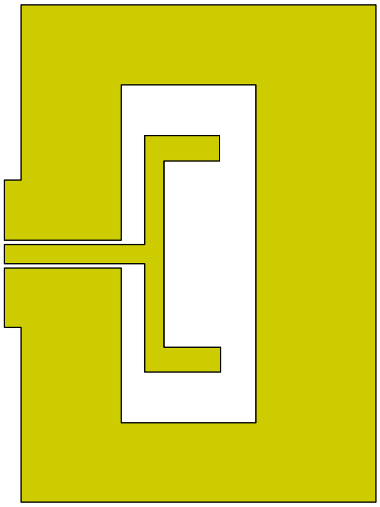
(a)

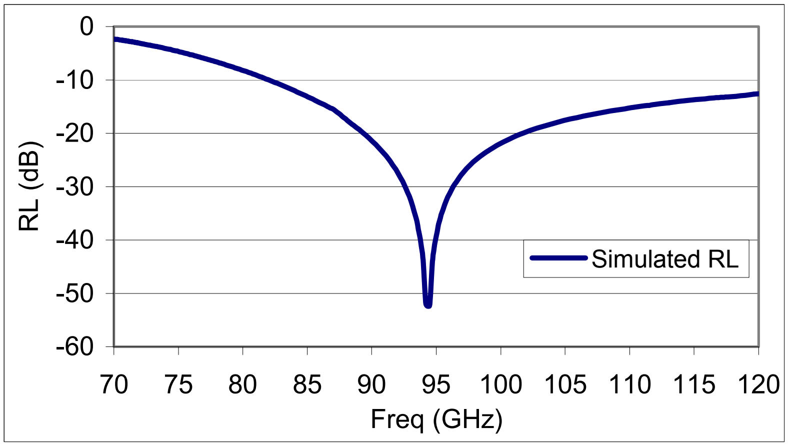

(b)

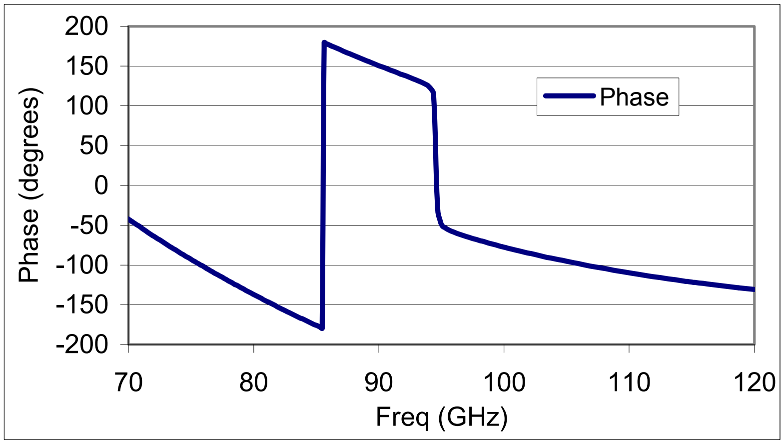

(c)

Figure 4.4: 94GHz Slot Antenna (a) Layout, (b) Simulated RL, and (c) Simulated Phase.

A comparison between the simulated radiation pattern of the 2.5GHz prototype and the 94GHz antenna is also presented in Figure 4.5.

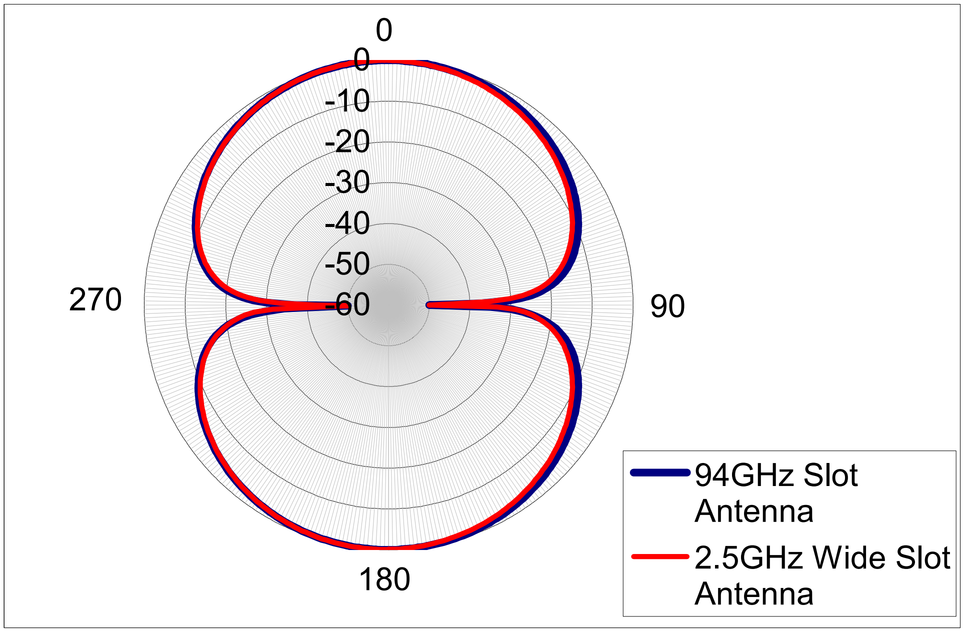

Figure 4.5: 94GHz vs. 2.5GHz Simulated 2D Radiation Pattern.

In Figure 4.5, it can be observed that the 94GHz antenna has the same radiation pattern as the low frequency prototype presented in Chapter 2. In addition, the simulated directivity and gain of the 94GHz antenna were found to be 4.628dB and 4.61dB. This translates to an efficiency of 99% under the assumption that gold is a perfect conductor. From these results, it can be concluded that the low frequency prototype slot antenna could be successfully scaled up in frequency while maintaining the same radiation characteristics.

4.2.3 TRL Standards and Substrate Thickness Issues

As mentioned before, in order to obtain the best efficiency and radiation pattern, the antenna had to be fabricated on a 10μm silicon membrane. The problem with this substrate thickness is that it cannot be probed without damaging the silicon membrane. Therefore, a set of TRL standards were designed in order to probe at a thicker section of the silicon substrate, in this case 250μm. Figure 4.6 illustrates the layout of some of the elements including a cross-section of the 10μm silicon membrane.

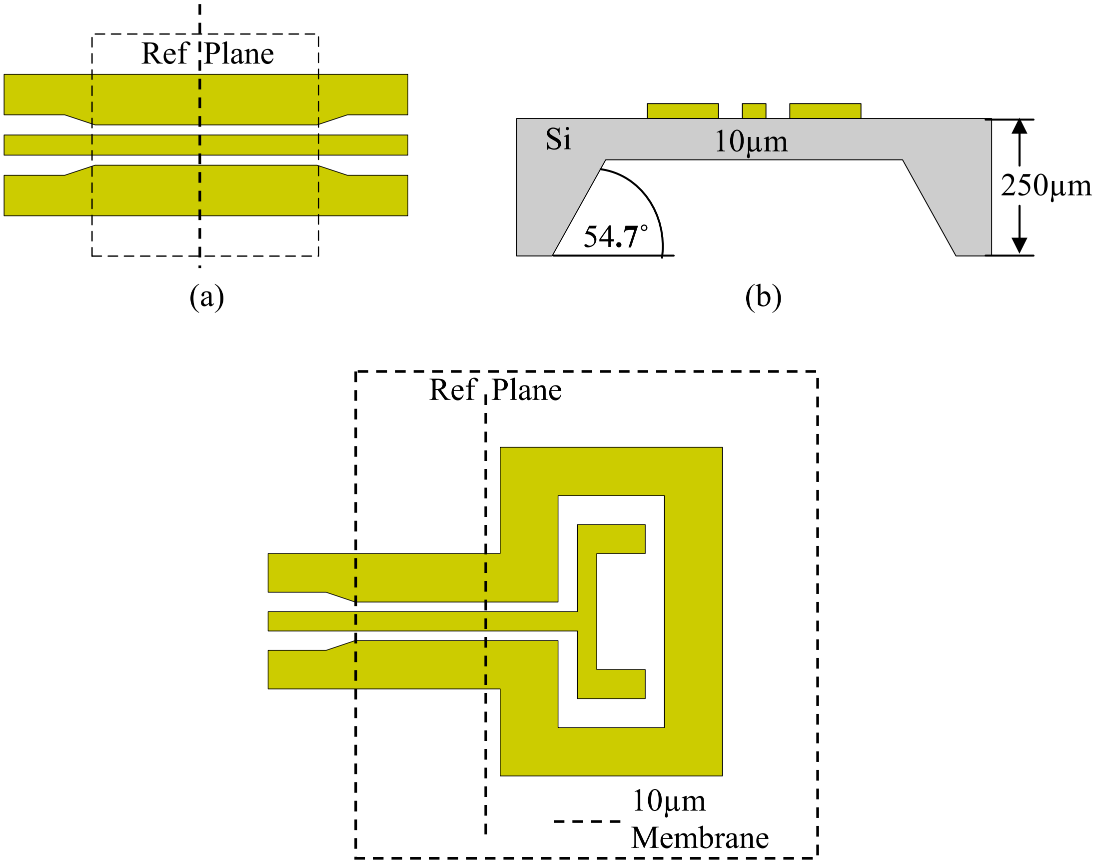

(a)

(b)

(c)

Figure 4.6: 94GHz Elements on a 10μm Silicon Membrane. (a) TRL Thru Standard, (b) Silicon Membrane Cross-Section, and (c) Slot Antenna.

The CPW slots' width decreases as the CPW line changes its thickness from 250μm to 10μm silicon membrane. This is the case since the dimensions of the CPW line depend on the substrate thickness. In order to account for the 54.7° slope at the edges of the silicon membrane, the ground planes of the CPW line were tapered to minimize the reflections present at the discontinuity. These reflections can give birth to higher order modes, which are undesirable at the measurement's reference plane. Thus, the length of the thru was designed to be as large as possible to ensure that the higher order modes die out by the time they reach the measurement's reference plane. According to Agilent Technologies [30], if enough separation between the two probes, and between the probes and the DUT, is not provided, coupling of the higher order modes could produce unwanted variations during the error correction process, which would translate into inaccurate measurements. A separation equal to two wavelengths between the two probe tips is usually recommended [30].

4.3 Results and Comparisons

The optimized 94GHz slot antenna along with the TRL calibration standards were fabricated on a bulk micromachined silicon membrane using standard lithography techniques, and measured using the Wiltron 360B Network Analyzer. A visual of the measurement setup along with the modules required for the *W* band measurements are presented in Appendix C. The TRL calibration standards along with the calibration results are also provided in Appendix C.

Twelve slot antennas and two sets of TRL calibration standards were realized on each 2" silicon wafer. Four of the antennas were designed to operate at a substrate thickness of 10μm. The other antenna sets were designed to operate at substrate thickness of 8μm, 9μm, 11μm, and 12μm in order to account for any minor discrepancies that would arise from fabrication. A photograph of the fabricated devices along with a visual of the back etched silicon membranes are depicted in Figure 4.7.

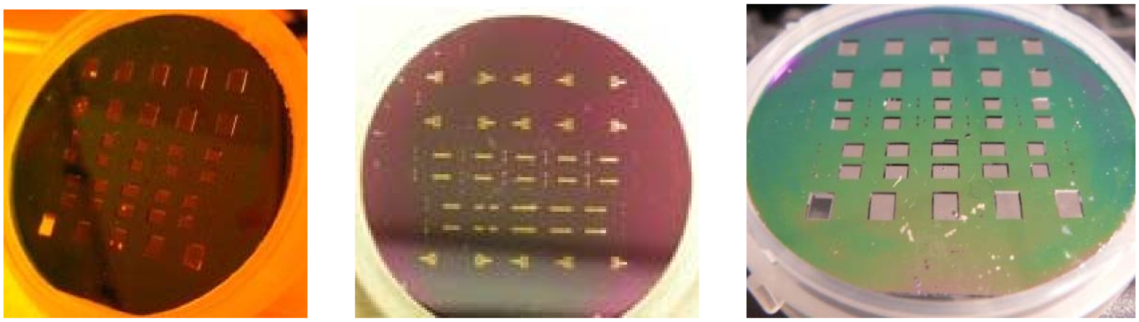

Figure 4.7: Visual of the Fabricated Devices. Right and Left Photograph Show the Fabricated Membranes.The Center Picture is the Top View of the Silicon Substrate.

For this project, a total of two silicon wafers were fabricated. The first successfully fabricated substrate, which is illustrated in Figure 4.7, contains silicon membranes varying in thickness from 15μm to 25μm. These thicknesses were measured using a profilometer. Figure 4.8 also illustrates a close up of the fabricated slot antenna and corresponding membrane, whose membrane thickness was measured to be approximately 20μm.

(a) (b)

Figure 4.8: Close up Visual of: (a) the 94GHz Slot Antenna and (b) 20μm Silicon Membrane.

Each of the antennas was measured using two types of calibrations standards. The best return loss obtained with the CS-5 calibration kit is illustrated in Figure 4.9. It can be seen that the antenna presents a well matched condition at the design frequency of 94GHz. The discrepancies between the simulated and measured data are due in part to the thickness variation within the membrane, and the fact that there is an error tolerance of 2μm within the mask.

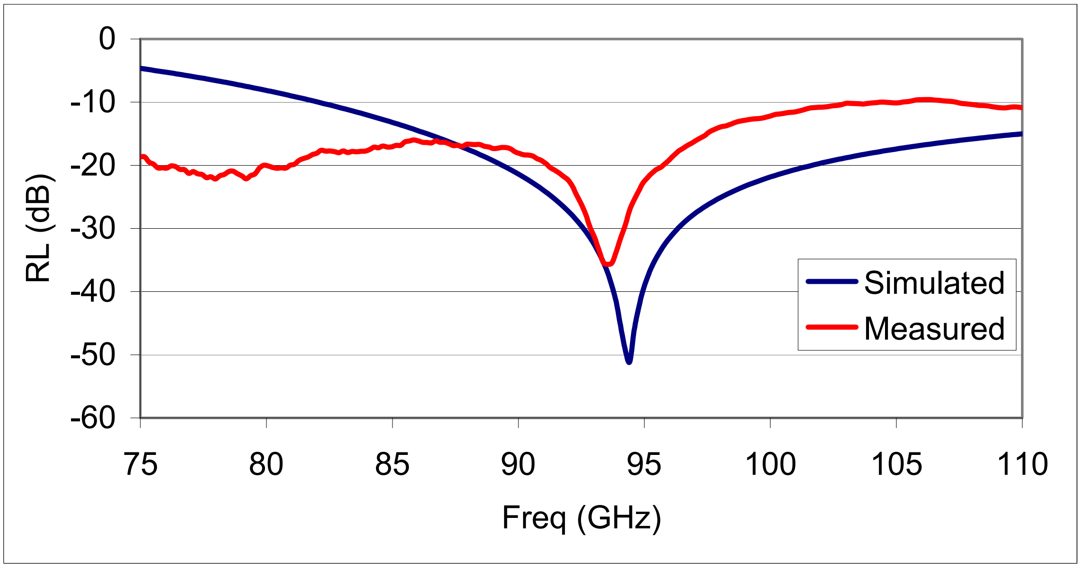

Figure 4.9: Measured vs. Simulated RL; Obtained with the CS-5 Calibration Kit.

Figure 4.10 also illustrates the measured results for the rest of the antennas, which were optimized to operate at substrate thickness of 8μm, 9μm, 10μm, 11μm, and 12μm respectively. The simulated results show that all of the measured antennas fall within the design frequency range. In addition, all of the antennas present a RL of 10dB or better over the entire *W* band frequency window. Furthermore, Figure 4.11 illustrates the mutual coupling between each antenna set. The results show that each antenna set presents at least a 35dB IL when fabricated on a 25μm high resistivity silicon membrane with a 2500μm separation between the antennas.

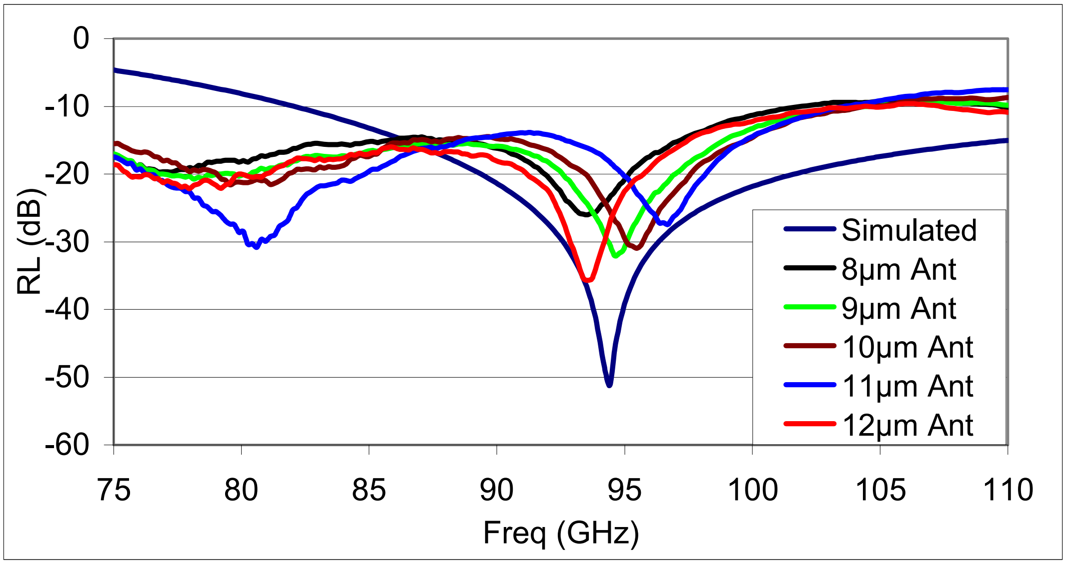

Figure 4.10: RL of the Different Slot Antennas Measured with the CS-5 Calibration Kit.

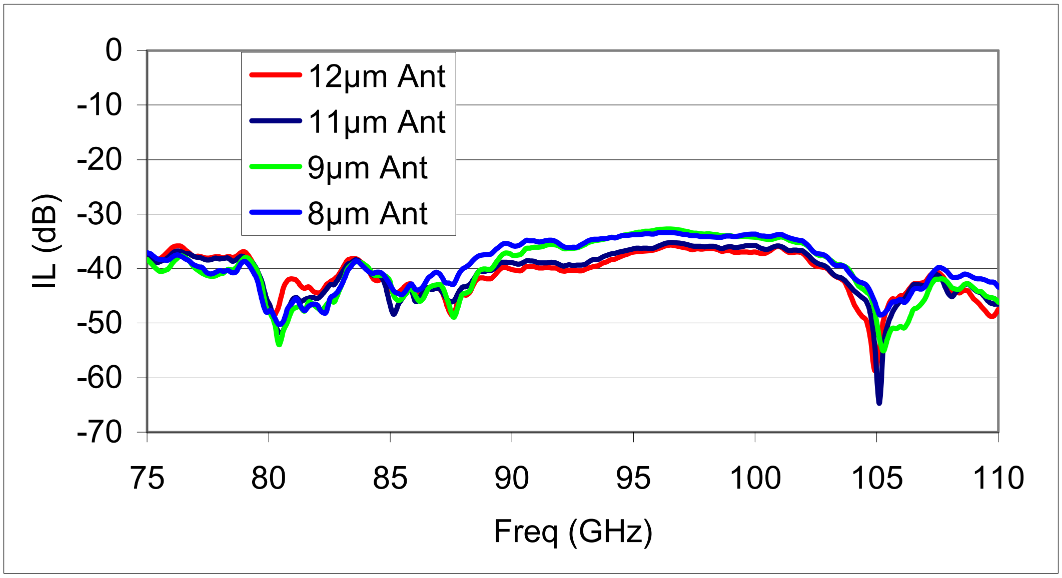

Figure 4.11: IL of the Different Slot Antennas Measured with the CS-5 Calibration Kit.

After examining the devices' performance with the CS-5 calibration kit, an on-wafer calibration was performed in order to de-embed the systematic errors that are present within the feeding line. The re-measured slot antennas with the on-wafer calibration results are presented in Figure 4.12. As expected this results closely resemble those obtained with the CS-5 calibration kit.

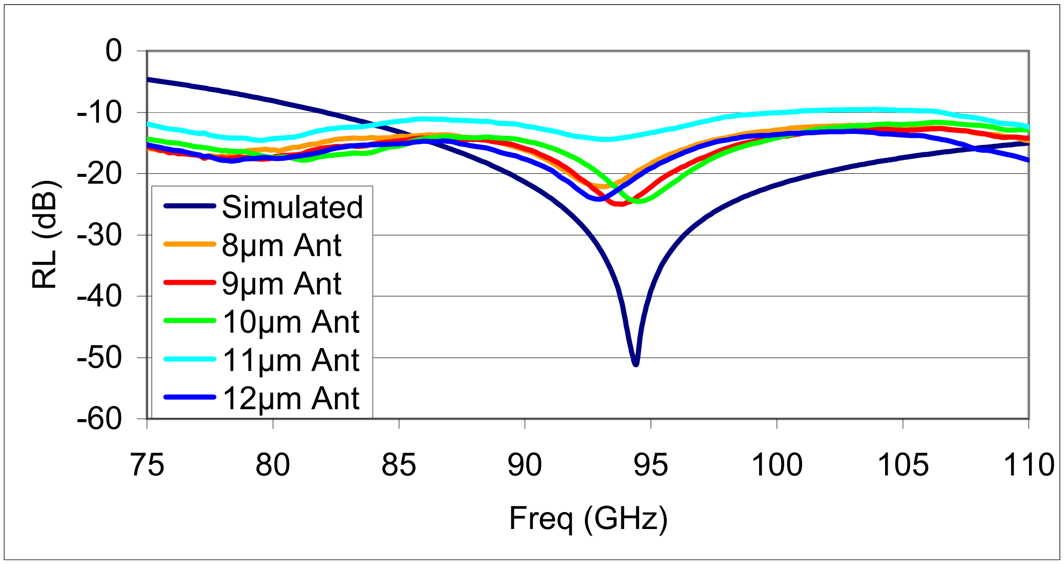

Figure 4.12: RL of the Different Slot Antennas Measured with the On-wafer Calibration Kit.

A visual of the second substrate is presented in Figure 4.13. This substrate was over-etched resulting in membranes' thicknesses ranging from a 1μm oxide layer to approximately 8μm silicon membrane.

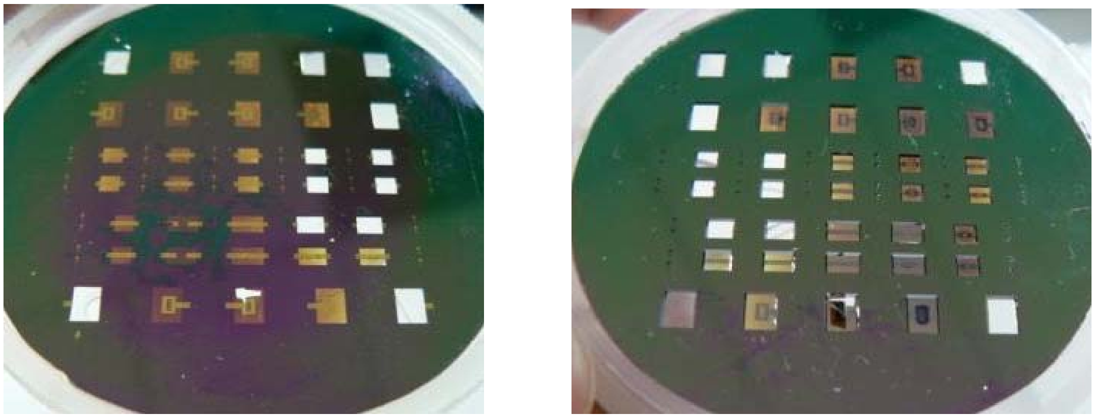

(a) (b)

Figure 4.13: (a) Top View of the Fabricated Substrate and (b) View of the Back Etched Membranes.

It should also be noted that in Figure 4.13 the silicon membranes are more transparent than the membranes presented in Figure 4.7. The transparency of the membrane is an indication of the membrane thickness. A close up of the fabricated antenna and its corresponding membrane is also presented in Figure 4.14.

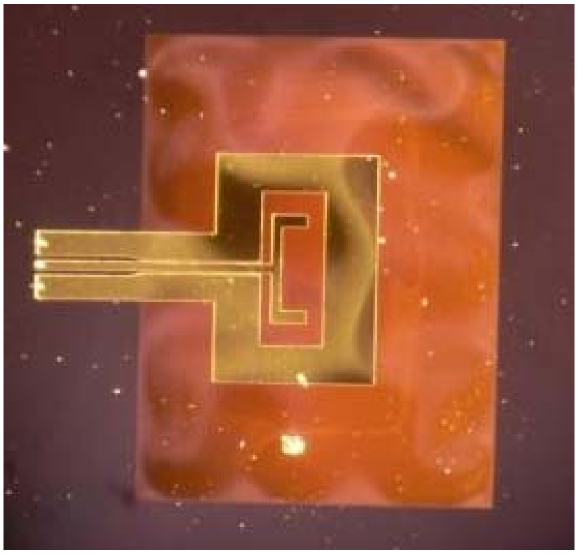

Figure 4.14: Close up of the Fabricated Slot Antenna on Top of ~ 5μm Silicon Membrane.

These antennas were also measured using both the CS-5 TRL probe tip and the on-wafer calibration method. A comparison between the simulated and measured slot antennas, both using the CS-5 and the on-wafer calibration kit are presented in Figure 4.15 and Figure 4.16 respectively. These results show that the worst case frequency shifts obtained with the CS-5 and on-wafer calibration kit were 8% and 5%, respectively. The phase of some of the measured slot antennas obtained using the on-wafer calibration is also presented in Figure 4.17.

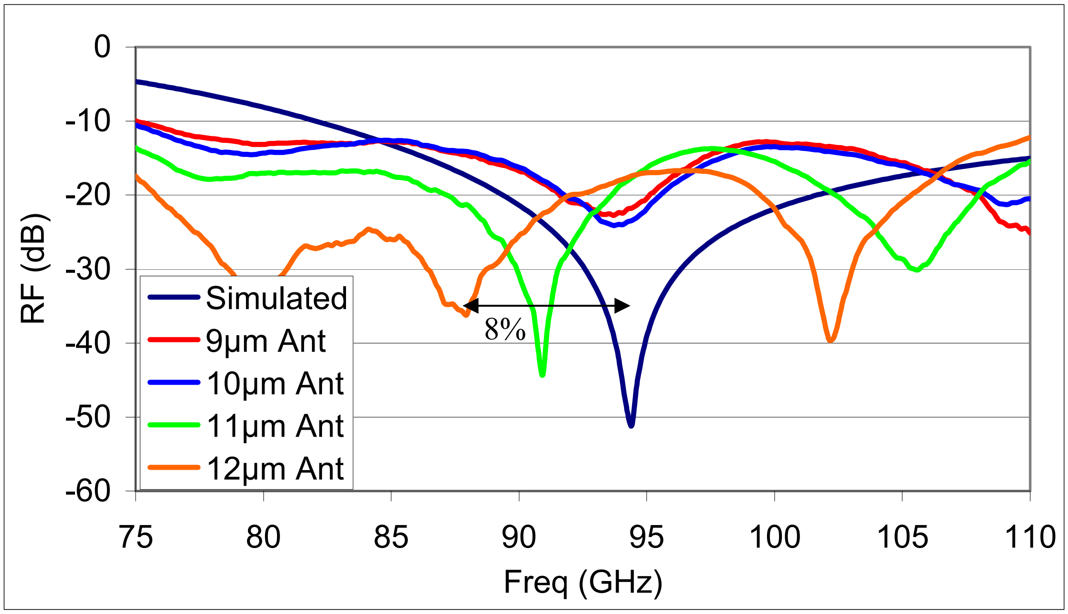

Figure 4.15: RL of the Different Slot Antennas Measured with the CS-5 Calibration Kit.

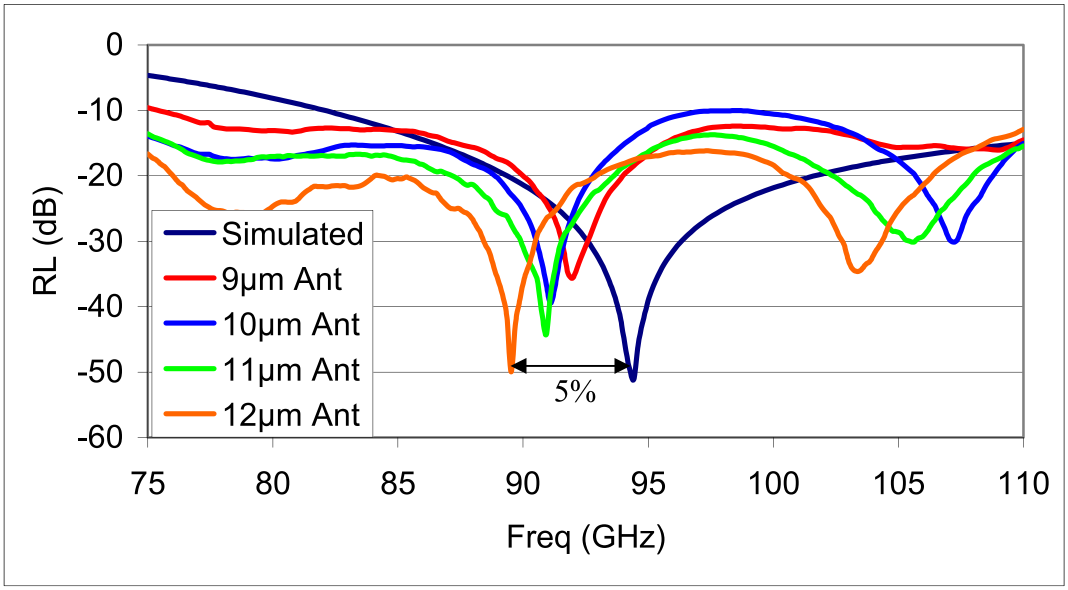

Figure 4.16: RL of the Different Slot Antennas Measured with the On-wafer Calibration.

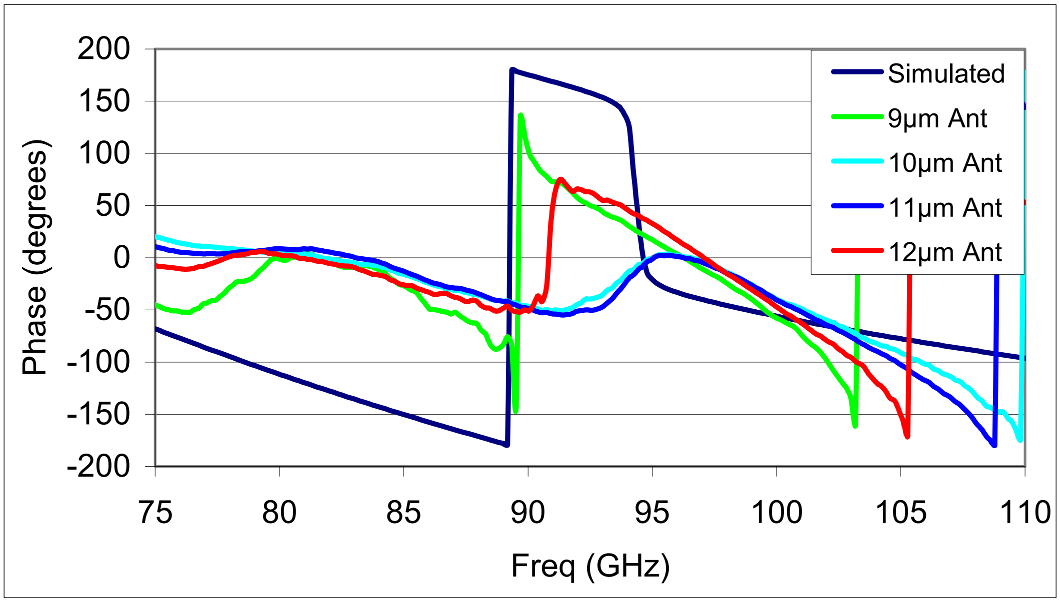

Figure 4.17: Phase of the Different Slot Antennas Measured with the On-wafer Calibration Standards.

4.4 Chapter Summary and Conclusions

This chapter provides a brief description of the millimeter wave frequency band along with some of the advantages and disadvantages that millimeter wave frequencies have over microwave, infrared, and optical frequencies. In addition, it was demonstrated through a set of Momentum simulations that the substrate thickness plays a major role on the antenna's radiation characteristics. Finally, the optimized antennas were successfully fabricated on a bulk micromachined silicon membrane using standard lithography techniques, and measured using the Wiltron 360B Network Analyzer.

The measured return loss using both calibration techniques shows that the majority of the fabricated antennas are well matched at the design frequency of 94GHz, and present at least a 10dB RL or better over the entire *W* band frequency window. The simulated radiation pattern of the 94GHz slot antenna closely resembles the radiation pattern of the 2.5GHz slot antenna described in Chapter 2. Finally, the simulated gain and directivity of the 94GHz antenna closely resembles the gain and directivity obtained with the 2.5GHz antenna. Based on these results it was concluded that the 2.5GHz antenna can be scaled up in frequency without compromising its radiation characteristics.

Chapter 5

Summary and Recommendations

5.1 Conclusions

In this thesis work, the design of two CPW-fed slot antennas, a Schottky diode detector circuit, and a CPW-to-Microstrip transition operating at 2.5GHz were presented. These low frequency devices were fabricated on an FR-4 board and tested individually to validate their performance. In addition, a low frequency Rectenna element was successfully integrated within a single FR-4 board and tested for its sensing characteristics. In the process, a set of simulations were performed to determine the dominating factors controlling the performance of each device.

It was demonstrated that an off-center feeding method of the narrow slot antenna can be utilized to decrease the high impedance of the resonant aperture and successfully match the antenna to the feeding line. The downside of this feeding technique is that it requires wire bonding in order to stabilize the ground planes of the CPW line. The failure to do so can lead to higher order modes, which are believed to be responsible for the high cross-polarization levels found in the narrow slot antenna. In order to overcome these shortcomings, a CPW-fed wide slot antenna with U-shaped tuning stubs was implemented. Since this antenna is center-fed and the ground structure of the CPW line is symmetric about its center conductor, it does not require wire bonding. This antenna provides extremely low cross-polarization, and presents the same radiation characteristic of the narrow slot antenna. Moreover, a 60% increase in bandwidth over the narrow slot antenna was observed in both simulated and measured data. The wider bandwidth response of the CPW-fed wide slot antenna is mainly dictated by the length, width, and location of the tuning stubs within the aperture. Finally, it was shown that by placing a reflector plate at the reverse side of the substrate from the antenna, with an optimum reflector plate spacing of approximately ¼λ, unidirectional radiation is achieved. The reflector plate minimizes the back radiation and concentrates that energy towards the top of the antenna, which provides approximately a 3dB improvement in the gain of the antenna.

The detector circuit of the Rectenna element was also designed, fabricated, and tested in order to study its sensing properties. It was found that the junction capacitance of the diode, the load resistor, and the matching network have a considerable effect on the output voltage and sensitivity of the detector. In addition, the filtering systems at the input and output of the detector have to be properly designed in order to prevent the higher order harmonics from re-radiating through the receiving antenna, and to isolate the input RF signal from the output DC voltage. In both measured and simulated data it was shown that the dynamic range of the detector circuit was found to be approximately from -17dBm to -50dBm, with a corresponding sensitivity of approximately 28,000mV/mW.

In order to completely integrate the low frequency prototype Rectenna element within a single FR-4 board, a via-less CPW-to-Microstrip transition was realized. It was demonstrated that the integration of the transition does not change the radiation characteristics of the antenna. This compact transition presents a well match condition at the design frequency and provides an IL better than 0.4dB over a 3.5GHz frequency span.

Finally, both of the Rectenna components were integrated within a single FR-4 board and tested for its sensing properties. It was demonstrated through a series of measurements that the fully integrated Rectenna element has the same square-law characteristics of the detector circuit. The fully integrated Rectenna is better matched at the design frequency then the separate Rectenna elements connected by M-M connector, which is responsible for the output voltage discrepancy between these two.

Once the low frequency prototypes were validated through simulated and measured data, the 2.5GHz wide slot antenna was scaled up in frequency to operate at 94GHz. A high resistivity silicon substrate was chosen for this design since it can be easily integrated with IC and CMOS technology. It was demonstrated through a set of Momentum simulations that the antenna performance heavily depends on the substrate thickness. It was shown that when the substrate thickness is comparable to the dielectric wavelength, higher order modes can be present that lead to high side lob levels and surface waves, both of which degrade the overall efficiency of the antenna. The 94GHz antenna fabricated on a 10μm silicon membrane was then optimized to provide simulated efficiencies of up to 99%. The optimized antennas were then fabricated on a bulk micromachined 10μm silicon membrane using standard lithography techniques. The measured results show that the fabricated antenna presents at least a 10dB RL over the entire *W* band frequency window. In addition, the antenna presents a well matched condition at the design frequency of 94GHz. To the best of the author's knowledge this is the first time that this specific antenna has been fabricated and tested for the *W* band frequency band.

5.2 Future Work and Recommendations

Throughout the course of this thesis work many devices were fabricated and tested, which lead to interesting conclusions and ideas for future work.

For instance, further research needs to be done in order to miniaturize the low frequency Rectenna prototype. The miniaturization of the low frequency prototype is desirable since it could reduce the cost and size of many mobile applications, but the gain and directivity of the antenna are likely to decrease as well. Thus, new miniaturization techniques are needed in order to reduce the size of the low frequency Rectenna element without degrading the overall performance of the device.

Moreover, a great deal of research still needs to be done in order to accurately complete a Rectenna element at 94GHz. First, the mutual coupling between antennas needs to be studied further. From the measurement results presented in Chapter 4, it was inconclusive if the high isolation between the two antennas is due to the etched membranes, or the distance between the antennas. In future research, a set of antennas placed at different distances from each other should be fabricated and measured to study the mutual coupling between the antennas. This is a key study needed in order to develop a high performance antenna arrays. Furthermore, the radiation pattern for the fabricated slot antenna has to be measured in order to validate the simulated radiation pattern.

Finally, a high frequency model for the Metal-Insulator-Metal (MIM) diode has to be developed in order to accurately design the detector circuit at 94GHz. The ability to scale MIM diodes up to 30THz makes it a more desirable choice when compared to the HSCH - 9161 GaAs detector diode. Additionally, the MIM diode can be fabricated within the Rectenna element using standard IC processing techniques. Lastly, an array of Rectenna elements has to be developed in order to improve the overall performance of the device. The successful completion of this research plan could lead to the next state of the art imaging, spectroscopy, or sensory systems.

References

[1] R. L. Bailey, “Journal of Engineering Power” (1972).

[2] W. C. Brown, “The History of Power Transmission by Radio Waves” Microwave Theory and Techniques, IEEE Transactions on, Vol.32, Iss.9, Sep 1984 pp: 1230-1242.

[3] J. J. Nahas, “Modeling and Computer Simulation of a Microwave-to-DC Energy Conversion Element” Microwave Theory and Techniques, IEEE Transactions on, Vol.23, Iss.12, Dec 1975, pp: 1030-1035.

[4] I. H. On, J. *S*. Rice. and D. C. Thorn, "A Theoretical Study of Microwave Beam Absorption by a Rectenna," NASA Lyndon B. Johnson Space Center, Jan 1981, NAS9- 16055.

[5] W. C. Brown, "The Receiving Antenna and Microwave Power Rectification," Journal of Microwave Power, 5, 1970, pp: 279

[6] I. J. Bahl, P. Bhartia, *Microstrip Antenna*, Artech House, Dedham, MA, 1980, Ch 6.

[7] R. Garg, P. Bhartia, I. Bahl, A. Ittipiboon, *Microstrip Antenna Design Handbook*, Artech House, Norwood, MA, 2001, Ch 7.

[8] Y. Yoshimura, **“**A Microstripline Slot Antenna,” Microwave Theory and Techniques, IEEE Transactions on, Vol.20, Iss.11, Nov 1972, pp: 760-762.

[9] Jeong Phill Kim; Wee Sang Park, **“**Network Modeling of an Inclined and Off-Center Microstrip-Fed Slot Antenna,” Antennas and Propagation, IEEE Transactions on, Vol.46, Iss.8, Aug 1998, pp: 1182-1188.

[10] D. Pozar, **“**A Reciprocity Method of Analysis for Printed Slot and Slot-Coupled Microstrip Antennas**”**Antennas and Propagation, IEEE Transactions on [legacy, pre -1988], Vol.34, Iss.12, Dec 1986, pp: 1439-1446.

[11] H. G. Booker, “Slot Aerials and Their Relation to Complementary Wire Aerials (Babinets’ Principle),” J. I. E.E., Vol.IIIA, 1946, pp: 620-226.

[12] S. Sierra-Garcia, J. J. Laurin, “Study of a CPW Inductively Coupled Slot Antenna” Antennas and Propagation, IEEE Transactions on, Vol.47, Iss.1, Jan 1999, pp: 58-64.

[13] Constantine A. Balanis, *Antenna Theory Analysis and Design,* 3rd ed., John Wiley & Sons, Inc., Hoboken, New Jersey, 2005.

[14] Warren L. Stutzman and Gary A. Thiele, *Antenna Theory and Design*, John Wiley & Sons, Inc., New York, 1981.

[15] Jyh-Ying Chiou; Jia-Yi Sze; Kin-Lu Wong “A Broad-Band CPW-fed Strip-Loaded Square Slot Antenna” Antennas and Propagation, IEEE Transactions on, Vol.51, Iss.4, April 2003, pp: 719-721.

[16] X. Ding, A.F. Jacob, “CPW-fed Slot Antenna with Wide Radiating Apertures” Microwaves, Antennas and Propagation, IEEE Proceedings -, Vol.145, Iss.1, Feb 1998, pp: 104-108.

[17] Horng-Dean Chen “Broadband CPW-fed Square Slot Antennas with a Widened Tuning Stub” Antennas and Propagation, IEEE Transactions on, Vol.51, Iss.8, Aug 2003, pp: 1982-1986.

[18] R. Chair, A. A. Kishk, K. F. Lee, C. E. Smith, and D. Kajfez, “Microstrip Line and CPW-fed Ultra Wideband Slot Antennas with U-shaped Tuning Stub and Reflector,” Progress In Electromagnetics Research, PIER 56, 2006, pp: 163-182.

[19] Stephen A. Maas, *The RF and Microwave Circuit Design Cookbook,* Artech House, Inc., Norwood, MA, 1998, Ch 5.

[20] Avago Technologies Data Sheet, “Surface Mount Zero Bias Schottky Detector Diodes”, HSMS-285X Series. Copyright © 2006 Avago Technologies, Limited.

[21] David M. Pozar, *Microwave Engineering,* 3rd ed., John Wiley & Sons, Inc., Hoboken, New Jersey, 2005, Ch 10.

[22] Agilent Technologies Application Note 969, “The Zero Bias Schottky Detector Diode”, HSMS-285X Series. Copyright © 1999 Agilent Technologies, Inc.

[23] Guillermo Gonzalez, *Microwave Transistor Amplifiers Analysis and Design*, 2nd ed., Prentice-Hall, Inc., Upper Saddle River, New Jersey, 1997, Ch 2.

[24] P. Bhartia, I. J. Bahl, *Millimeter Wave Engineering and Applications,* John Wiley & Sons, Inc., New York, NY, 1984.

[25] http://www.phys.hawaii.edu/~anita/web/paperwork/currently%20organizing/Military%20EW%20.

[26] L. R. Wicker, and D. C. Webb, “The Potential Military Application of Millimeter Waves,” AGARD *Conf. Proc.*, CP 225, on Millimeter and Submillimeter Wave Propagation and Circuits, 1978, pp: 11-16.

[27] J. F. Luy, K.M. Strohm, J. Buechler, P. Russer, "Silicon Monolithic Millimetre-Wave Integrated Circuits," Microwaves, Antennas and Propagation, IEEE Proceedings H , Vol.139, no.3, , Jun 1992 ,pp: 209-216.

[28] P. Russer, "Si and SiGe Millimeterwave Integrated Circuits for Sensor and Communications Applications," Microwaves and Radar, 1998. MIKON '98., 12th International Conference on , Vol.4, pp: 330-344 Vol.4, May 1998, pp: 20-22.

[29] G. P. Gauthier, J. P. Raskin, L. P. B. Katehi, G. M. Rebeiz, "A 94-GHz Aperture-Coupled Micromachined Microstrip Antenna," Antennas and Propagation, IEEE Transactions on , Vol.47, no.12, Dec 1999, pp: 1761-1766.

[30] http://cp.literature.agilent.com/litweb/pdf/5091-3645E.pdf.

Appendices

Appendix A: 2.5GHz Rectenna Elements Measurements' Setup

The reflection coefficient (S11) of the Rectenna elements was obtained using the measurement setup presented in Figure A.1. The reflection coefficient measurement is a one-port measurement in which only P_1 of the RF Vector Network Analyzer (VNA) has to be calibrated. The accuracy of the measured reflection coefficient is determined by the precision of the standards utilized in the error correction processes, which is widely known as the calibration standards. In this measurement, a set of pre-determined calibration standards consisting of an open, short, and load (SOL) were utilized during the calibration process. See Appendix B for calibrated results.

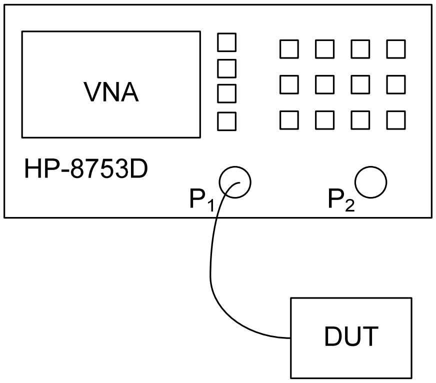

Figure A.1: Block Diagram for One-Port S-parameter Measurements.

In order to obtain both reflection and transmission coefficients of a given device under test (DUT) a full two-port calibration is required in order to de-embed the systematic errors from the measurements. A block diagram of the full two-port calibration setup is presented in Figure A.2. This calibration technique is very similar to the SOL calibration presented above. The only difference is that it requires one more known standard in order to complete the error model. This calibration technique, known as the SOLT calibration, consists of measuring a short, open, load, and thru standards.

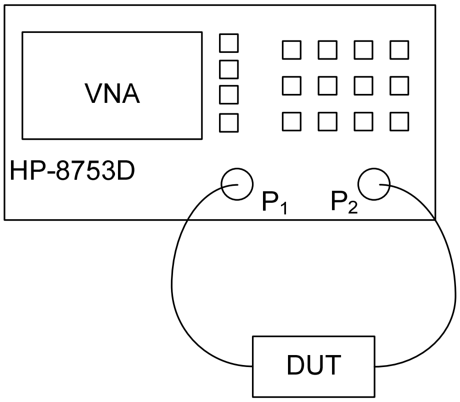

Figure A.2: Block Diagram of a Full Two-Port S-parameter Measurements.

The radiation pattern of the 2.5GHz slot antenna was measured using the measurement setup presented in Figure A.3. Here, the source is used to set the transmitting RF power at a pre-determined power level. Then, the DAM's computer tool controls the turn table, which rotates the receiving antenna in the azimuth and elevation direction. At each angle the pattern recorder saves the transmission coefficient (S21) value until the azymuthal angle reaches 360º.

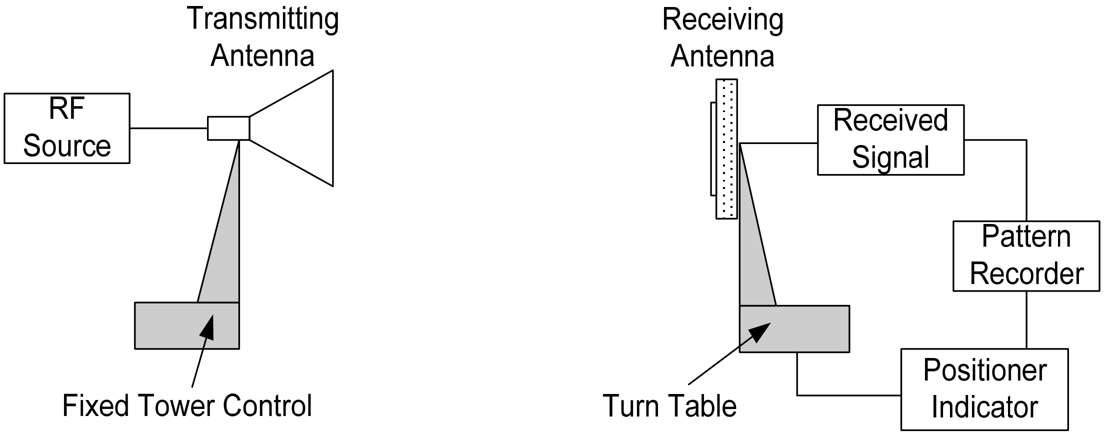

Figure A.3: Typical Block Diagram for Antenna Range Measurements.

The 2.5GHz detector circuit square-law and sensitivity measurements were performed using the measurement setup presented in Figure A.4. Here, the VNA acts as the RF source, and the digital multimeter is used to measure the rectified output voltage. The power meter is calibrated prior to making the measurement, and it is utilized to measure the actual power available from the source. The variable step attenuator is than varied and the corresponding DC voltage at the output of the detector circuit is recorded.

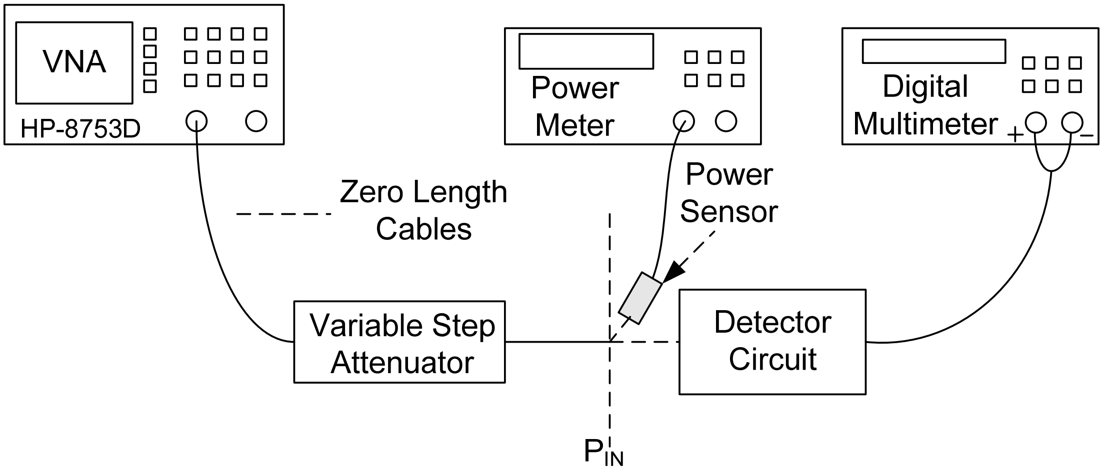

Figure A.4: Square-law Detector Block Diagram Measurement Setup.

The block diagram presented in Figure A.5 was utilized to measure the sensing properties of the fully integrated 2.5GHz Rectenna element. This measurement setup closely resembles that of the square-law detector, with some added features. The power amplifier is needed to increase the power incident to the transmitting antenna. The power meter is responsible for accurately reading the power available at the output of the step attenuator, and the digital multimeter reads the output DC voltage delivered by the Rectenna element. The transmitting antenna and the Rectenna element must be aligned to reduce any polarization losses. Finally, the input power to the transmitting antenna and the output DC voltage are recorded as a function of attenuation setting. The recorded data for the fully integrated Rectenna element and the individual Rectenna elements connected by a M-M connector are presented at the end of this Appendix.

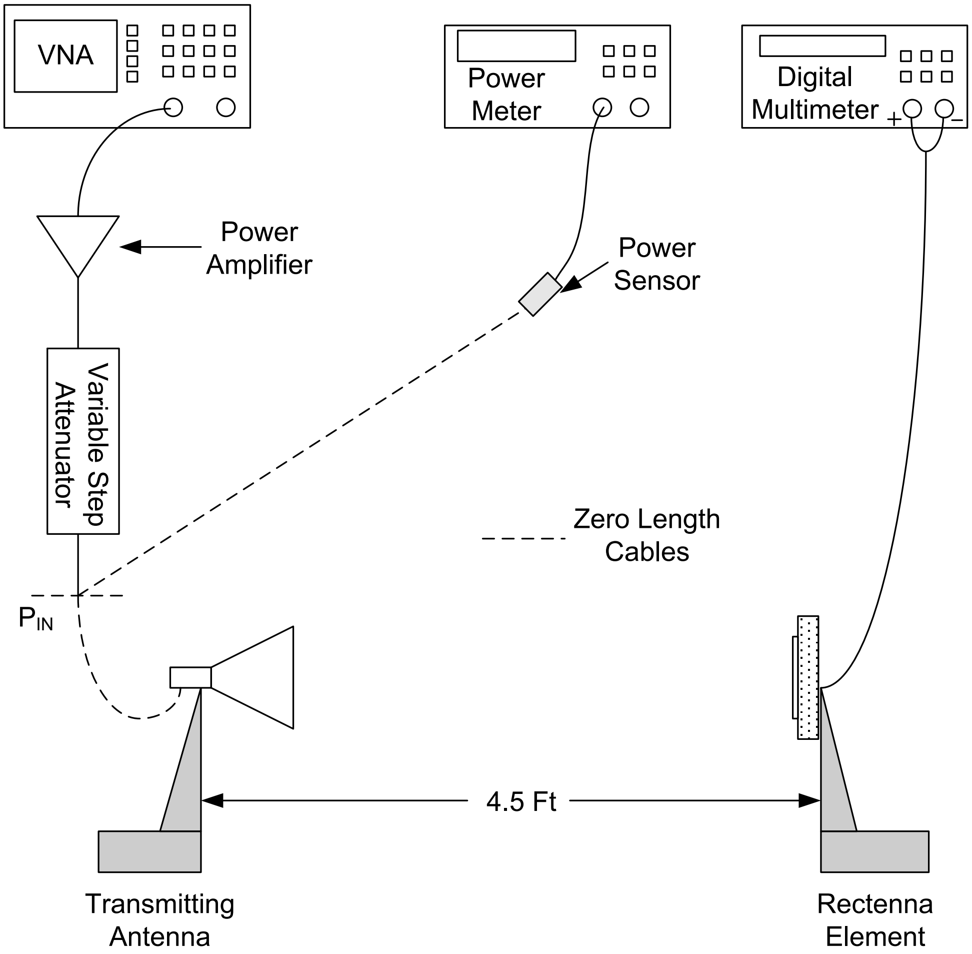

Figure A.5: Block Diagram for the Integrated Rectenna Element Power Measurements.

Table A.1: Recorded Data for the Rectenna Elements Connected by a M-M Barrel.

Attenuator Setting	Transmitting Antenna P_{IN} (dBm)	Receiving Antenna P_R (dBm)	Rectenna Output V_{DC} (mV)
0	22.93	-2.94	1175.5
2	21.1	-4.63	960.3
4	19.19	-6.54	776.96
6	17.12	-8.61	610.00
8	15.09	-10.64	476.85
10	12.78	-12.95	352.20
12	10.76	-14.97	270.50
14	8.84	-16.89	205.60
16	6.87	-18.86	150.70
18	4.91	-20.82	110.80
20	2.87	-22.86	80.59
22	0.89	-2484	57.25
24	-1.05	-26.78	39.96
26	-3.06	-28.78	27.18
28	-5.03	-30.86	18.19
30	-7.13	-32.86	11.68
32	-9.13	-34.86	7.64
34	-11.09	-36.82	5.0
36	-13.08	-38.81	3.25
38	-15.06	-40.79	2.14
40	-17.07	-42.80	1.42
42	-19.09	-44.82	0.95
44	-21.08	-46.81	0.65
46	-23.12	-48.85	0.45
48	-25.16	-50.89	0.3
50	-27.34	-53.07	0.21

Table A.2: Recorded Data for the Fully Integrated Rectenna Element.

Attenuator Setting	Transmitting Antenna P_{IN} (dBm)	Receiving Antenna P_R (dBm)	Rectenna Output V_{DC} (mV)
0	22.95	-2.92	1250.7
2	21.13	-4.60	1023.2
4	19.24	-6.49	826.98
6	17.17	-8.56	652.67
8	15.12	-10.61	513.89
10	12.88	-12.85	388.89
12	10.97	-14.76	298.50
14	9.00	-16.73	229.17
16	6.98	-18.75	173.04
18	4.99	-20.74	129.60
20	2.88	-22.85	93.99
22	0.89	-24.84	67.96
24	-1.07	-26.80	48.47
26	-3.08	-28.81	33.53
28	-5.07	-30.80	22.83
30	-7.17	-32.90	14.86
32	-9.19	-34.92	9.81
34	-11.16	-36.89	6.47
36	-13.15	-38.88	4.22
38	-15.14	-40.87	2.78
40	-17.15	-42.88	1.85
42	-19.17	-44.90	1.26
44	-21.15	-46.88	0.84
46	-23.18	-48.91	0.58
48	-25.20	-50.93	0.41
50	-27.36	-53.09	0.28

Appendix B: Low Frequency Calibration Standards and Results

In Chapter 3, the CPW-to-Microstrip transition results show a significant amount of ripple, which in some cases degrades the IL (S21) of the device. The origin of these errors mainly comes from the calibration process in which the cable movement, SMA connector, and transition from one medium to another (coaxial to CPW) have a significant effect. The cable movement changes the phase of the calibrated data and adds uncertainties to the calibration correction process. In addition, the transition from coaxial line to CPW and microstrip line represents discontinuities, which further contribute to the ripple effect present in the measured IL of the CPW-to-Microstrip transition. The calibration results for the 2.5GHz antennas, detector circuit, and CPW-to-Microstrip transition S-parameter measurements are presented below. It should be mentioned that these results were obtained using the HP-8753D network analyzer.

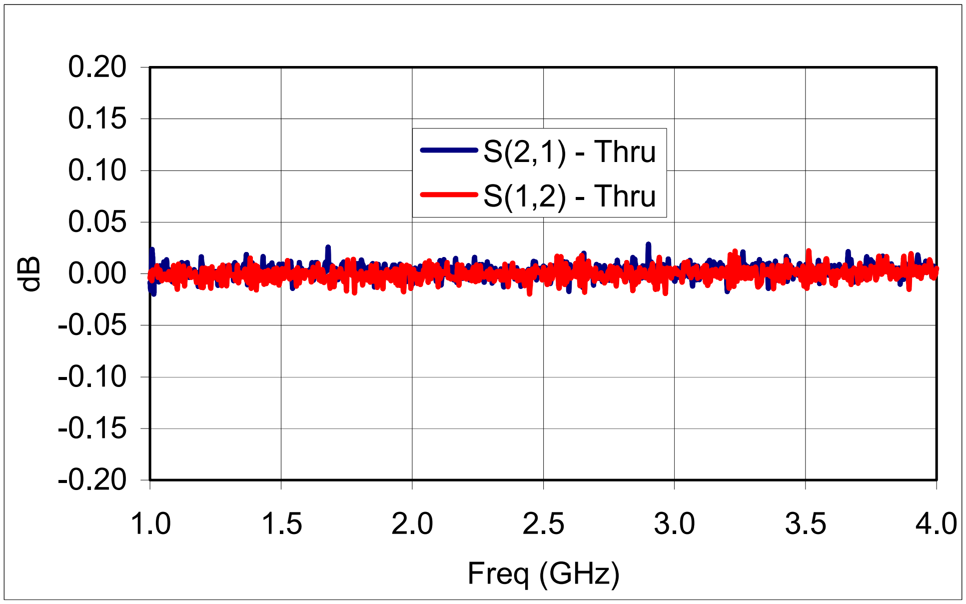

Figure B.1: IL of the SOLT Thru Standard.

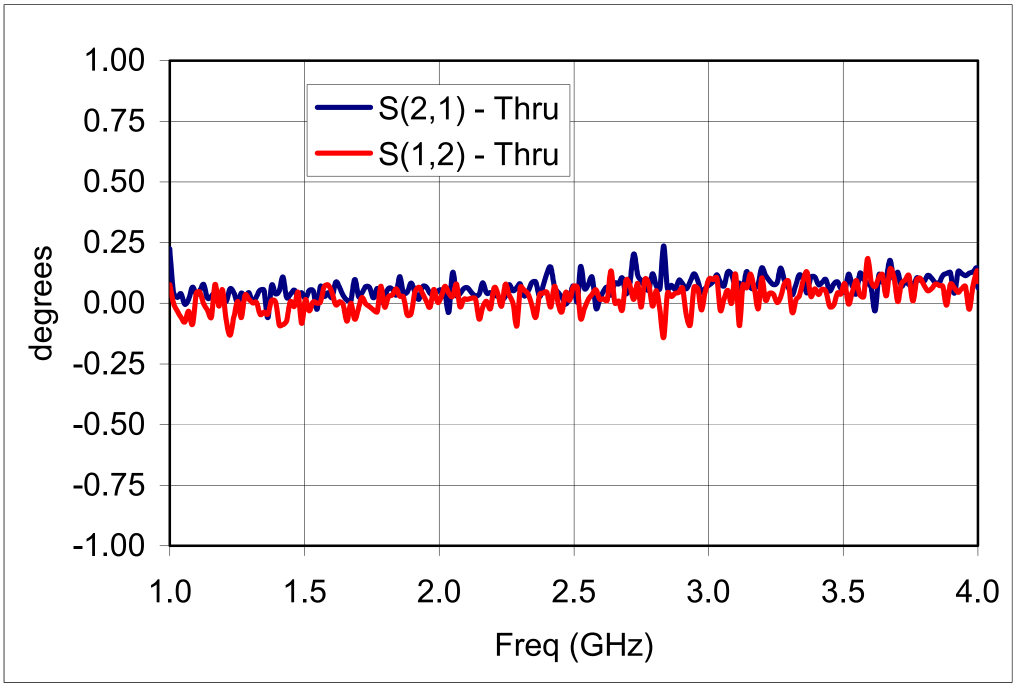

Figure B.2: Phase Response of the SOLT Thru Standard.

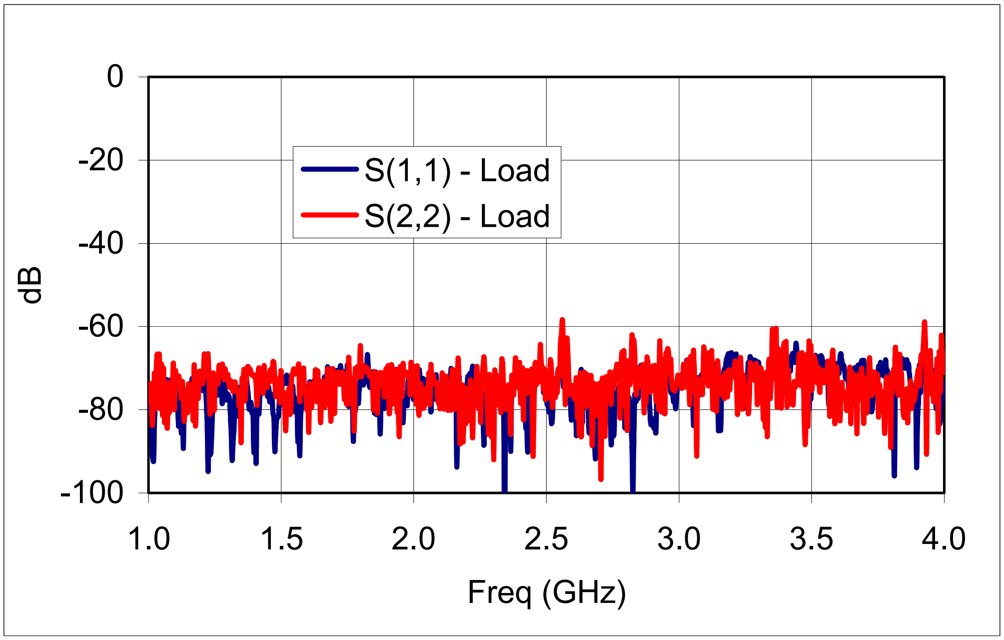

Figure B.3: RL of the SOLT Load Standard.

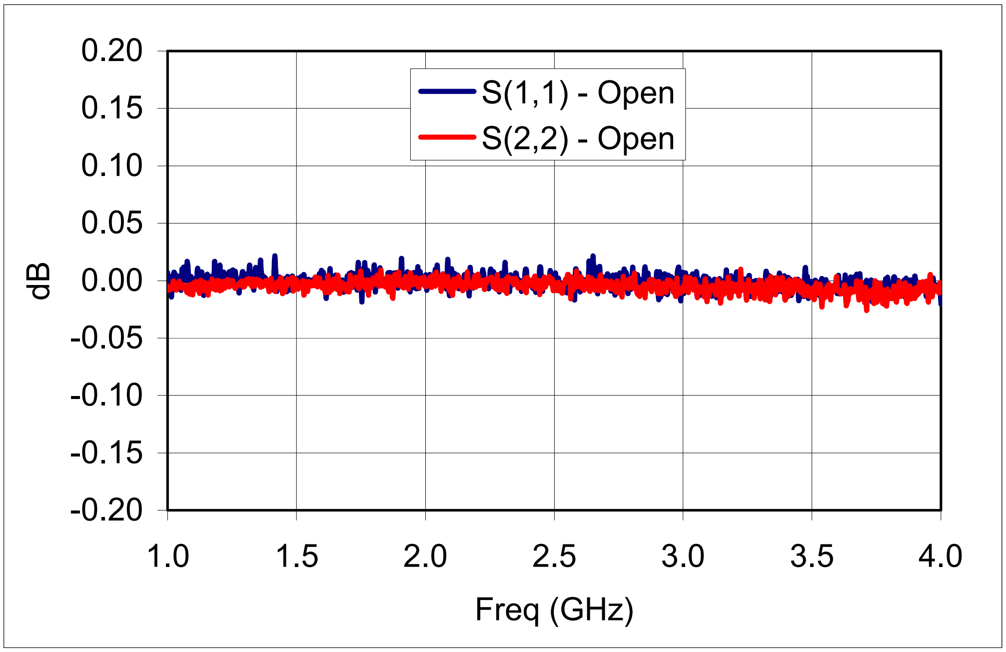

Figure B.4: RL of the SOLT Open Standard.

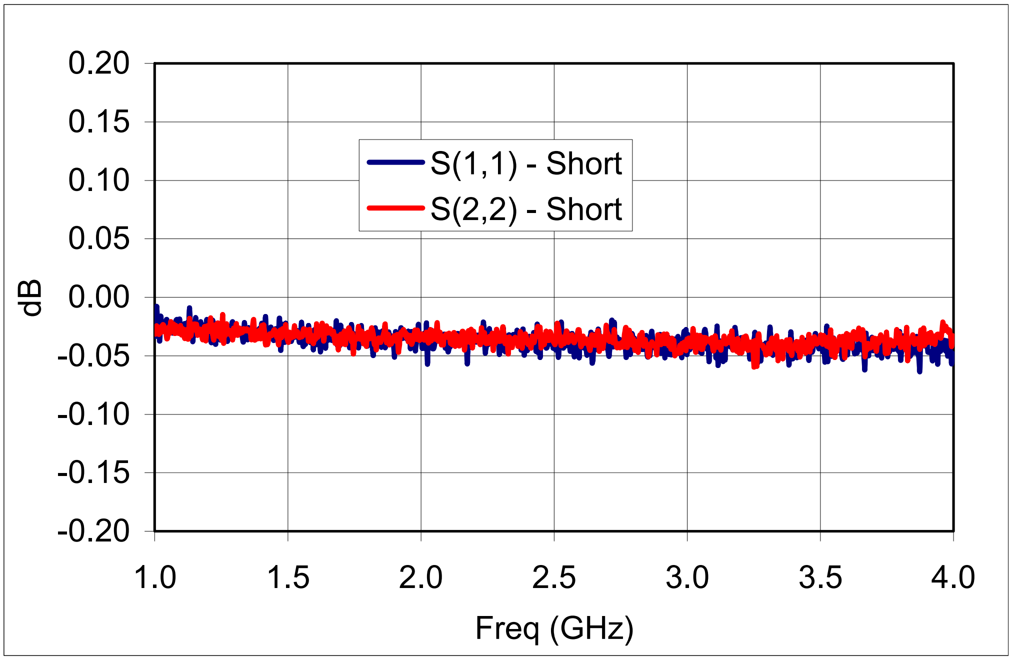

Figure B.5: RL of the SOLT Short Standard.

As mentioned before a Thru-Reflect-Line (TRL) calibration kit was designed in order to measure the actual input impedance of the detector circuit. The advantage of this type of calibration is that it takes into account the SMA connector losses, and gives an extra degree of freedom, which allows one to control the measurements' reference plane. As depicted in Figure B.6, the length of the thru standard is arbitrarily chosen, and it sets the reference plane of the measurement. The length of the open is ½ of the thru standard, and the length of the delay is chosen to be ¼λ at the design frequency of 2.5GHz. The useable bandwidth of a single delay line is limited to an 8:1 (frequency span /start frequency) ratio. If a larger frequency range is needed, multiple line pairs with the same characteristic impedance can be utilized. It should be mentioned that the frequency span of each delay line should overlap with one another.

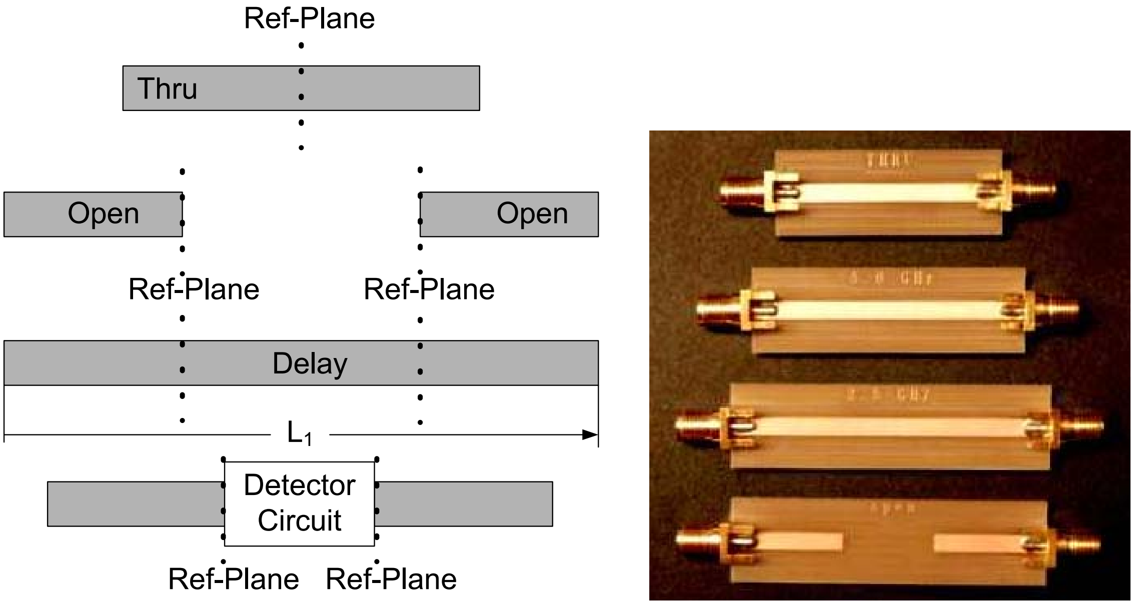

(a) (b)

Figure B.6: (a) Drawing of a Given TRL Standard Kit and Reference Plane. (b) Visual of the Fabricated TRL Standards.

The key terms and formulas needed to calculate the TRL standard definitions are presented bellow. It should be mentioned that the thru and reflect standards' delays were defined to be zero picoseconds.

$L_1 = L_{THRU} + L_{2.5GHz\_DELAY}$ $\quad L_{OPEN} = \frac{L_{THRU}}{2}$ $\quad \varepsilon_{\text{eff}} = 3.29$

$L_{THRU} = 4$ cm $\quad L_{OPEN} = 2$ cm $\quad L_{2.5GHz\_DELAY} = 1.6531$ cm

$$v_p = \frac{c}{\sqrt{\varepsilon_{eff}}} = 1.653x10^8 \frac{m}{s} = 1.653x10^{10} \frac{cm}{s}$$

$$T_{2.5GHz\_DELAY} = \frac{L_{2.5GHz-DELAY}}{v_p} = 99.8ps$$

$$T_{5GHz\_DELAY} = \frac{L_{5GHz\_DELAY}}{v_p} = 49.42ps$$

Finally, after calculating the standard definitions, a TRL calibration kit was fabricated by on a FR-4 board and implemented for error correction using the HP-8753D VNA. The calibration results are presented below.

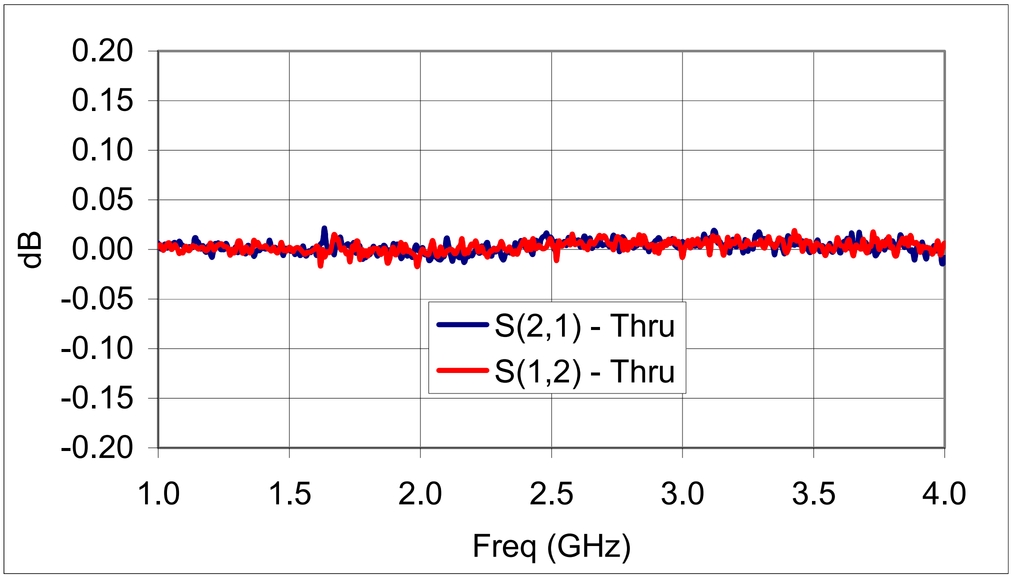

Figure B.7: IL of the TRL Thru Standard.

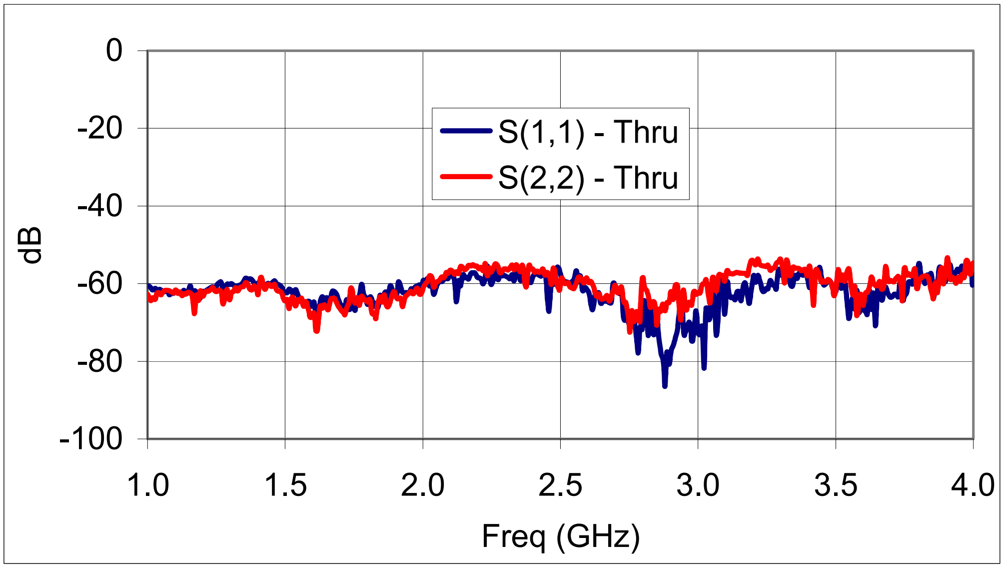

Figure B.8: RL of the TRL Thru Standard.

Appendix B (Continued)

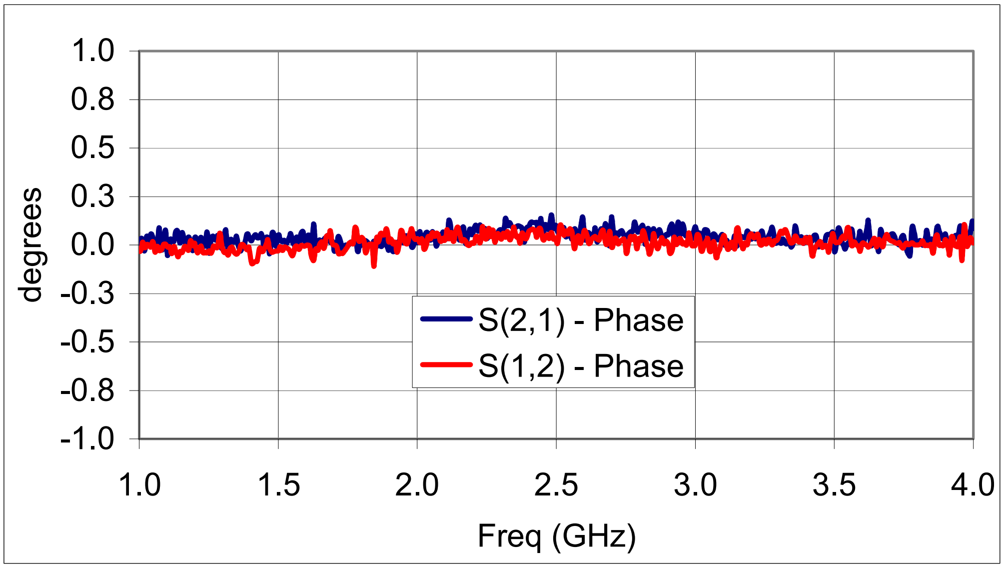

Figure B.9: Phase of the TRL Thru Standard.

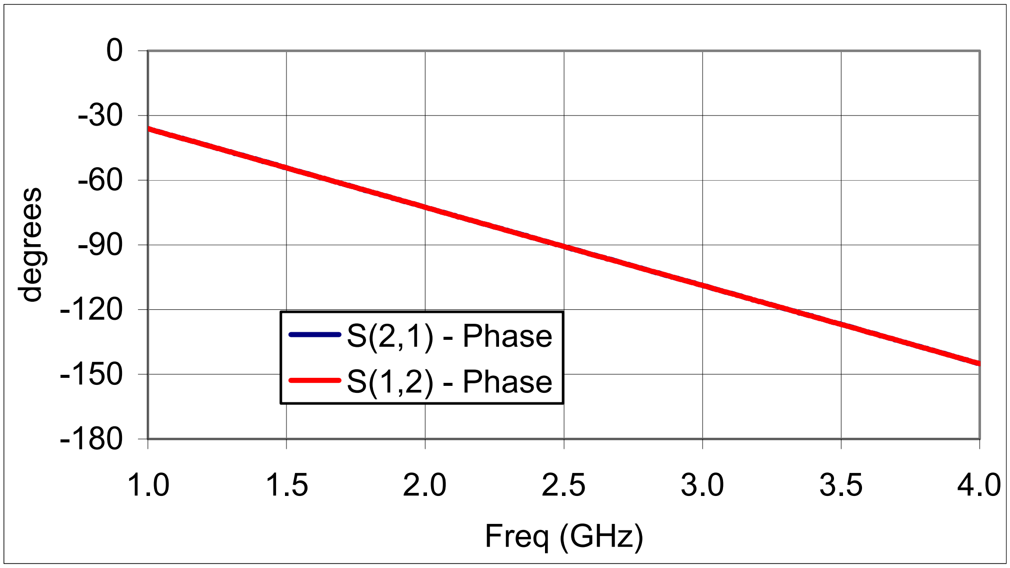

Figure B.10: Phase of the TRL Delay Standard.

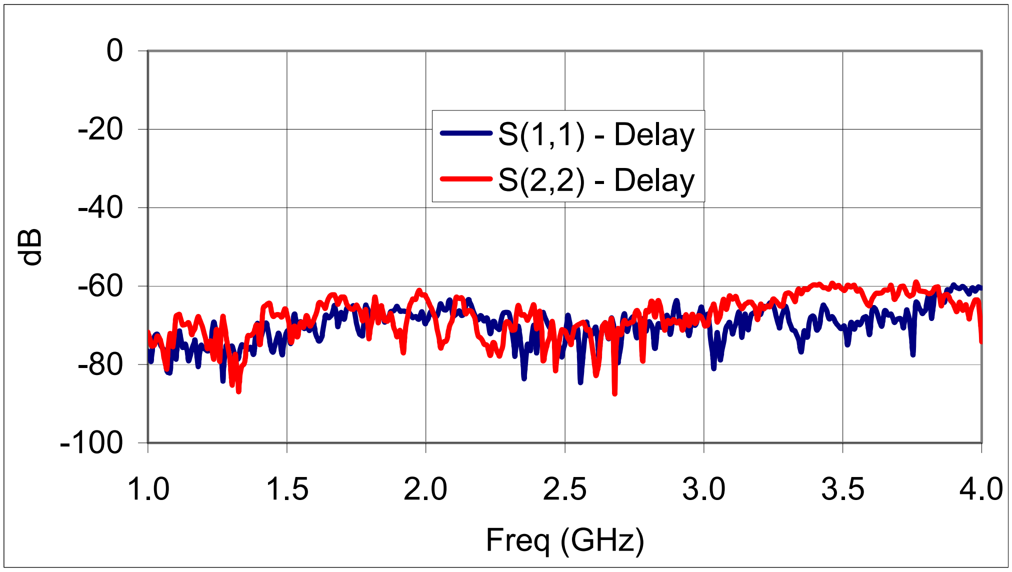

Figure B.11: RL of the TRL Delay Standard.

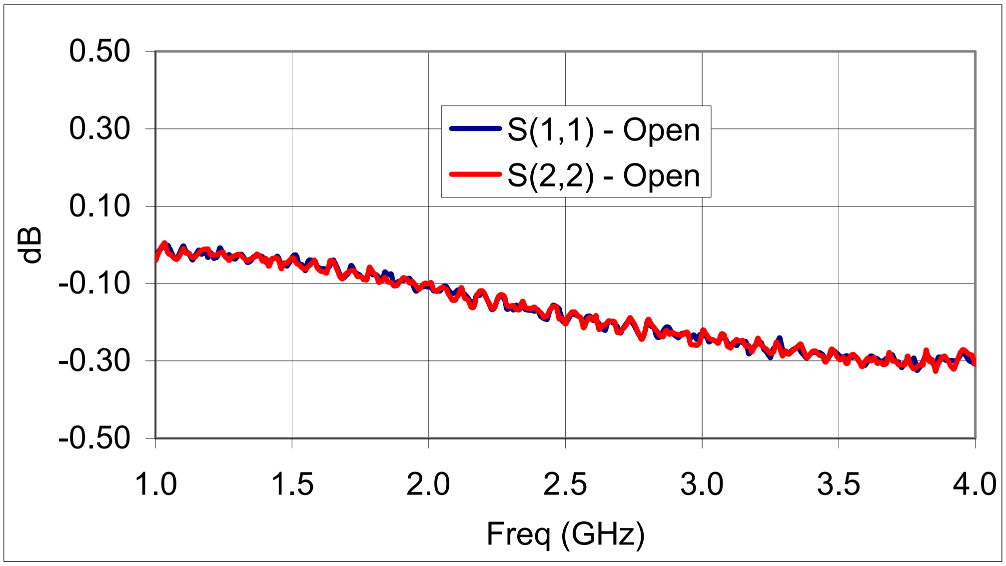

Figure B.12: RL of the TRL Open Standard.

Appendix C: *W* band Calibration Standard Results

The *W* band measurements were performed using the Wiltron 360B Network Analyzer along with the Wiltron SM5184 transmission and reflection modules. As the name implies the transmission and reflection modules expands the frequency range of the network analyzer to the 65GHz - 110GHz *W* band frequency window, and performs transmission and reflection measurements. A visual of the measurement setup is illustrated in Figure C.1.

Figure C.1: Visual of the *W* band Measurement Setup.

For the *W* band antenna measurements two type of calibrations were performed in order to remove the systematic errors from measured data. First, the system was calibrated using the CS-5 calibration kit. With this calibration kit a TRL calibration was performed. Then the reference plane was shifted in order to obtain a probe tip calibration. The corrected calibrated results are depicted below.

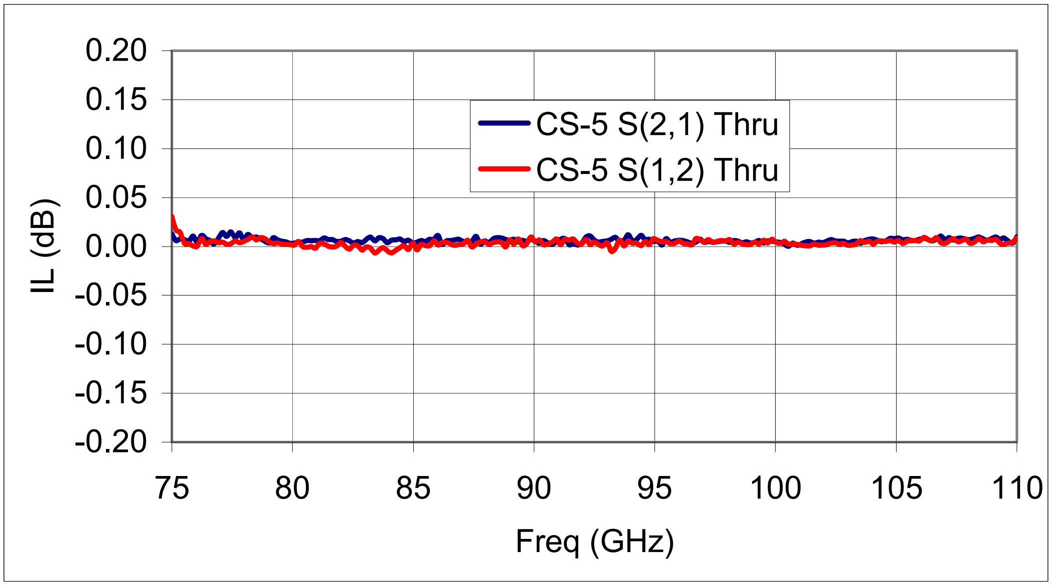

Figure C.2: IL of the CS-5 Thru Standard (After Reference Plane Shift to Probe Tips).

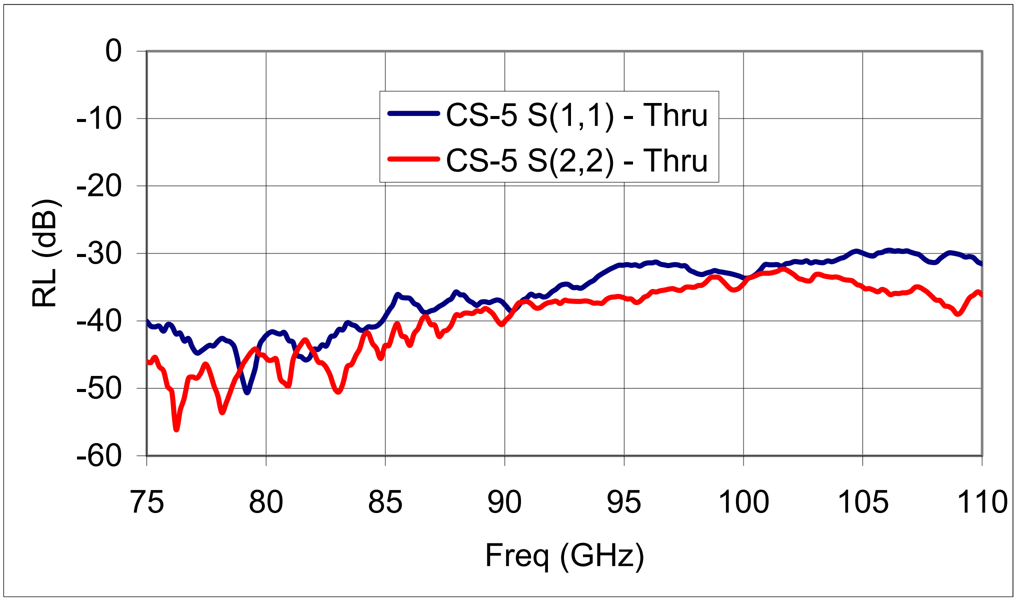

Figure C.3: RL of the CS-5 Thru Standard (After Reference Plane Shift to Probe Tips).

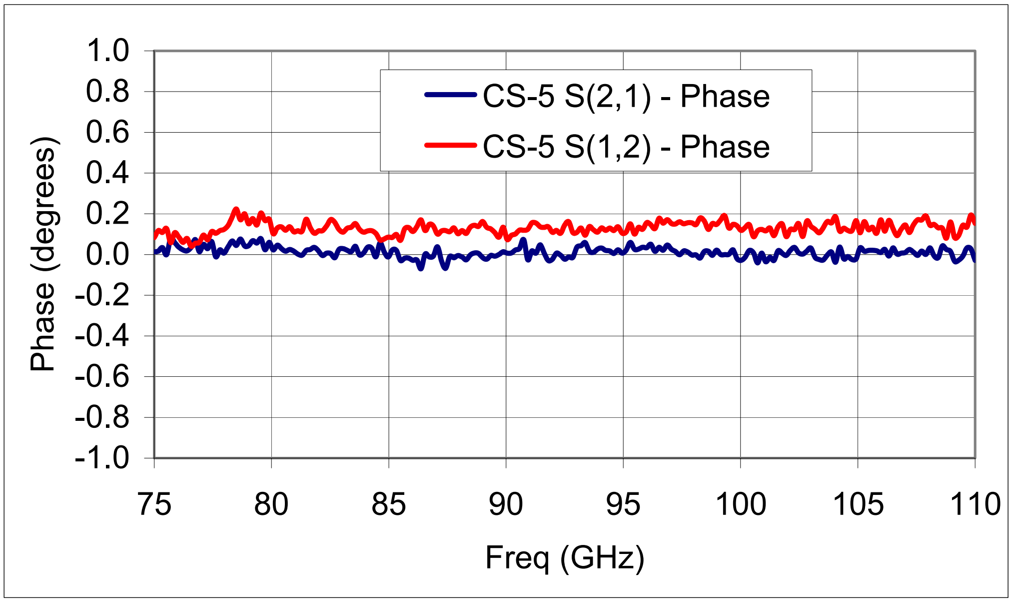

Figure C.4: Phase of the TRL Thru Standard (After Reference Plane Shift to Probe Tips).

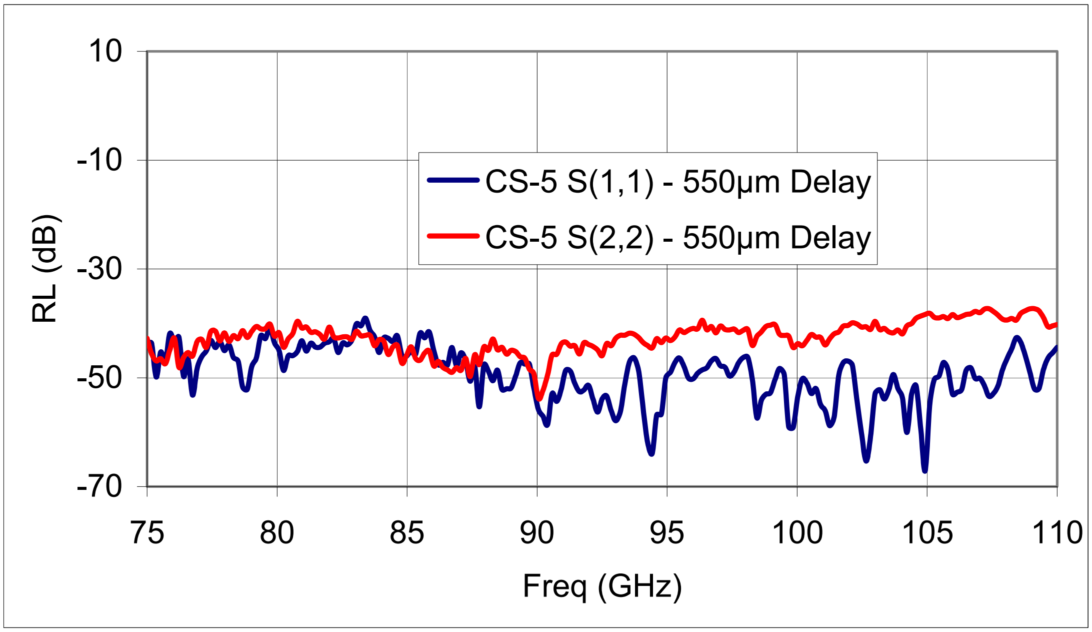

Figure C.5: RL of the CS-5 550µm Delay Standard (After Reference Plane Shift to Probe Tips).

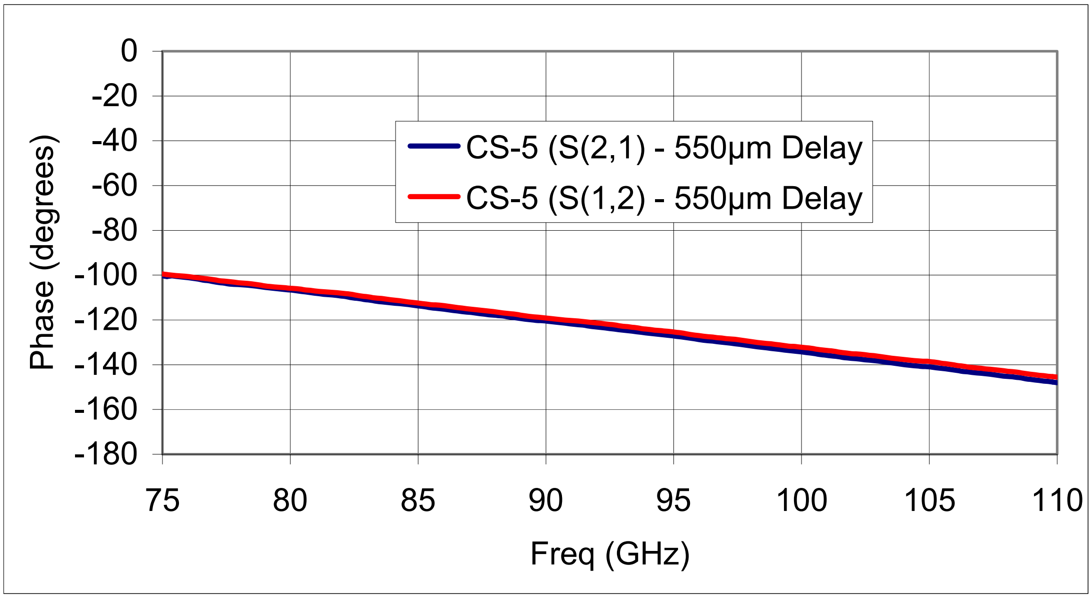

Figure C.6: Phase of the CS-5 550µm Delay Standard (After Reference Plane Shift to Probe Tips).

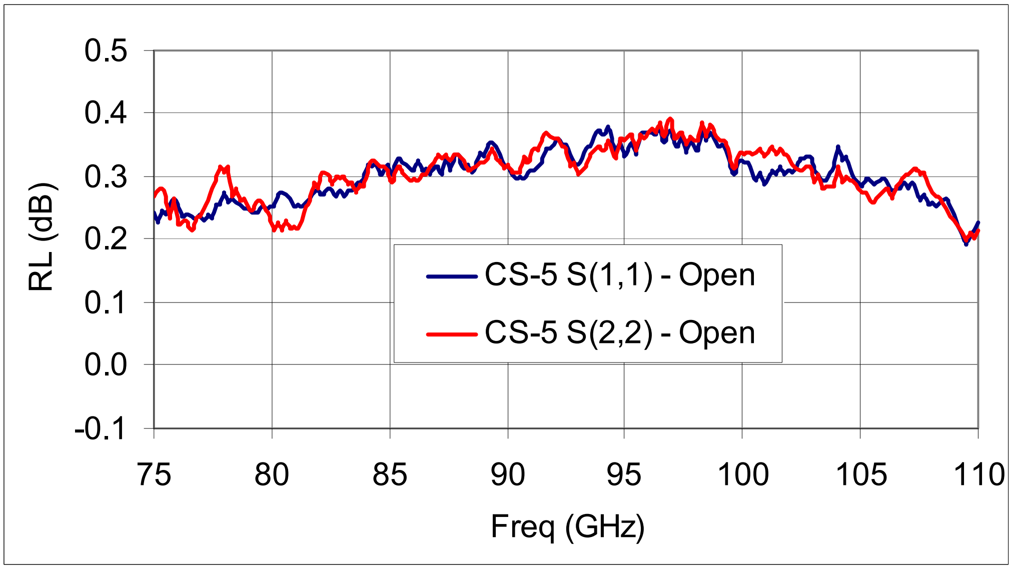

Figure C.7: RL of the CS-5 Open Standard (After Reference Plane Shift to Probe Tips).

Appendix C (Continued)

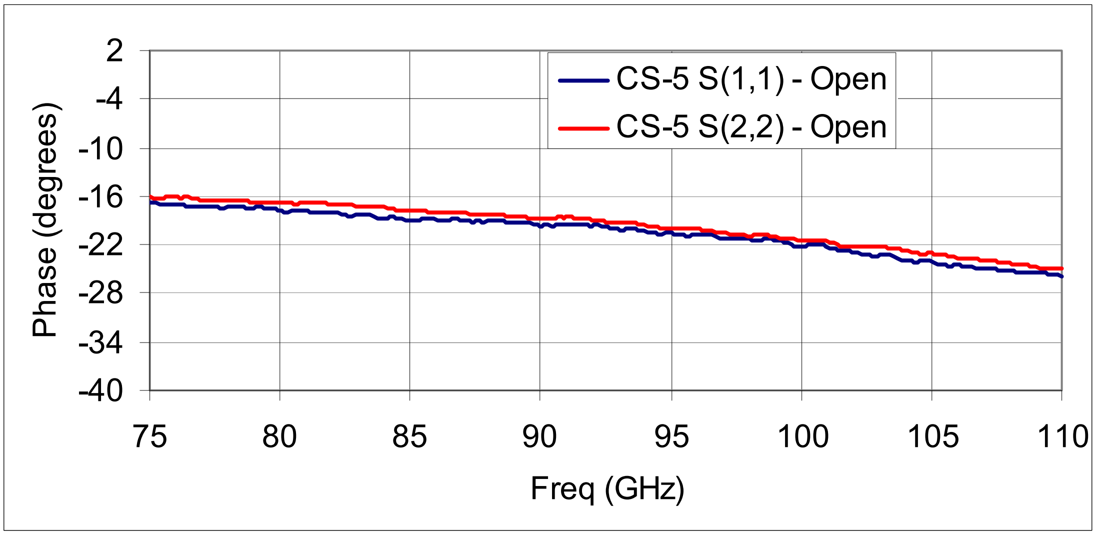

Figure C.8: Phase of the CS-5 Open Standard (After Reference Plane Shift to Probe Tips).

After obtaining the antenna measurements with the probe tip calibration, an on-wafer calibration was performed in order to de-embed the systematic errors that are present within the feeding line. A drawing of the calibration standards utilized for this measurements along with the calibration results are presented Figure C.8.

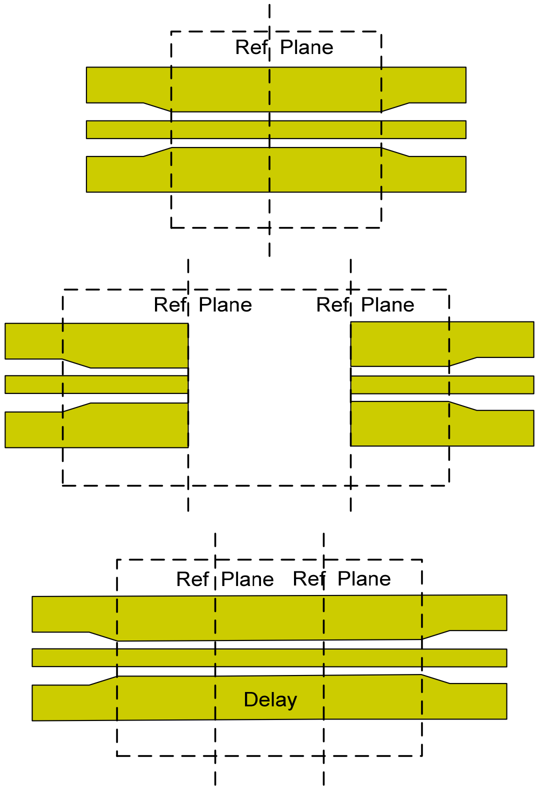

Figure C.9: Drawing of the On-wafer Calibration Standards.

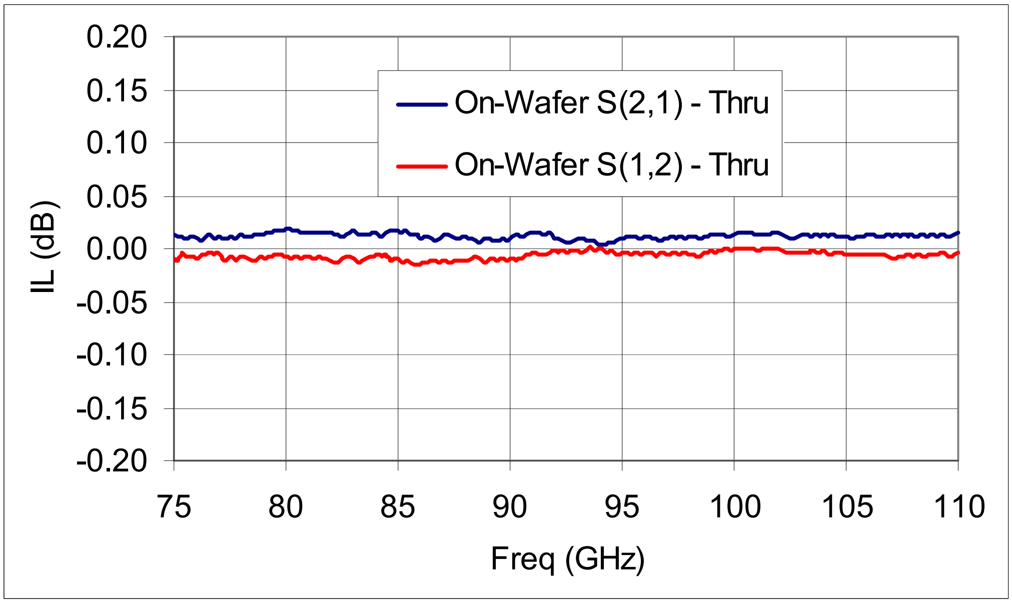

Figure C.10: IL of the On-wafer Thru Standard.

Appendix C (Continued)

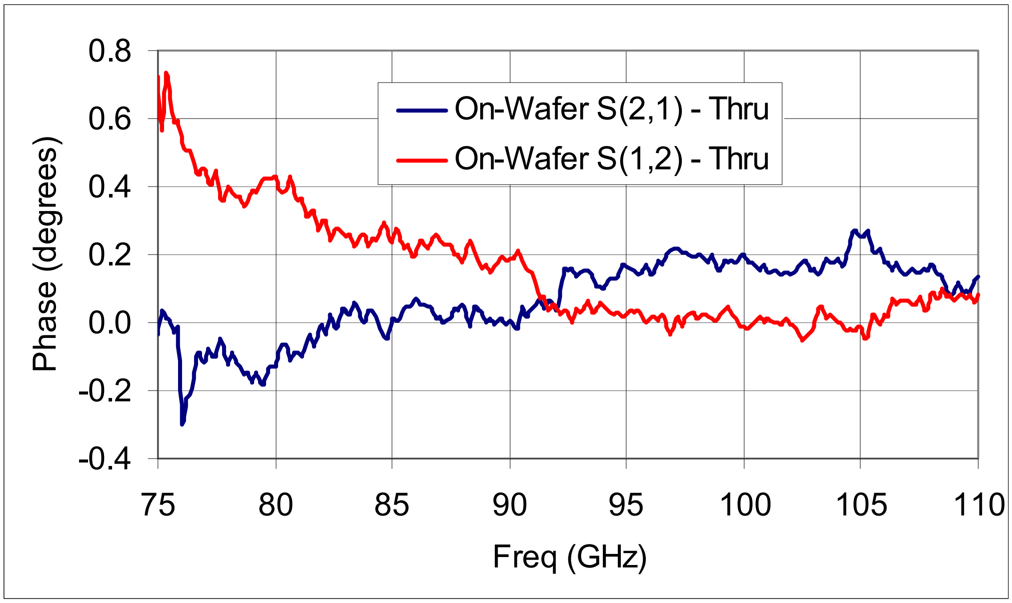

Figure C.11: Phase of the On-wafer Thru Standard.

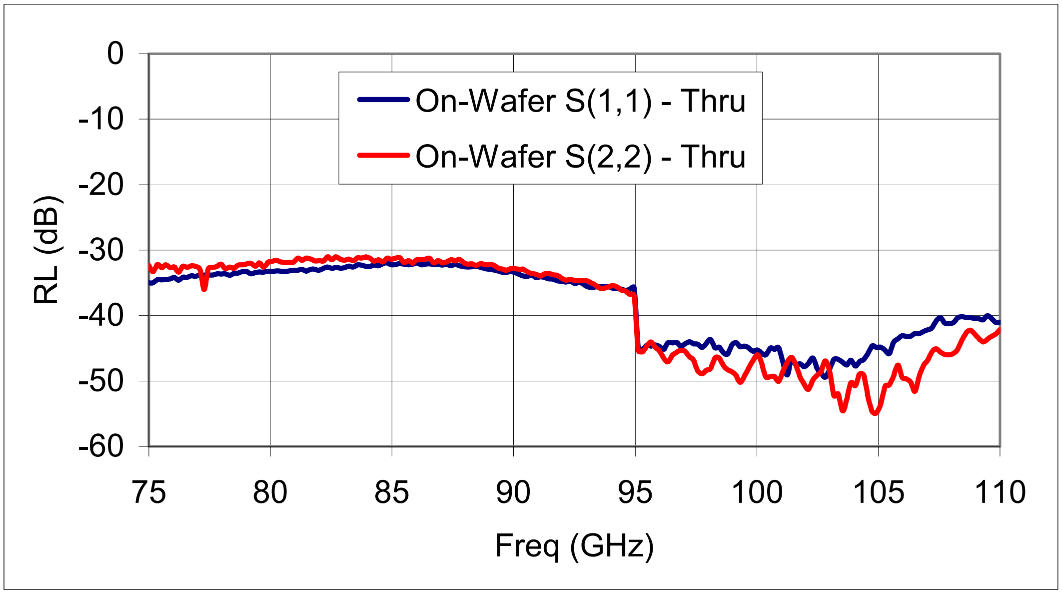

Figure C.12: RL of the On-wafer Thru Standard.

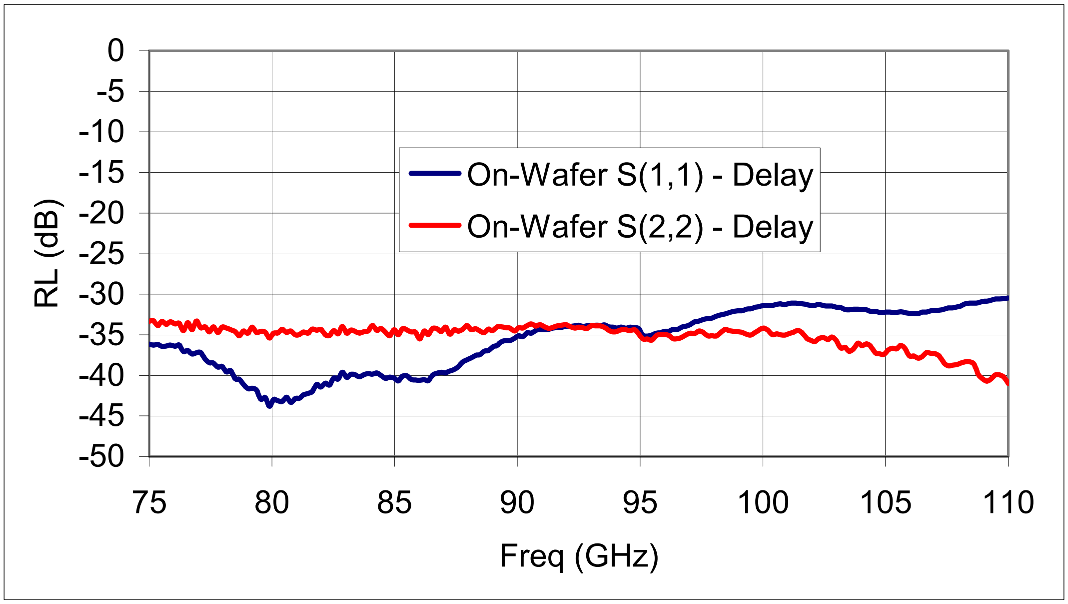

Figure C.13: RL of the On-wafer Delay Standard.

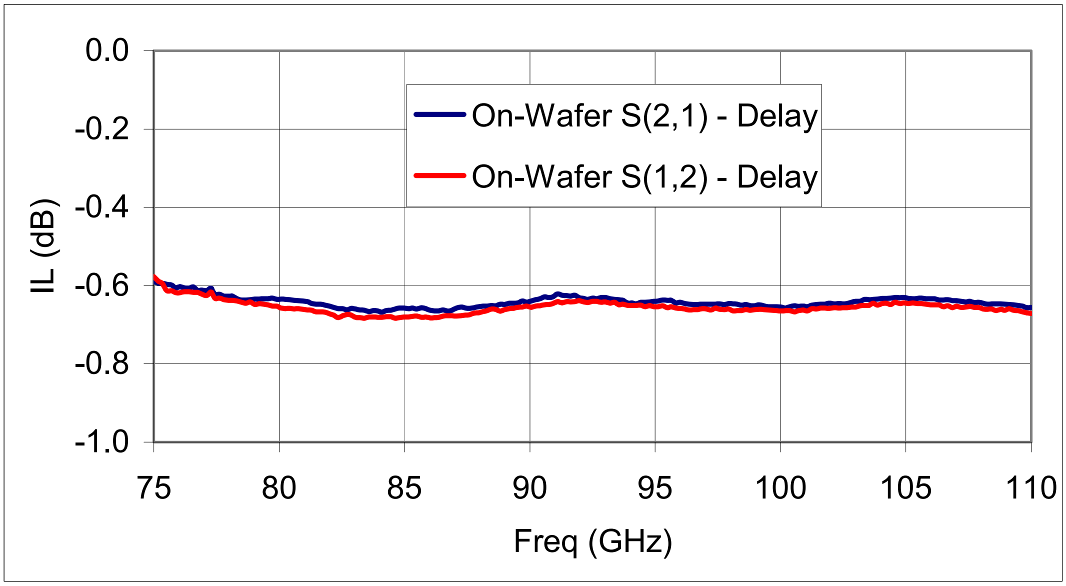

Figure C.14: IL of the On-wafer Delay Standard.

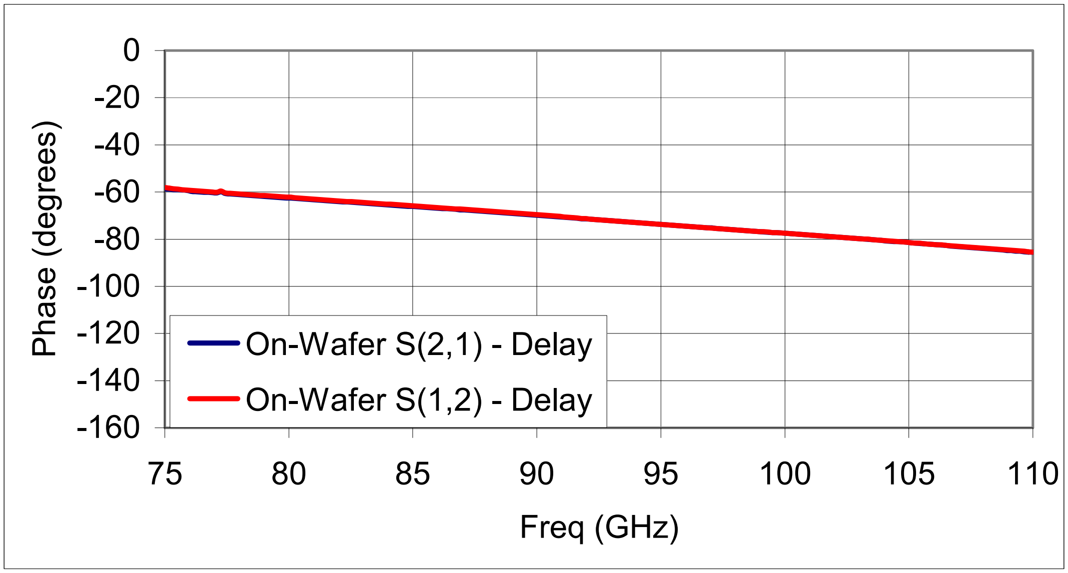

Figure C.15: Phase of the On-wafer Delay Standard.

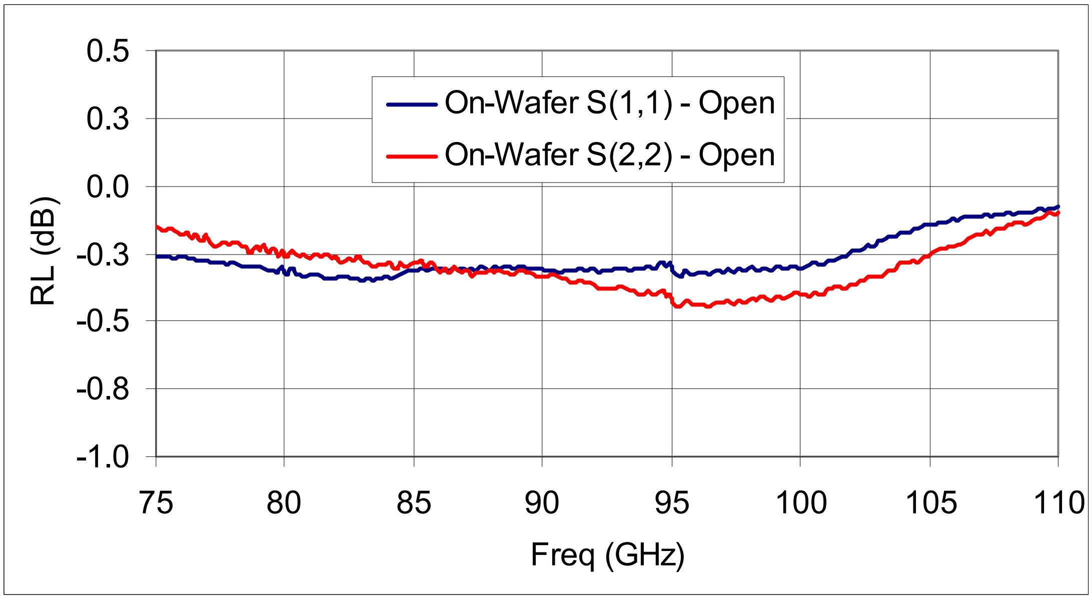

Figure C.16: RL of the On-wafer Open Standard.

Appendix C (Continued)

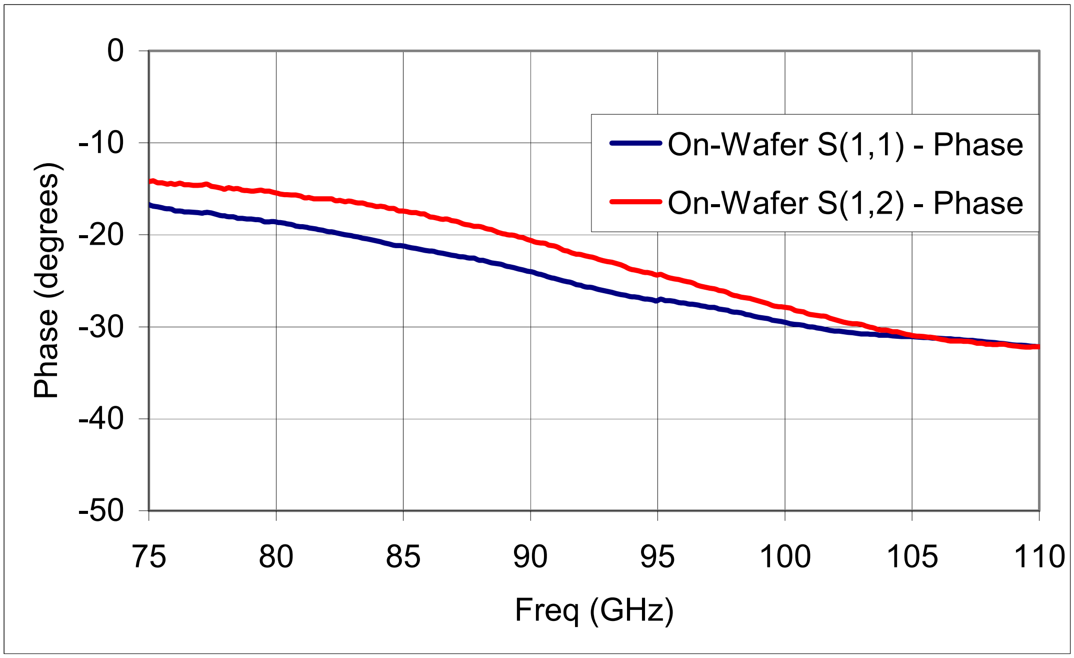

Figure C.17: Phase of the On-wafer Open Standard.